No. 316
February 1991

LARGE-AMPLITUDE SHIP MOTIONS IN THE TIME DOMAIN

Allan R. Magee

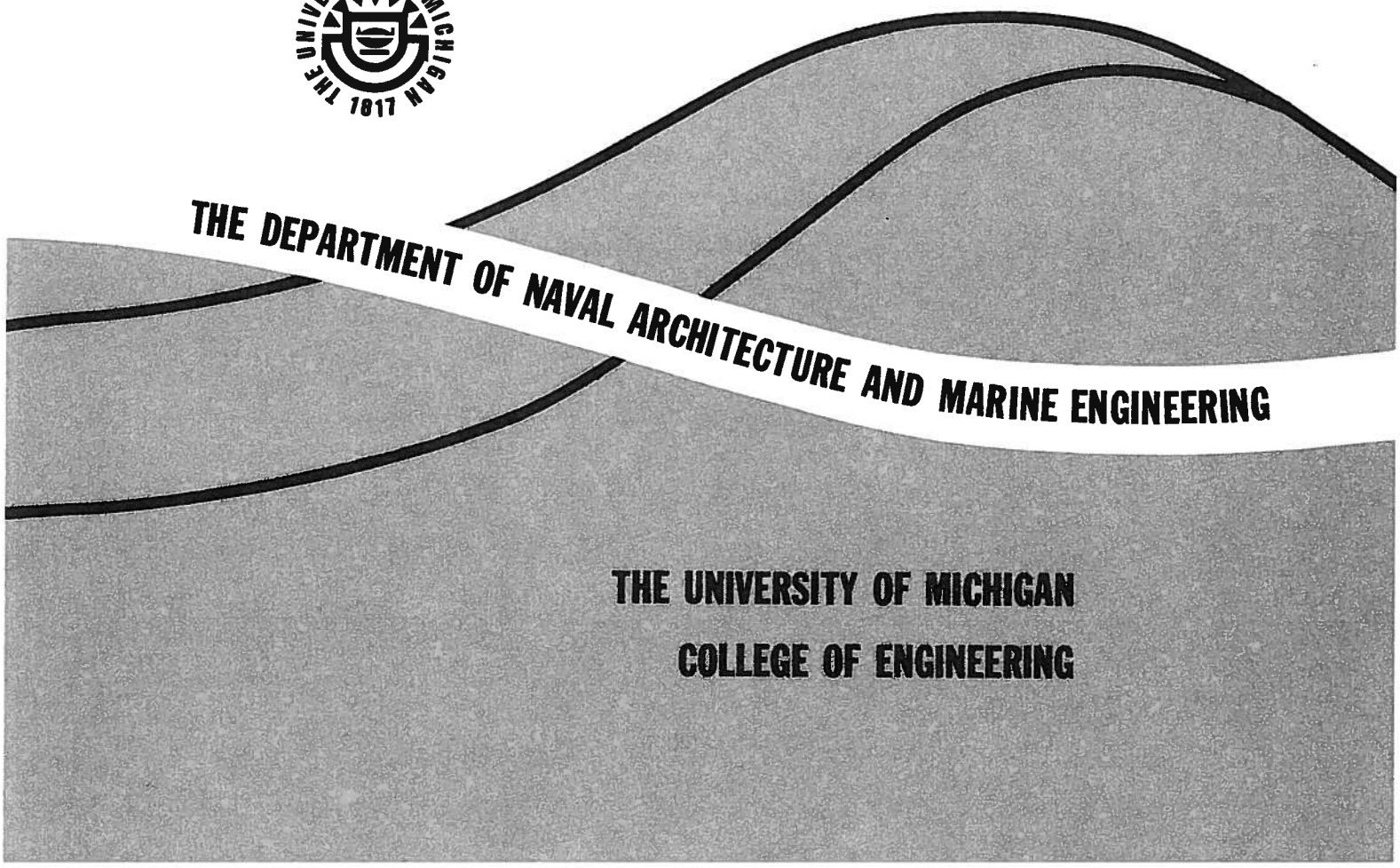

LARGE-AMPLITUDE SHIP MOTIONS IN THE TIME DOMAIN

by

Allan R. Magee

A dissertation submitted in partial fulfillment
of the requirements for the degree of
Doctor of Philosophy
(Naval Architecture and Marine Engineering)
in The University of Michigan
1991

Doctoral Committee:

Professor Robert F. Beck, Chairperson
Associate Professor Klaus-Peter Beier
Assistant Professor William W. Schultz
Associate Professor Armin Troesch

ABSTRACT

LARGE-AMPLITUDE SHIP MOTIONS IN THE TIME DOMAIN

by

Allan R. Magee

Chair: Robert F. Beck

The use of time-domain analysis for predicting ship motions is investigated. In the method, the hydrodynamic problem is solved directly in the time domain as an initial value problem starting from rest rather than using the more conventional frequency-domain formulation.

Both linear and large-amplitude motions are considered. The large-amplitude problem requires the body boundary condition to be satisfied on the instantaneous position of the body while maintaining the linearized free surface boundary condition. In the linear problem, the body boundary condition is also linearized about the mean position of the body. Because the free surface condition remains linear, a time-domain Green function approach can be used to solve both problems.

Results of linear time-domain calculations are presented and compared with experiments. Large-amplitude computations are also performed for submerged bodies. In both cases, the influence on the time-domain results of the singularity in the frequency domain at $\tau = 1/4$ is discussed.

ACKNOWLEDGEMENTS

I would like to thank Professor Beck for all of his efforts. This work would never have been possible without his dedication, his enthusiasm, and his experience, as well as the financial support. In addition, Professor Beier provided me with my first graduate student support, and taught me how to draw a graph on a computer, a skill which has proven quite useful. The M-Plot graphics in this thesis are the result of his hard work.

Thanks are also due to Jeff Falzarano, Rich Korpus, Nikiforos Papadakis, and Lisa Payton. Friends like these don't come along every day (Thank God!), and I never would have made it without you. Special thanks go to Rosa Borge, who put up with my moods remarkably well during some of the most trying times.

This research was funded by The Office of Naval Research, Contract No. N00014-88-K-0628. Computations were made in part using a CRAY Grant, University Research and Development Program, at the San Diego Supercomputer Center.

TABLE OF CONTENTS

LIST OF FIGURES

CHAPTER I

INTRODUCTION

The development of three-dimensional solutions to the ship motion problem has evolved on two fronts: the time-domain, or transient method, and the frequency-domain method. For strictly linear problems, that is, when both the free surface boundary condition and the body boundary condition are linearized, the time and frequency-domain solutions are related by a Fourier transform, and are complementary. For time-dependent geometries executing large-amplitude motions, or for fully nonlinear problems, the time-domain approach is the most useful— frequency-domain solutions being limited to a few special cases.

The Neumann-Kelvin approximations, in which the free surface boundary condition is linearized about the free stream by assuming a small disturbance potential, but the body boundary condition is applied on the three-dimensional body surface, are considered by some to be mathematically inconsistent for surface-piercing bodies. Such an inconsistency is not present for a submerged body which will always produce small waves, if submerged deeply enough. The so-called Dawson techniques which linearize the free surface about the double body flow are an alternative. (See Scragg (1990).) Various formulations are possible, depending on the order of magnitude assumptions about the various terms in the free surface condition.

Despite the apparent inconsistency, the Neumann-Kelvin approximations have

often been successfully applied to floating bodies, in both steady and unsteady linear problems in the time and frequency domains. The results have generally been encouraging for bodies which are vertical, or nearly so at the waterline. However, less convincing evidence exists that solutions for bodies which have a large flare at the waterline are so easily attainable.

Although the idea of time-domain analysis is not particularly new, it is certainly the most logical and straightforward way to pursue solutions of increasingly more accurate models. The fundamental solution for the time-domain Green function, a source moving arbitrarily beneath a linearized free surface, has generally been attributed to Finkelstein (1957), but must now also be credited to Brard (1948). (See Ferrant (1990).) Discussions of direct time-domain solutions were presented by Stoker (1957), Cummins (1962), Ogilvie (1964), and Wehausen (1967). Actual solutions of the time-domain problem were performed by Adachi and Omatsu (1979) and by Yeung (1982) for two-dimensional bodies, by Jami and Pot (1985), for the transient motion of a sphere, and by Newman (1985), for the axisymmetric vertical cylinder, but it was not until Liapis and Beck (1985), and Liapis (1986) that the method was applied to ships. Subsequently, King (1987) and King et al. (1988) developed a method of solving for both radiation and exciting forces using a non-impulsive method, at both zero and steady forward speed and Korsmeyer (1988) examined the transient solution up to second order at zero forward speed.

Closer to the point of this work, however, is the formulation of Ferrant (1989). A solution was presented for submerged bodies in large-amplitude forced heave motion in the time domain. A linearized free surface was used while the body boundary condition was applied on the time-dependent three-dimensional body surface. A large-amplitude formulation in the frequency domain for a heaving body was also given. Beck and Magee (1990) presented a large-amplitude formulation which included the line integral terms for surface-piercing bodies and numerical results for submerged

bodies. This work included unsteady forward speed as one case of the forced large-amplitude motion problem. Lin and Yue (1990) used a similar formulation and solved the equations of motion in the time domain to produce large-amplitude motion simulations for surface-piercing bodies. The line integrals and forward speed calculations for submerged bodies were also included in Ferrant (1990).

This so-called body-exact or exact Neumann-Kelvin formulation, which is the focus of this work, can be viewed as an extension of the strictly linear time-dependent solutions mentioned above, or as the time-dependent equivalent of the classic Neumann-Kelvin solution for steady forward speed. Both these solutions are contained as special cases of the body-exact problem as limits of the amplitude of the unsteady motions, and frequency of the surge motion, respectively, go to zero.

The analogous frequency-domain approach was begun much earlier with the two-dimensional strip theories, (cf. Salvesen, et al. , (1970)) the rational formulation of which was given by Ogilvie and Tuck (1969). The unified theory, was developed by Newman (1978) and calculations were carried through by Sclavounos (1985). Yeung and Kim (1985) also presented a more consistent slender ship formulation. Recently, Faltinsen and Zhao (1990) and Ohkusu and Faltinsen (1990) presented a new strip theory using different slenderness assumptions for bodies with high forward speed. The success of these methods lies in the low computational requirements (no supercomputer is necessary) and, considering their approximate nature, the remarkable accuracy of the results obtainable, especially at high frequencies. However, deficiencies are apparent in the strip theory results, and some of these will be discussed.

Korsmeyer et al. (1988) have demonstrated the convergence of zero speed frequency-domain methods using up to 12,600 panels on a TLP. Despite the difficulties of computing the required Green function, Chang (1977), Inglis and Price (1981b), Guevel and Bougis (1982) and several others have obtained three-dimensional frequency-domain solutions for ships with forward speed. Recent efforts in the frequency-

domain include Nakos (1990), and Sclavounos and Nakos (1990) who used bi-quadratic splines and Rankine sources (obviating the need for the complicated Green function) to solve the linearized problem with forward speed. Ohkusu and Iwashita (1989) have found an analytic form for the integral of the frequency-domain Green function over lines and panels. This could prove promising for studies of surface-piercing bodies with forward speed. Hoff (1990) brings to light the difficulties associated with calculations using the forward speed three-dimensional frequency-domain Green function.

Fully nonlinear three-dimensional solutions, which account for both the nonlinearities in the free surface boundary condition and also solve the true body boundary condition are being pursued. They have met with some success (cf. Jensen, Mi and Söding (1988), Cao, Schultz and Beck (1990), and Bertram (1990)). One of the shortcomings shared by the time-dependent nonlinear solutions is the computational power required to discretize a large portion of the free surface with a grid fine enough to resolve all frequencies of interest. This in fact leads to another possible application of the time-domain method— that of providing far field conditions with which to match a fully nonlinear inner-domain solution. A combined method may be developed in order to reduce the extent of the free surface that must be paneled, and to minimize reflections at the computational boundaries. Such a method was employed by Dommermuth and Yue (1988) who used a linear time-domain solution in the far field to match a fully nonlinear inner-domain solution for axisymmetric flows.

In general, complicated body shapes are more difficult to treat than smooth, analytically defined bodies. Some of the difficulty is related to the approximation of arbitrary shpaes with a relatively small number of flat panels. Recently, several methods have become available to panelize arbitrary geometries. The program PANNURBS, Harries, (1990) allows the user interactive control over the distribution of panels which are formed as the intersection of parameter lines on a normalized rational B-spline surface. Individual panels can be deformed and modified by drag-

ging parameter lines around the u-v space. The program includes an algorithm for intersecting the body surface with an arbitrary plane, such as the linearized free surface.

Another solution is the Air Force public domain program *I3G*, Burtness and Steele, 1989, which employs splines to develop a grid, and automatic smoothing techniques to refine and modify this grid. Arbitrary geometries are easily handled. This program has extensive capabilities, but it still requires input from the user.

The black art of paneling is still subjective, and involves choices based on the user's experience. Liapis (1988) has given a method for determining optimal paneling, and perhaps this can guide us in determining good overall discretization parameters. Of course, the method of choice must be efficient enough to provide adequate solutions without unreasonably increasing the cost of the computations.

1.1 Overview

The present method is an extension of Beck, Liapis and King's work on the linear problems. The extension allows large-amplitude motions of a body of arbitrary geometry to be studied using a panel method. The body boundary condition is applied on the three-dimensional, time-dependent body surface, as opposed to the usual (linear) methods which have traditionally assumed small motions, allowing the mean, steady three-dimensional body position to be used. As usual, the fluid is assumed ideal and incompressible. The linearized free surface is retained, and hence the time-domain Green function can be used. The Green function satisfies the free surface and radiation conditions, so that unknowns need only be distributed on the body surface. The resulting system for the large-amplitude problem is not in fact nonlinear. Rather, it is a time-dependent linear system which at times exhibits behavior that appears to be nonlinear. As the amplitude of motion goes to zero, the

linear solutions for unsteady motions about a fixed or steadily moving mean position can be recovered.

However, many of the advantages of a linear system are lost in the body-exact formulation. For instance, the impulse-response function which can be derived assuming small-amplitude motions is no longer valid. The superposition theorem is not valid for large-amplitude motions— doubling the amplitude does not double the force. The computational burden is greatly increased because the time-dependent geometry requires that the Green function be recomputed at every time step for the entire relevant past history of the motion. This changes the order of computations from $O(K_T)$ for the fully linear problem to $O(K_T^2)$ for the large-motion problem, where K_T is the number of time steps. Despite the difficulties, much interesting information can be gained by the study of such a formulation. Many of the important features of fully nonlinear solutions can be understood with its use.

The thesis is divided into six chapters. After this introduction, Chapter 2 gives the formulation for the body-exact problem to be solved using potential and source distributions in the time-domain. The linear problem using the mean body position is also formulated for completeness, as it will be referred to later. Chapter 3 gives a description of the numerical methods, and includes a discussion of the methods used to vectorize the Green function calculations. Chapter 4 presents results for the body-exact problem for submerged bodies. The problems progress from simpler examples up to some cases of arbitrary specified motion. The results are compared with existing analytical and numerical solutions.

Before attacking the body-exact problem for surface-piercing bodies, research was again devoted to the linear problem. Some results of calculations for a modified Wigley hull, and some of the difficulties (for bodies with large flare at the waterline) are presented in Chapter 5. Comparisons are made with strip theory and experimental results. Chapter 6 gives conclusions and suggestions for further research.

CHAPTER II

THEORETICAL FORMULATION

2.1 The Body-Exact Problem

As presented in figure 1, the origin of the axis system is fixed on the free surface of an infinitely deep, incompressible, ideal fluid, initially at rest. The z-axis is positive upwards and the $z = 0$ plane corresponds to the calm water level. The direction of motion of the body is generally in the positive x-direction. The governing equation in the fluid for the velocity potential is the Laplace equation:

$$\nabla^2 \phi (x, y, z, t) = 0 \tag{2.1}$$

where the velocity of the fluid is given by

$$\mathbf{U} = \nabla \phi \tag{2.2}$$

The boundary condition on the free surface is linearized to yield:

$$\frac{\partial^2 \phi}{\partial t^2} - g \frac{\partial \phi}{\partial z} = 0 \qquad \text{on } z = 0 \tag{2.3}$$

For the so-called body-exact problem, the body boundary condition is satisfied on the instantaneous position of the body surface:

$$\frac{\partial \phi}{\partial n} = \mathbf{V} \cdot \mathbf{n} \qquad \text{on } S_B(t) \tag{2.4}$$

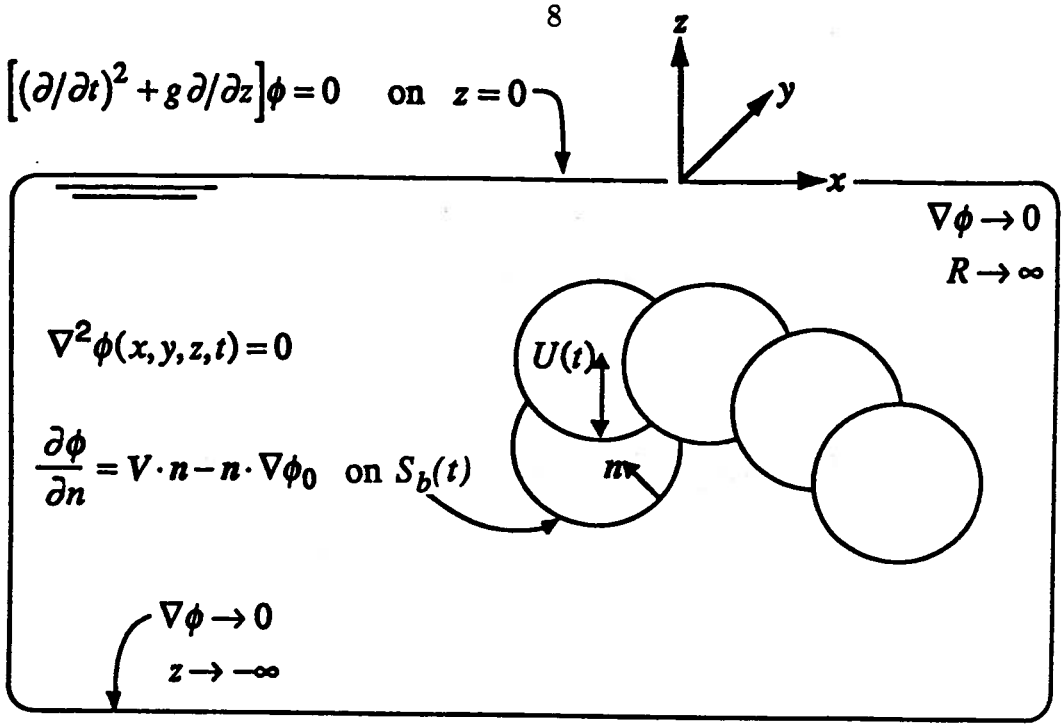

Figure 2.1: Coordinate system definition

where,

n = inward unit normal to the body surface, out of the fluid.

V = instantaneous velocity of a point on the body surface including angular velocity effects.

At infinity, the fluid velocities must all go to zero such that:

$$\nabla\phi \to 0 \qquad \text{as } z \to -\infty \tag{2.5}$$

$$\nabla\phi \to 0 \qquad \text{as } R \to \infty \tag{2.6}$$

where R is the horizontal distance from the body. The motion starts from rest so that the initial conditions are:

$$\phi,\ \frac{\partial\phi}{\partial t} \to 0 \qquad \text{as } t \to -\infty \tag{2.7}$$

In the usual manner, an integral equation that must be solved to determine ϕ is found by applying Green's theorem to the fluid domain yielding:

$$\iiint_V dV\ \left(\phi\,\nabla^2 G - G\,\nabla^2\phi\right) = \iint_S dS\ \left(\phi\,\frac{\partial G}{\partial n} - G\,\frac{\partial\phi}{\partial n}\right) \tag{2.8}$$

with the volume V bounded by S, where $S = S_B \cup S_F \cup S_\infty$, and S_B is the body surface, S_F is the free surface, and S_∞ is the bounding surface at infinity.

The Green function for the time dependent problem is given by

$$G(P,Q,t,\tau) = \left(\frac{1}{r} - \frac{1}{r'}\right)\delta(t-\tau) + \tilde{G}(P,Q,t,\tau)\,H(t-\tau) \tag{2.9}$$

where,

$$\begin{aligned}
\tilde{G}(P,Q,t,\tau) &= \int_0^\infty dk\sqrt{kg}\sin\left(\sqrt{kg}\,(t-\tau)\right)e^{k(z+\zeta)}J_0(kR) \\
P &= (x(t), y(t), z(t)) \\
Q &= (\xi(\tau), \eta(\tau), \zeta(\tau)) \\
r &= \left((x-\xi)^2 + (y-\eta)^2 + (z-\zeta)^2\right)^{\frac{1}{2}} \\
r' &= \left((x-\xi)^2 + (y-\eta)^2 + (z+\zeta)^2\right)^{\frac{1}{2}} \\
R &= \left((x-\xi)^2 + (y-\eta)^2\right)^{\frac{1}{2}} \\
\delta(t) &= \text{delta function} \\
&= \int_{-\infty}^{\infty} \delta(t)\,f(t)\,dt = f(0)
\end{aligned}$$

$H(t) =$ unit step function

$$= \begin{cases} 0 & \text{if } t < 0 \\ 1 & \text{if } t > 0 \end{cases}$$

It can be shown that the Green function has the following properties:

$$\begin{aligned}
\nabla^2 G &= -4\pi\delta(P-Q)\,\delta(t-\tau) \\
\frac{\partial^2 G}{\partial^2 t} + g\frac{\partial G}{\partial z} &= 0 \qquad \text{on } z = 0 \\
G,\ \frac{\partial G}{\partial t} &= 0 \qquad t - \tau < 0 \\
\nabla G &\to 0 \qquad \text{as } r \to \infty
\end{aligned}$$

Substituting the Green function into (2.8), integrating both sides with respect to τ and then reducing the integrals over the free surface using a two-dimensional

transport theorem (See Appendix A for details.) results in the following integral equation for $\phi(P,t)$:

$$\phi(P,t)+\frac{1}{2\pi}\int\int_{S_B(t)}dS_Q\;\phi(Q,t)\frac{\partial}{\partial n_Q}\left(\frac{1}{r}-\frac{1}{r'}\right)=\frac{1}{2\pi}\int\int_{S_B(t)}dS_Q\left(\frac{1}{r}-\frac{1}{r'}\right)\frac{\partial}{\partial n_Q}\phi(Q,t)$$
$$-\frac{1}{2\pi}\int_{-\infty}^{t}d\tau\int\int_{S_B(\tau)}dS_Q\left\{\phi(Q,\tau)\frac{\partial}{\partial n_Q}\tilde{G}(P,Q,t,\tau)-\tilde{G}(P,Q,t,\tau)\frac{\partial}{\partial n_Q}\phi(Q,\tau)\right\} \tag{2.10}$$
$$-\frac{1}{2\pi g}\int_{-\infty}^{t}d\tau\oint_{\Gamma(\tau)}dl_Q\left\{\phi(Q,\tau)\frac{\partial}{\partial\tau}\tilde{G}(P,Q,t,\tau)-\tilde{G}(P,Q,t,\tau)\frac{\partial}{\partial\tau}\phi(Q,\tau)\right\}V_N(Q,\tau)$$

where $\Gamma(t)$ is the curve defined by the instantaneous intersection of the mean hull position and the $z=0$ plane and V_N is the two-dimensional normal velocity in the $z=0$ plane of a point on Γ.

It should be noted that in the linearized problem the line integrals are zero at zero forward speed. However, for the body-exact problem the line integrals have nonzero values even at zero forward speed unless the body is wall sided for all points on Γ for all time. If the shape or location of the waterplane changes, the line integral terms must be included. These terms reduce to those given by King et al. (1988) for constant forward speed. For a body which is executing an unsteady, large amplitude maneuver in the horizontal plane, they reduce to the equation given by Liapis (1986) in his Appendix A.

In many situations a source formulation is more convenient because it is easier to compute the tangential velocities on the body surface. In the usual manner of potential theory (cf. Lamb (1929)), it is possible to derive the following integral equation for the source strength on the body surface. The details are given in Appendix B.

$$-\frac{\sigma(P,t)}{2}-\frac{1}{4\pi}\int\int_{S_B(t)}dS_Q\;\sigma(Q,t)\frac{\partial}{\partial n_P}\left(\frac{1}{r}-\frac{1}{r'}\right)=\frac{\partial\phi(P,t)}{\partial n_P}$$
$$+\frac{1}{4\pi}\int_{-\infty}^{t}d\tau\int\int_{S_B(\tau)}dS_Q\;\sigma(Q,\tau)\frac{\partial}{\partial n_P}\tilde{G}(P,Q,t,\tau) \tag{2.11}$$
$$+\frac{1}{4\pi g}\int_{-\infty}^{t}d\tau\oint_{\Gamma(\tau)}dl_Q\;\sigma(Q,\tau)V_n(Q,\tau)V_N(Q,\tau)\frac{\partial}{\partial n_P}\tilde{G}(P,Q,t,\tau)$$

Here, V_n is the three-dimensional normal velocity of a point on $\Gamma(t)$ and $\sigma(P,t)$ is the unknown source strength. The potential on the body surface is given by

$$\phi(P,t) = -\frac{1}{4\pi}\iint_{S_B(t)} dS_Q\, \sigma(Q,t)\left(\frac{1}{r}-\frac{1}{r'}\right) - \frac{1}{4\pi}\int_{-\infty}^{t} d\tau \iint_{S_B(\tau)} dS_Q\, \sigma(Q,\tau)\,\tilde{G}(P,Q,t,\tau)$$

$$+\frac{1}{4\pi g}\int_{-\infty}^{t} d\tau \oint_{\Gamma(\tau)} dl_Q \left\{\sigma(Q,\tau)\,\tilde{G}(P,Q,t,\tau)\right\} V_n(Q,\tau)\, V_N(Q,\tau) \qquad (2.12)$$

The velocity of the fluid is found by taking the gradient of (2.12) with respect to the field point variable.

The hydrodynamic forces acting on the body due to a prescribed body motion are found by integrating the pressure over the body surface. The unsteady pressure is given by Bernoulli's equation:

$$\frac{p}{\rho} = -\left(\frac{\partial\phi}{\partial t} + \mathbf{V}\cdot\nabla\phi\right) - \frac{1}{2}|\nabla\phi|^2 + \mathbf{V}\cdot\nabla\phi - gz \qquad (2.13)$$

The term $\mathbf{V}\cdot\nabla\phi$ has been added and subtracted. This form is more convenient because the term in parenthesis represents the time derivative following a point on the body. Other representations are possible, and may prove to be more useful for the surface-piercing body. The generalized force on the body in the jth direction is then given by:

$$F_j = \iint_{S_B(t)} dS_Q\; p(Q,t)\;\; n_j(Q,t) \qquad j = 1,2,\ldots,\ 6 \qquad (2.14)$$

where n_j, representing the generalized unit normal, is defined as

$$\begin{aligned} (n_1,n_2,n_3) &= \mathbf{n} \\ (n_4,n_5,n_6) &= \mathbf{r}\times\mathbf{n} \\ \overline{\mathbf{r}} &= (\overline{x},\overline{y},\overline{z}) \end{aligned} \qquad (2.15)$$

where $(\overline{x},\overline{y},\overline{z})$ are coordinates in the body axis system and $j = 1,2,3$ correspond to the directions of the $(\overline{x},\overline{y},\overline{z},)$ axes, respectively.

2.2 Simulations Using the Body-Exact Formulation

The body-exact formulation is primarily useful for simulations in which the equations of motion are solved by direct integration. The input to the system would then be the incident wave field. A suitable superposition of sine waves could be used for this purpose. While such a simulation is not included in this thesis, it has been one of the goals towards which this work is directed. The computer code has been written with an eye toward this problem.

To include the incident wave field in the problem, the boundary condition (2.4) is modified by the addition of an extra term. Thus,

$$\frac{\partial \phi}{\partial n} = \mathbf{V} \cdot \mathbf{n} - \frac{\partial \phi_0}{\partial n} \qquad \text{on } S_B(t) \tag{2.16}$$

where, ϕ_0 is the potential due to the incident wave field. King (1987) has shown how to obtain the potential at any point in time and space from a time history of the wave elevation at any point for long-crested linear waves. If the incident wave elevation is given at the origin as $\zeta_0(t)$, then at any point in the fixed coordinate system the incident wave velocity is given by:

$$\nabla \phi_0(P,t) = \int_{-\infty}^{\infty} d\tau \, \underline{K}(P, t-\tau) \, \zeta_0(\tau) \tag{2.17}$$

where,

$$\underline{K}(P,t) = \frac{1}{\pi} \left\{ \left[\hat{i} \cos(\beta), \, \hat{j} \sin(\beta), \, \hat{k} \right]^T \int_0^t d\omega \, \omega e^{k(z-i\varpi)} e^{i\omega t} \right\}$$

$$\varpi = x \cos\beta + y \sin\beta$$

$$\beta = \text{direction of the incident waves relative to the x-axis}$$

The latter integral can be evaluated in closed form as shown in Appendix B of King (1987).

The solution of this boundary value problem would yield the pressure and the total forces on the body. The equations of motion in the body-fixed system (cf.

Falzarano (1990) or Guo (1981)) could then be integrated in time. A suitable differential equation integrator, such as a fourth-order Runge-Kutta could be used to time step the equations. The intermediate steps would require extra evaluations of the Green function matrix at each time step. An alternative method for solving the equations of motion is given by Kang (1990). Additional linear or nonlinear external forces such as a mooring line force or water-on-deck forces could be included.

2.3 The Linear Problem

The above body-exact formulation is for the problem in which the body boundary condition is satisfied on the instantaneous position of the body surface. Because the resulting system is nonstationary in time, much of the linear system theory normally invoked in seakeeping analysis cannot be used. As stated, the body-exact approach is most useful for large-amplitude simulations.

If in addition to the use of a linear free surface boundary condition, the assumption is made that the amplitude of motion is small, a linearized time-domain analysis may be developed for the constant or zero forward speed case. The linear body boundary condition can be applied on the mean, three-dimensional body position. The correct body boundary condition was given by Timman and Newman (1962), and discussed in detail in Newman (1978). The superposition theorem holds for this system, since it holds for Laplace's equation and all the boundary conditions.

The development which follows is given in more detail in King (1987), but is repeated here for completeness. Either impulsive or nonimpulsive inputs can be used. The resulting transient response can be Fourier transformed to compare with frequency-domain representations. Liapis and Beck (1985) developed a theory for the impulsive radiation problem. King et al. (1988) developed a nonimpulsive approach to both the radiation and exciting-force problems. If impulsive methods are used, certain variables may not decay quickly enough for Fourier transforms to be easily

taken. Limiting the frequency range by appropriate choice of the nonimpulsive input can reduce numerical errors in the computations. See King's discussion for the proper choice of input.

In linear time-domain analysis it is more convenient to work in a coordinate system fixed to the moving vessel. The total velocity potential is then defined as:

$$\Phi_T(x,y,z,t) = -U_0 x + \Phi_0(x,y,z) + \phi_0(x,y,z,t) + \Phi(x,y,z,t) \tag{2.18}$$

where,

$$\begin{aligned}
-U_0 x + \Phi_0 &= \text{the potential due to steady translation} \\
U_0 &= \text{the steady forward speed of the ship} \\
\phi_0 &= \text{the incident wave potential} \\
\Phi(x,y,z,t) &= \sum_{k=1}^{7} \phi(x,y,z,t) \\
\phi_7 &= \text{the diffracted wave} \\
\phi_{1,\ldots,6} &= \text{the potentials due to the body motions} \\
&\quad \text{surge, sway, heave, roll, pitch and yaw, respectively.}
\end{aligned} \tag{2.19}$$

To meet the appropriate body boundary condition, $\partial\Phi_T/\partial n = 0$ on the mean body surface S_0, the following boundary conditions are specified for the various potentials:

$$\begin{aligned}
\frac{\partial \Phi_0}{\partial n} &= U_0 n_1 \qquad \text{on } S_0 \\
\frac{\partial \phi_7}{\partial n} &= -\frac{\partial \phi_0}{\partial n} \qquad \text{on } S_0 \\
\frac{\partial \phi_k}{\partial n} &= n_k \dot{\zeta}_k + m_k \zeta_k \qquad \text{on } S_0
\end{aligned} \tag{2.20}$$

where ζ_k is the displacement in the kth mode of motion, and the overdot represents the derivative with respect to time, n_k is the generalized unit normal given in (2.15) and m_k, resulting from the steady forward motion, is given by

$$
\begin{aligned}
(m_1, m_2, m_3) &= -(\mathbf{n} \cdot \nabla)\, \mathbf{W} \\
(m_4, m_5, m_6) &= -(\mathbf{n} \cdot \nabla)\, (\mathbf{r} \times \mathbf{W}) \\
\mathbf{W} &= \nabla\, (-U_0 x + \Phi_0)
\end{aligned}
\tag{2.21}
$$

$\mathbf{W}$ is the fluid velocity due to the steady forward motion of the vessel in the ship fixed coordinate frame. It represents the solution of the steady Neumann-Kelvin problem, and the m-terms in the boundary condition (2.18) are the first order interaction terms between the steady and unsteady components of the flow. In King (1987) this term was approximated as

$$
\mathbf{W} = -U_0 \hat{\imath} \tag{2.22}
$$

In this case, the m-terms reduce to the simple form

$$
(m_1, m_2, \ldots\ m_6) = (0, 0, 0, 0, U_0 n_3, -U_0 n_2) \tag{2.23}
$$

The solution of the steady Neumann-Kelvin problem is included in the solution of the body-exact problem by specifying a constant forward speed in the boundary condition (2.4) and no unsteady motion.

The linearized free surface condition in the moving coordinate system is written as:

$$
\left(\frac{\partial}{\partial t} - U_0 \frac{\partial}{\partial x} \right) \phi_k + g \frac{\partial}{\partial z} \phi_k = 0 \qquad \text{on } z = 0 \tag{2.24}
$$

The initial conditions for the unsteady potentials are:

$$
\phi_k\ ,\ \frac{\partial \phi_k}{\partial t} \to 0 \qquad \text{as } t \to -\infty \tag{2.25}
$$

Because the potentials for both radiation and diffraction problems originate in the neighborhood of the origin

$$
\nabla \phi_k\, (x, y, z, t) \to 0 \qquad \text{on } S_\infty \qquad k = 1, 2, \ldots, 7 \tag{2.26}
$$

It can be shown that the Green function given by (2.8) also satisfies these conditions if the appropriate transformation is made to the moving coordinate system, King (1987).

In developing the linear boundary value problem implied by (2.18)– (2.26), there is an implicit assumption that the body geometry is such that the steady disturbance potential Φ_0 is small. This must be so in order to justify the linearization of the free surface boundary condition about the free stream velocity U_0. In addition, the amplitude of motion must be small because the body boundary condition has been expanded about the mean position of the body surface.

As with the body-exact problem, an integral equation to determine the unknown linear potentials is found by applying Green's theorem and using the Green function (2.9). The final result may be found in King et al. (1988) and is

$$\begin{aligned}
&\phi(P,t)+\frac{1}{2\pi}\int\!\!\int_{S_0} dS_Q \phi(Q,t)\frac{\partial}{\partial n_Q}\left(\frac{1}{r}-\frac{1}{r'}\right)=\frac{1}{2\pi}\int\!\!\int_{S_0} dS_Q\left(\frac{1}{r}-\frac{1}{r'}\right)\frac{\partial}{\partial n_Q}\phi(Q,t)\\
&-\frac{1}{2\pi}\int_{-\infty}^{t} d\tau\int\!\!\int_{S_0} dS_Q\left\{\phi(Q,\tau)\frac{\partial}{\partial n_Q}\tilde{G}(P,Q,t-\tau)-\tilde{G}(P,Q,t-\tau)\frac{\partial}{\partial n_Q}\phi(Q,\tau)\right\}\\
&-\frac{1}{2\pi g}\int_{-\infty}^{t} d\tau\oint_{\Gamma_0} d\eta\left\{U_0^2\left(\phi(Q,\tau)\frac{\partial}{\partial \xi}\tilde{G}(P,Q,t-\tau)-\tilde{G}(P,Q,t-\tau)\frac{\partial}{\partial \xi}\phi(Q,\tau)\right)\right.\\
&\left.-U_0\left(\phi(Q,\tau)\frac{\partial}{\partial \tau}\tilde{G}(P,Q,t-\tau)-\tilde{G}(P,Q,t-\tau)\frac{\partial}{\partial \tau}\phi(Q,\tau)\right)\right\}
\end{aligned}\tag{2.27}$$

where Γ_0 is the curve defined by the intersection of the mean hull position and the $z=0$ plane. Details of the derivation can be found in Liapis (1986).

The linearized pressure is given by

$$\frac{p}{\rho}=-\left(\frac{\partial\phi}{\partial t}+\mathbf{W}\cdot\nabla\phi\right)\tag{2.28}$$

and the forces are found by integration over the body surface as:

$$F_j=-\rho\int\!\!\int_{S_0} dS_Q\left(\frac{\partial\phi}{\partial t}+\mathbf{W}\cdot\nabla\phi\right)n_j\qquad j=1,2,\ldots,6\tag{2.29}$$

To avoid taking gradients along the body surface, the theorem developed by Tuck is employed, Ogilvie (1977):

$$\int\int_{S_0} dS_Q \{m_j \phi(Q,t) + n_j (\mathbf{W} \cdot \nabla\phi)\} = -\oint_{\Gamma_0} dl_Q \, n_j (\mathbf{l} \times \mathbf{n}) \cdot \mathbf{W} \qquad (2.30)$$

where, l is the unit vector, tangent to the surface and lying in the $z = 0$ plane. This yields

$$F_j = -\rho \int\int_{S_0} dS_Q \frac{\partial \phi}{\partial t} n_j + \rho \int\int_{S_0} dS_Q \, \phi \, m_j + \rho \oint_{\Gamma_0} dl_Q \, \phi \, n_j (\mathbf{l} \times \mathbf{n}) \cdot \mathbf{W} \qquad (2.31)$$

The force in each mode j, due to motion in the mode k, can then be separated into two components.

$$F_{jk}(t) = -\frac{\partial}{\partial t} g_{jk}(t) - h_{jk}(t) \qquad (2.32)$$

where,

$$\begin{aligned} g_{jk} &= \rho \int\int_{S_0} dS_Q \, \phi_k \, n_j & j = 1,2,\ldots,6 \quad (2.33)\\ h_{jk} &= -\rho \int\int_{S_0} dS_Q \, \phi_k \, m_j - \rho \oint_{\Gamma_0} dl_Q \, \phi_k \, n_j (\mathbf{l} \times \mathbf{n}) \cdot \mathbf{W} & k = 1,2,\ldots,7 \end{aligned}$$

If the assumption is made that the flow is tangent to the hull at the waterline, i.e.,

$$\mathbf{W} = |\mathbf{W}| \mathbf{l} \qquad (2.34)$$

then,

$$(\mathbf{l} \times \mathbf{n}) \cdot \mathbf{W} = 0 \qquad (2.35)$$

The last term in (2.33) is then zero. This holds true exactly if the double body m-terms are used because the flow cannot penetrate the rigid free surface. If the approximate m-terms are used, then the term reduces to

$$(\mathbf{l} \times \mathbf{n}) \cdot \mathbf{W} = U_0 \, l_2 \, n_3 \qquad (2.36)$$

If the body is wall-sided, then n_3=0, and if it is slender, then l_2 is of higher order. In any case, it seems reasonable to neglect the contribution of this term, as was done in all the computations presented in Chapter 5.

2.4 Equivalence of Time and Frequency Domain Coefficients

For the linear problem, the hydrodynamic forces acting on the vessel can be related to the more traditional frequency-domain added mass and damping. The radiation force in mode j due to an imposed motion in mode k may be written in general as (cf. Cummins, 1962):

$$F_{jk}(t) = -\left(\mu_{jk}\ddot{\zeta}_k(t) + b_{jk}\dot{\zeta}_k(t) + c_{jk}\zeta_k(t) + \int_{-\infty}^{t} d\tau K_{jk}(t-\tau)\,\dot{\zeta}_k(\tau)\right) \tag{2.37}$$

where K_{jk} represents the memory effect due to the free surface and the hydrostatic restoring forces have been neglected.

It is shown in King (1987) that b_{jk} is zero and c_{jk} is a hydrodynamic force that is proportional to the body displacement. It is given by

$$c_{jk} = -\rho \int\int_{S_0} dS_Q\, \phi_{k\infty}\, m_j - \rho \oint_{\Gamma} dl_Q\, \phi_{k\infty}\, n_j\, (\mathbf{l}\times\mathbf{n})\cdot\mathbf{W} \tag{2.38}$$

where $\phi_{k\infty}$ represents the large-time limit of the potential ϕ_k. ϕ_k has a non-zero large-time limit because

$$\lim_{t\to\infty} \frac{\partial \phi_k}{\partial n} = m_k \tag{2.39}$$

which is nonzero. The integral equation that must be solved to determine $\phi_{k\infty}$ is given in King et al. (1988).

The factor μ_{jk} represents the infinite frequency added mass and is given by

$$\mu_{jk} = \rho \int\int_{S_0} dS\, \psi_k\, n_j \tag{2.40}$$

where, ψ_k is the solution to the integral equation

$$\psi_k + \frac{1}{2\pi}\int\int_{S_0} dS_Q\, \psi_k \frac{\partial}{\partial n_Q}\left(\frac{1}{r}-\frac{1}{r'}\right) = \frac{1}{2\pi}\int\int_{S_0} dS_Q\, n_k \left(\frac{1}{r}-\frac{1}{r'}\right) \tag{2.41}$$

For sinusoidal motions, the radiation forces are usually given in terms of the added mass and damping coefficients. The equivalence between the time-domain

force formulation and the frequency domain is found by substituting $\zeta_k(t) = e^{i\omega t}$ into (2.37) and equating it with the frequency-domain representation:

$$\begin{aligned} & \left[\omega^2 \mu_{jk} - c_{jk} - i\omega \int_{-\infty}^{\infty} d\tau \; K_{jk}(\tau)\, e^{-i\omega\tau}\right] e^{i\omega t} \\ = \; & \left[\omega^2 A_{jk}(\omega) - i\omega B_{jk}(\omega)\right] e^{i\omega t} \end{aligned} \tag{2.42}$$

Equating real and imaginary parts yields

$$\begin{aligned} A_{jk}(\omega) &= \mu_{jk} - \frac{1}{\omega}\int_0^{\infty} d\omega \; K_{jk}(t)\, sin(\omega t) - \frac{c_{jk}}{\omega^2} \\ B_{jk}(\omega) &= \int_0^{\infty} d\omega \; K_{jk}(t)\, cos(\omega t) \end{aligned} \tag{2.43}$$

The term c_{jk} is frequency independent. Since it multiplies the motion amplitude, it can be added to the hydrostatic restoring force coefficients in the usual frequency-domain equations of motion. In the typical strip theory, (Salvesen, Tuck, and Faltinsen, (1970)), this term does not appear. When comparing time-domain predictions with strip theory it therefore appears reasonable to retain c_{jk} with the added mass. In experiments, the hydrodynamic part of the spring constant term is sometimes subtracted off and at other times it is not. Thus, when comparing predictions with experiments one must take care to properly account for this term. One case of the influence of this term on the added mass will be shown in chapter 5.

CHAPTER III

NUMERICAL METHODS

3.1 Formulation of the Discrete Integral Equation

The principal numerical task in the time-domain method is the solution of the integral equation for either the unknown source strength (2.10) or the potential (2.11). Because the time-domain Green function satisfies the free surface and far-field conditions automatically, unknowns need only be distributed on the body surface. This greatly reduces the difficulty of the computations, but restricts the validity of the results to flows with small waves.

To solve the integral equations, a panel method is used in which the instantaneous wetted surface of the body is divided into quadrilateral panels. On each panel the unknown potential or source strength is assumed constant. A time marching scheme is used to solve the governing integral equation in the time domain. At each time step a new value of the unknown is determined on each panel. As opposed to the linear problem in which the components of the potential are separated into problems of radiation and diffraction with various possible symmetry combinations, in the body-exact problem we must deal with only one potential, whose symmetry is dictated by the body geometry and the incident wave field. In arbitrary six degrees of freedom

motion, there is no symmetry in the flow, so some computational advantages are lost. However, the problem is thus somewhat simplified, with lower required storage. The details of the numerical method for the linear problem may be found in King (1987) with modifications given below.

3.2 The Potential Formulation

At each time step N, the discrete form of the integral equation for the potential (2.10) due to large-amplitude motion can be written as

$$\sum_{q=1}^{M} A_{pq}^{N}\, \phi_{q}^{N} \;=\; B_{p}^{N} + C_{p}^{N} \tag{3.1}$$

where,

A_{pq}^{N} = the left hand side matrix

ϕ_{q}^{N} = the unknown potential vector

B_{p}^{N} = the right hand side vector due to the $1/r$ and $1/r'$ terms

C_{p}^{N} = the right hand side vector due to the wave terms

p = the field point

q = the source point

N = the time step number

M = the number of panels

The left hand side terms involve integrals over panels of derivatives of $1/r$ and $1/r'$. These are performed by the method of Hess and Smith (1964). The terms are:

$$\begin{aligned} A_{pq}^{N} &= 1 + \frac{1}{2\pi} \int\int_{S_q^N} dS \frac{\partial}{\partial n_q} \left(\frac{1}{r_{pq}} - \frac{1}{r'_{pq}} \right) \qquad p = q \\ &= \frac{1}{2\pi} \int\int_{S_q^N} dS \frac{\partial}{\partial n_q} \left(\frac{1}{r_{pq}} - \frac{1}{r'_{pq}} \right) \qquad p \neq q \end{aligned} \tag{3.2}$$

The right hand side contains integrals of $1/r$ and $1/r'$:

$$B_p^N = \frac{1}{2\pi}\sum_{q=1}^{M}\int\int_{S_q^N} dS\left(\frac{1}{r_{pq}}-\frac{1}{r'_{pq}}\right)\frac{\partial}{\partial n_q}\phi_q^N \tag{3.3}$$

For the floating body, both the $1/r$ and $1/r'$ terms must be recomputed at each time step because of the changing body position. For the submerged body, only the $1/r'$ terms must be recomputed since the body moves with respect to its image. For rotational body motions, the velocities induced by the $1/r$ terms must be rotated in the earth-fixed frame.

The additional terms are in the form of convolutions.

$$C_p^N = \frac{\Delta t}{2\pi}\sum_{k=2}^{N-1}\sum_{q=1}^{M}\int\int_{S_q^k} dS\left\{\tilde{G}_{pq}^{N-k}\frac{\partial}{\partial n_q}\phi_q^k-\phi_q^k\frac{\partial}{\partial n_q}\tilde{G}_{pq}^{N-k}\right\} \tag{3.4}$$

$$-\frac{\Delta t}{2\pi g}\sum_{k=2}^{N-1}\sum_{l=1}^{L}\int_{\Gamma_l^k} dl\left\{\phi_l^k\frac{\partial}{\partial \tau}\tilde{G}_{pl}^{N-k}-\tilde{G}_{pl}^{N-k}\frac{\partial}{\partial \tau}\phi_l^k\right\}V_{Nl}^k$$

where, V_N is the two-dimensional normal velocity in the $z=0$ plane of a point on Γ, and L is the number of line segments along the waterline. The temporal summation is the trapezoidal rule with endpoints neglected. The contributions from the endpoints are zero because $\tilde{G}(0)=0$ and $\phi(0)=0$.

The integrals of wave terms over panels are performed by mapping the quadrilaterals onto unit squares. Gauss quadrature is then used. For submerged bodies, a single point integration rule usually is sufficient. By placing the collocation point and the integration point at panel centroids, a monopole approximation can be used. Since the wave term is symmetric with respect to integration and field points, the number of Green function evaluations can thus be halved.

3.3 The Source Formulation

The form of the integral equation for the source formulation in the body-exact problem is similar to the one for the potential. In its discrete form the integral equation (2.11) is written as

$$\sum_{q=1}^{M} D_{pq}^{N}\,\sigma_{q}^{N} \;=\; E_{p}^{N} + F_{p}^{N} \tag{3.5}$$

where,

D_{pq}^{N} = the left hand side matrix

σ_{q}^{N} = the unknown source distribution

E_{p}^{N} = the right hand side vector due to the $\partial\phi/\partial n$ term

F_{p}^{N} = the right hand side vector due to the wave terms

and the indices are the same as those given in (3.1). Thus, we have

$$\begin{aligned}
D_{pq}^{N} &= -\frac{1}{2} - \frac{1}{4\pi}\int\!\!\int_{S_q^N} dS\left(\frac{1}{r_{pq}} - \frac{1}{r'_{pq}}\right) \qquad p = q \\
&= \qquad -\frac{1}{4\pi}\int\!\!\int_{S_q^N} dS\left(\frac{1}{r_{pq}} - \frac{1}{r'_{pq}}\right) \qquad p \neq q \\
E_{p}^{N} &= \frac{\partial}{\partial n_p}\phi_{p}^{N} \\
F_{p}^{N} &= \frac{\Delta t}{4\pi}\sum_{k=2}^{N-1}\left\{\sum_{q=1}^{M}\sigma_{q}^{k}\int\!\!\int_{S_q^k} dS\frac{\partial}{\partial n_q}\tilde{G}_{pq}^{N-k}\right. \\
&\qquad \left. -\frac{1}{g}\sum_{l=1}^{L}\int_{\Gamma_l^k} dl\;\sigma_{l}^{k}\,V_{N_l}^{k}\,V_{n_l}^{k}\,\frac{\partial}{\partial n_p}\tilde{G}_{pl}^{N-k}\right\}
\end{aligned} \tag{3.6}$$

The discrete form of the potential (2.12) in the source formulation is found to be

$$\begin{aligned}
\phi_{p}^{N} &= -\frac{1}{4\pi}\sum_{q=1}^{M}\sigma_{q}^{N}\int\!\!\int_{S_q^N} dS\left(\frac{1}{r_{pq}} - \frac{1}{r'_{pq}}\right) \\
&+ \frac{1}{4\pi}\sum_{k=2}^{N-1}\left(\sum_{q=1}^{M}\sigma_{q}^{k}\int\!\!\int_{S_q^k} dS\;\tilde{G}_{pq}^{N-k} - \frac{1}{g}\sum_{l=1}^{L}\sigma_{l}^{k}\int_{\Gamma_l^k} dl\;\tilde{G}_{pl}^{N-k}\right)
\end{aligned} \tag{3.7}$$

3.4 Calculations of the M-Terms in the Linear Boundary Condition

For the linear problem, the m-terms in (2.4) are calculated by two methods. The first (and most common) is to use simplified m-terms which are computed assuming $\mathbf{W} = -U_0\hat{\imath}$. In this case, the simplified m-terms are given by (2.22).

The second technique is to calculate the m-terms using a finite difference scheme. The required terms, Newman (1978), are derived from the normal derivatives of the fluid velocities due to the steady flow on the body surface. The value of the fluid velocities on the body and in the fluid a small distance, Δn, away from the body along the normal vector can easily be calculated from the known solution to the steady Neumann-Kelvin problem, Doctors and Beck (1987). Once these velocities are known, a simple finite difference can be used to determine the required normal derivatives, and these can be extrapolated to take the limit as $\Delta n \to 0$. The procedure works quite well for the semi-infinite fluid problem of the double-body flow. However, when the wave terms are included in the computations for the gradients of the velocities, the results are highly oscillatory, and do not converge for this finite difference scheme. As expected, it is the panels near the free surface that cause the difficulties. Therefore, in Chapter 5 results are presented only for simplified and double body m-terms.

3.5 The Nondimensional Form of The Green Function

The time domain Green function given by (2.9) is written as

$$G(P,Q,t,\tau) = \left(\frac{1}{r} - \frac{1}{r'}\right)\delta(t-\tau) + \tilde{G}(P,Q,t,\tau)\,H(t-\tau) \tag{3.8}$$

By a suitable transformation, the oscillatory part, $\tilde{G}$, can be recast into a non-dimensional form which depends on only two variables:

$$\tilde{G}(P,Q,t,\tau) = \sqrt{\frac{g}{r'^3}}\hat{G}(\mu,\beta) \tag{3.9}$$

$$\begin{aligned}
\hat{G}(\mu,\beta) &= 2\int_0^\infty d\lambda\sqrt{\lambda}\sin\left(\beta\sqrt{\lambda}\right)e^{-\lambda\mu}J_0\left(\lambda\sqrt{1-\mu^2}\right) \\
\lambda &= kr' \\
\beta &= \sqrt{\frac{g}{r'}}(t-\tau) \\
\mu &= -\left(\frac{z+\zeta}{r'}\right) = 1/\sqrt{1+R^2/(z+\zeta)^2} \\
r' &= \left((x-\xi)^2+(y-\eta)^2+(z+\zeta)^2\right)^{\frac{1}{2}} \\
R &= \left((x-\xi)^2+(y-\eta)^2\right)^{\frac{1}{2}}
\end{aligned}$$

The parameter μ relates the vertical to horizontal distance between source (Q) and field (P) points, and β is time like and relates to the phase of the generated waves. The function is oscillatory for large β and is sharply peaked (though not singular) for μ near 0.

3.6 General Computational Considerations

In typical boundary integral techniques, the influence of each of the several hundred panels on the body surface is required for each other panel. Thus, there are $O(M^2)$ repetitive, independent calculations to form the influence matrix, where M is the number of unknowns. The techniques used here to improve efficiency of the computations on a supercomputer are not limited to this particular problem, nor to one class of machines, but are equally applicable to many boundary integral solutions, (and indeed many other $O(M^2)$ methods), on a variety of vector/parallel machines.

The boundary integral formulation of equations (3.1) through (3.7) contain both line and surface integrals, and include convolutions over the entire past history of the motion. (Those familiar with supercomputer calculations immediately recognize

these as long, potentially vectorizable nested DO loops.) Because of the history dependence, over 80 percent of CPU time is spent evaluating these terms. In order to proceed with realistic computations, fast techniques for evaluating the Green function are imperative for adequate representation of complicated body geometries. Each Green function evaluation is independent, and hence the calculations are subject to vector and parallel processing.

Though many existing solutions have employed sophisticated computational methods, little has been done (until quite recently) within the field of Naval Architecture to exploit the inherent parallelism of this class of problems. Many present-day codes have been optimized for performance on scalar machines by minimizing memory storage requirements and the number of operations per call. These are not the same requirements to be met for efficient vector processing, Ginsberg (1985).

The requirements for efficient vector and parallel processing are quite similar. For instance, there must be a large number of independent calculations to be performed, and there should be a minimum of data movement between the processors and the memory, as well as little contention for access to the data. So an algorithm which vectorizes well may also map well onto parallel architectures.

Several impediments must be overcome in order to efficiently utilize the power of vectorization. The first is the complicated form of the time-domain free surface Green function which involves an infinite integral over wave number, and requires several numerical schemes for efficient computation. Each scheme or algorithm is in itself a sizable block of code, and choosing between these schemes requires IF statements— an impediment to high performance on all current vector processors.

In addition, other routines which call the Green function subroutines, compute geometric quantities, perform integrations and matrix operations must be structured with the required sets of long inner DO loops. Hence, one is faced with writing or rewriting large blocks of highly complex code. Fortunately, however, the 80-20 rule

often applies, that is, an 80% improvement can be achieved by concentrating efforts on roughly 20% of the code.

However, the curve of speed versus percent of vectorization is a steep one. In order to reach high processing speeds, one needs to efficiently process the great majority of operations. Optimizing just a few routines is not enough to insure good overall performance for the entire program, as the remaining scalar code will dominate the execution time. This is a qualitative statement of the principle of Ahmdahl's Law, Levesque and Williamson (1986).

The question arises as to the value of time spent optimizing in a research environment, where computer code is constantly changing. The answer depends primarily on whether the code will be used many times or only rarely. It has been found that once a code is vectorized, little extra work needs to be done when rewriting to maintain the vector capability. A well-designed modular structure (with all the implications) is the best practical solution, so that when developing new code, one already has a good basis from which to work, and many subroutines can be utilized without much modification.

As opposed to typical scalar machines on which optimization pays off in a few percent speed increase, the potential gains on a vector processor, and the resulting ability to solve problems involving large data sets and billions of operations warrant the extra time spent. For the time being, a clear picture of the behaviour of many three-dimensional time-dependent problems can only be had with the better resolution attainable with a supercomputer, and the more efficiently we use that supercomputer, the clearer that picture will become.

3.7 Survey of Available Techniques

An example of typical scalar (or unvectorized) performance is exemplified by the code developed by King (1987). This code was developed for use on an IBM 3090 without

vector facility. In its original form, the algorithm for computing the time-domain Green function contained four different expansions, with the choice of method based on the values of the two nondimensional parameters described above. A recursive series of Legendre polynomials which required as many as one hundred terms for sufficient accuracy, a Filon quadrature (also recursive), a Bessel function expansion, and a scalar asymptotic series were employed. About 75 microseconds were required for each evaluation of the Green function and its spatial derivatives on a CRAY X-MP. Approximately 80% of the CPU time was spent in these routines, so this was the natural place to begin optimizing.

Several other researchers have worked on efficient time-domain Green function calculations. Ferrant (1988) presented a method for interpolation of the Green function. What was computationally most remarkable about this work was that body-exact calculations for submerged bodies, and linear motion computations were performed for a wall-sided body (a TLP) at zero forward speed on a VAX 8700—a scalar machine.

Based on run-time statistics, Ferrant was able to assume that the value of the parameter μ was rarely near zero, where the Green function is most oscillatory. This assumption allowed the use of a simple bi-quadratic interpolation scheme with constant grid spacing which covered most of the μ range. The small μ values were handled by a method similar to King's Legendre polynomial series, which although costly, was rarely needed. While his assumption is generally true for the submerged bodies which he considered, for surface-piercing bodies, in particular for long slender ships which have forward speed, it is not the case.

In addition, for computations on a vector machine, the required IF statement to deal with rare cases can degrade the performance of the entire computation, if not handled properly. The rule of thumb on the CRAY is that a fully vectorized calculation runs about ten times faster than a scalar calculation with the same number

of operations. Thus, if 10% of the operations fail to vectorize, the overall CPU time will be 1.9 times larger than a fully vectorized version.

The present method was first described in Magee and Beck (1988b). The method uses two regimes for the Green function calculation— an interpolation regime for $\beta < 10$ and an asymptotic regime for $\beta > 10$. In order to reduce the data required for the interpolation scheme, an approximation is first subtracted from the Green function, and the remainder is interpolated over a grid using bi-cubic polynomials.

Somewhat later, Newman (1991) (actually presented in 1990) and Lin and Yue (1990) also presented methods for vectorized time-domain Green function calculations on a supercomputer. In the interpolation regime both used a two-part calculation scheme which employed a two-term stationary phase approximation as a subtraction function, and a high-order Chebyshev polynomial for the remainder. Both have proven quite sucessful and Newman has extended his method for the case of finite depth. While these methods require little data, it is felt that the computational burden of the two-term stationary phase approximation (which involves several calls to the exponential function), and the fifth-order polynomials (which require more operations than a low-order scheme) is not warranted, given the availability of vast supercomputer memory. An asymptotic routine was used for large values of β.

3.8 The Interpolation Regime

The vectorized Green function code was originally developed for the CRAY X-MP. Because of the stringent 4 million word (MW) maximum program size on this machine (1 word is 64 bits, the default real number on the CRAY), it was necessary to keep the interpolation data set relatively small. Similar to Newman, a first approximation is made, and this is subtracted to obtain a smoother function which can be more easily calculated by the interpolation scheme.

Wehausen and Laitone (1960) have shown that when both source and field points lie on the free surface (that is, for $\mu = 0$), the Green function reduces to the following form in terms of Bessel functions of the first kind:

$$\hat{G}(0,\beta) \equiv \hat{G}_0(\beta) = \frac{\pi\beta^3}{8\sqrt{2}}\left\{J_{\frac{3}{4}}(\alpha) * J_{-\frac{3}{4}}(\alpha) + J_{\frac{1}{4}}(\alpha) * J_{-\frac{1}{4}}(\alpha)\right\} \qquad (3.10)$$

where,

$$\alpha = \frac{\beta^2}{8}$$

The form of the asymptotic expansion when $\mu \neq 0$ suggests a dependence on $exp(-\beta^2\mu/4)$ so that the Green function can be calculated as

$$\hat{G}(\mu,\beta) = \hat{G}_0(\beta) * e^{-\beta^2\mu/4} + \hat{G}_i(\mu,\beta) \qquad (3.11)$$

where $\hat{G}_i(\mu,\beta)$ is the part which must be interpolated over the grid. The two functions $\hat{G}(\mu,\beta)$ and $\hat{G}_i(\mu,\beta)$ are shown in figure 3.1. As can be seen in the figure, the simple function is a good approximation, especially near $\mu = 0$, where $\hat{G}(\mu,\beta)$ is most oscillatory. About 95% of the function is accounted for by the subtraction function which is used for $\mu < 0.6$.

Decomposing the function into these two parts allows a much larger grid spacing to be used than would have been possible without the separation. However, except for $\mu = 0$ (where $\hat{G}_i = 0$), the analytic approximation is not perfect, and $\hat{G}_i$ is still oscillatory. A nonuniform grid spacing with a simple dependence on μ and β was needed to further reduce the data requirements.

The choice of this subtraction function is an important factor, and determines if one is emphasizing an analytic or computational approach to the Green function calculation. When developing the present approach, a single term asymptotic function was tried as a subtraction function, but it was found to be a worse fit, and also to cost more to compute than the function chosen here. The two term approximation used by Newman would provide a better fit, but must be even more expensive.

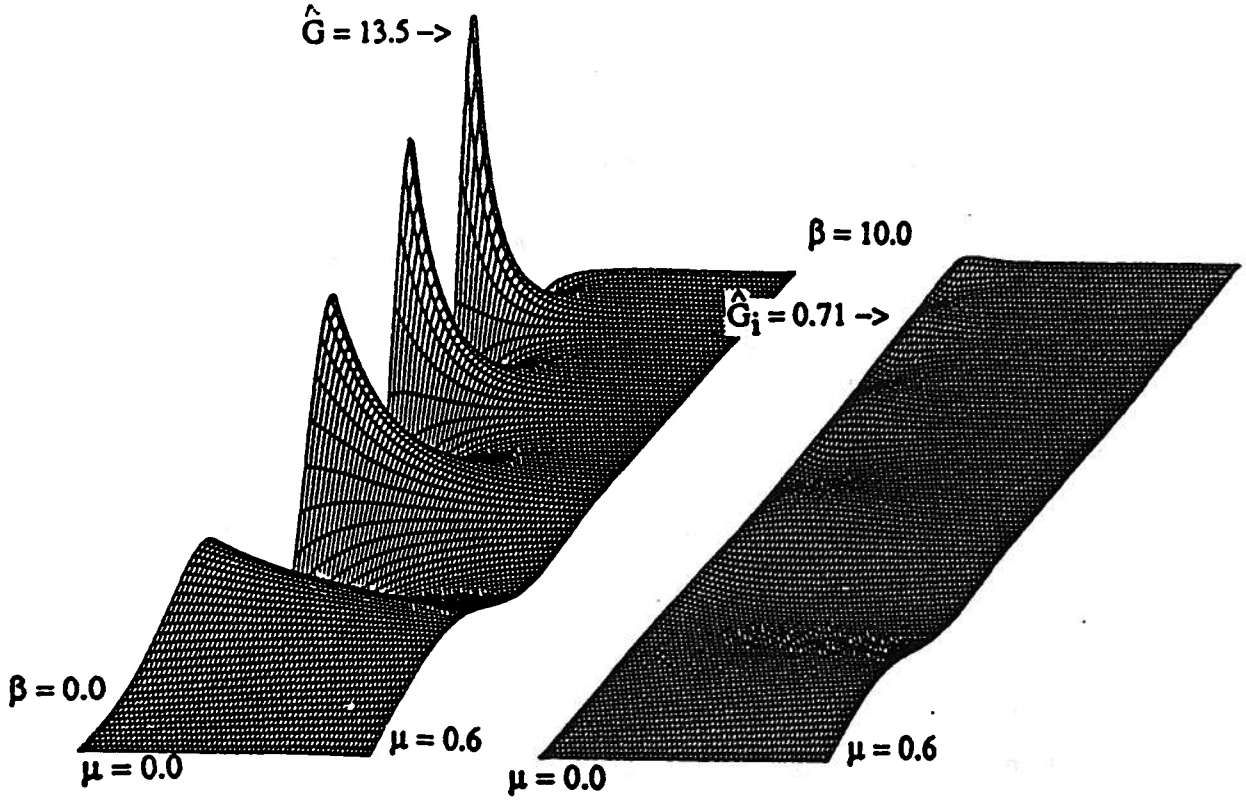

Figure 3.1: The time-domain green function $\widehat{G}(\mu,\beta)$ and $\widehat{G}_i(\mu,\beta)$, the portion which must be interpolated over the grid

The interpolation scheme uses a bi-cubic polynomial. The interpolated part is calculated as

$$\hat{G}_i(\mu,\beta) = \sum_{m=1}^{4}\sum_{n=1}^{4} C_{mn}\, u^{m-1}\, v^{n-1} \tag{3.12}$$

where (u,v) are the normalized coordinates over a grid cell.

The derivatives are calculated as

$$\begin{aligned} \frac{\partial \hat{G}_i}{\partial \mu}(\mu,\beta) &= \frac{\partial \hat{G}_i}{\partial u}\frac{\partial u}{\partial \mu} \\ \frac{\partial \hat{G}_i}{\partial \beta}(\mu,\beta) &= \frac{\partial \hat{G}_i}{\partial v}\frac{\partial v}{\partial \beta} \end{aligned} \tag{3.13}$$

The subtraction function $\hat{G}_0(\beta)$ and its derivatives are calculated using a similar cubic scheme, and then multiplied by the exponential function, but the interpolation is a function of only one variable.

3.9 Vectorization of the Calculations

Vectorization has been achieved by moving the column loop of the influence matrix calculations into the Green function subroutines. A routine which calculates a pointer array decides which of the M Green function calls belong to which expansion. Here, M is the number of unknowns. This separates the μ and β vectors into input subvectors for the asymptotic and interpolation subroutines. A CRAY routine 'WHENFLT' can be used for this purpose, but a Fortran IF-statement is nearly as fast, is transportable, and vectorizes using the *cft77* compiler with the '*−oaggress*' option.

Simple IF statements within a loop will vectorize on the CRAY. Experience has shown that the maximum speed achievable with such a 'conditionally vectorized' loop is somewhat less than a fully vectorized loop. Actual performance varies with the density of truths and with the required executable code for each branch. It is

often better to execute a loop with all the IF's separately so that the full speed may be brought to bear on separate loops containing most of the computations.

The subvectors are then passed to the interpolation and asymptotic routines which calculate the nondimensional Green function and its two derivatives in vector mode. The results are scattered back to fill the appropriate elements of the influence coefficient matrix. Although these subvectors will necessarily be less than M in length, they tend to be long enough for efficient processing. In fact, the required vector length for increased performance over unvectorized calculations is always less than ten, and this is nearly always achieved for normal discretizations.

In general, random access to memory to fetch the polynomial coefficients has not slowed calculations on the CRAY X-MP or the Y-MP significantly. These machines have separate vector address registers which have their own pipelines. These processors operate independently from the floating point units, and hence do not interfere with them. On machines without efficient indirect addressing, such as a CRAY-1, the vector of interpolating polynomial coefficients can be compressed into contiguous memory. This should speed the evaluation of the polynomials on such machines by avoiding the need to access noncontiguous addresses in the loop which actually does the calculations. However, on the Y-MP, with hardware GATHER-SCATTER the extra overhead of doing the compression separately is usually greater than the savings obtained by having continuous addressing in the calculation loop. The preferred method changes depending on the vector length and the density of the pointers in each routine. Long vectors, and very skewed densities (more hits in the interpolation routines) favor contiguous memory access, but only very slight differences are detectable. Ideally, one could set up two routines to take advantage of the two cases, but this has not been done because the potential gains do not warrant it.

A memory access bottleneck can occur when the same memory bank is addressed twice before a suitable time has elapsed for it to be ready. The probability of two

hits in the same bank depends mainly on the number of banks and on their speed. On the CRAY Y-MP, with 128 memory banks, with a bank cycle time of about four clock cycles, it is nearly impossible to have memory conflicts, unless one is accessing memory with a stride of 128 or a multiple of that number.

The number of floating point operations per memory reference is also a crucial factor in determining the speed at which a loop will run. One reason is that with a larger number of operations per memory reference and such fast memory, the bank cycle time often may elapse while processing the arrays already in the vector registers. Nevertheless, a conflict can occur when one needs two sets of polynomial coefficients with at least some elements contained in the same bank. For a smaller number of subregions, there is a larger probability of having to re-access the coefficients from the same subregion consecutively within the vector loop.

For $\beta > 10$ the asymptotic expansion of the Green function, King, 1987, was retained, and the special expansion was used for μ near 1.0, where the usual asymptotic expansion becomes singular. This routine is fully vectorized.

The calculation of the infinite fluid terms is performed using the method of Hess and Smith (1964). These routines have also been vectorized with a resulting speed up of eight to twelve times. Restructuring was required since these algorithms contain many branches. The actual speed depends on the distribution of points in the monopole, dipole, and exact regimes for the integrals. The convolutions are also fully vectorized, and automatic loop unrolling can be performed on these loops by the compiler.

3.10 Evaluation of the Method

The interpolation routines are fast and accurate. They run at about 140 million floating point operations per second (MFLOPS). The Y-MP has a maximum possible speed of 333 MFLOPS on one CPU. Between 2.6×10^{-6} and 3.5×10^{-6} CPU

seconds are required for one evaluation of the Green function and its three spatial derivatives— a factor of twenty to thirty less than those used by King on the X-MP. Ferrant (1988) gives CPU times only for his entire computation, which include large amounts of unvectorized convolutions, since these were performed on a VAX 8700. Overall, the CPU times for similar calculations are 80 to 100 times less on the CRAY X-MP than the VAX, which seems reasonable when one compares the potential speeds of the two machines.

The CPU times for the various Green function routines, as they were employed in the linear time-domain program, are given in figure 3.2. The calculations are for a modified Wigley seakeeping hull at Fn=0.0 using 240 panels on the half-body and 256 time steps, and for the SL-7 containership at Fn=0.2, using 212 panels on the half-body and 127 time steps. A 2 by 2 Gauss quadrature rule was used for integration of the wave terms over panels. The Wigley hull results are presented in Chapter 5 and those for the SL-7 are included in Magee and Beck (1988a).

The percentages of overall CPU time for the various routines are given in figure 3.3, and the MFLOP rating, as determined by the performance monitoring software on the CRAY Y-MP, is shown in figure 3.4. The vector length has an effect on the CPU time per evaluation, but a study of speed versus vector length will not be included here for brevity. The optimal vector length on the CRAY Y-MP and X-MP is not, as is sometimes stated, sixty-four (the length of the vector registers), but rather, a larger multiple of sixty-four. Thus, 256 panels would probably produce slightly faster times per Green function evaluation than those presented here.

The subroutine *VGREEN* performs the transformation between dimensional (x, y, z, t) variables and the (μ, β) space, and also the transformation from $(\widehat{G}, \frac{\partial \widehat{G}}{\partial \mu}, \frac{\partial \widehat{G}}{\partial \beta})$ to $(\widetilde{G}, \frac{\partial \widetilde{G}}{\partial x}, \frac{\partial \widetilde{G}}{\partial y}, \frac{\partial \widetilde{G}}{\partial z})$. It is to be noted that a large number of operations are required for these calculations, but when processed in a vector loop, they are quite fast. The routine also calls other routines which determine to which expansion each Green func-

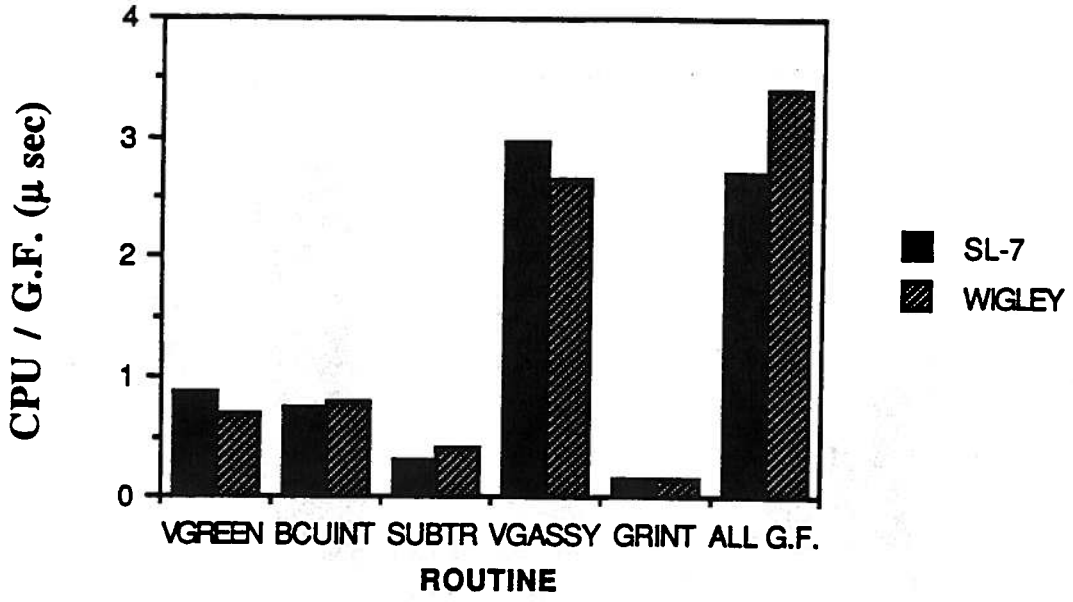

Figure 3.2: Average CPU time for various Green function routines

tion call belongs, and hence those routines' CPU time is accounted for in the time for $VGREEN$. Finally, the calculations of the normalized coordinates on the grid cells for the interpolating polynomial is also included here. The routine $BCUINT$ performs the bi-cubic interpolation calculations of (3.13). About 100 floating point add and multiply operations are required for each evaluation of the nondimensional Green function and its two derivatives. The routine $SUBTR$ calculates the nondimensional subtraction function and its derivatives. The routine $VGASSY$ calculates the asymptotic expansion used for large β values.

The CPU time per Green function varies depending on the relative number of calculations in each regime. The asymptotic form is more expensive to compute, although it runs at higher MFLOPS. Thus, for the longer time record used for the Wigley hull, which involves more calls to the asymptotic routine, a larger CPU time per call is required, and a higher MFLOP rating is obtained.

Newman quotes a CPU time for his interpolation regime of one microsecond. This includes the two-term stationary phase approximation. While this appears to

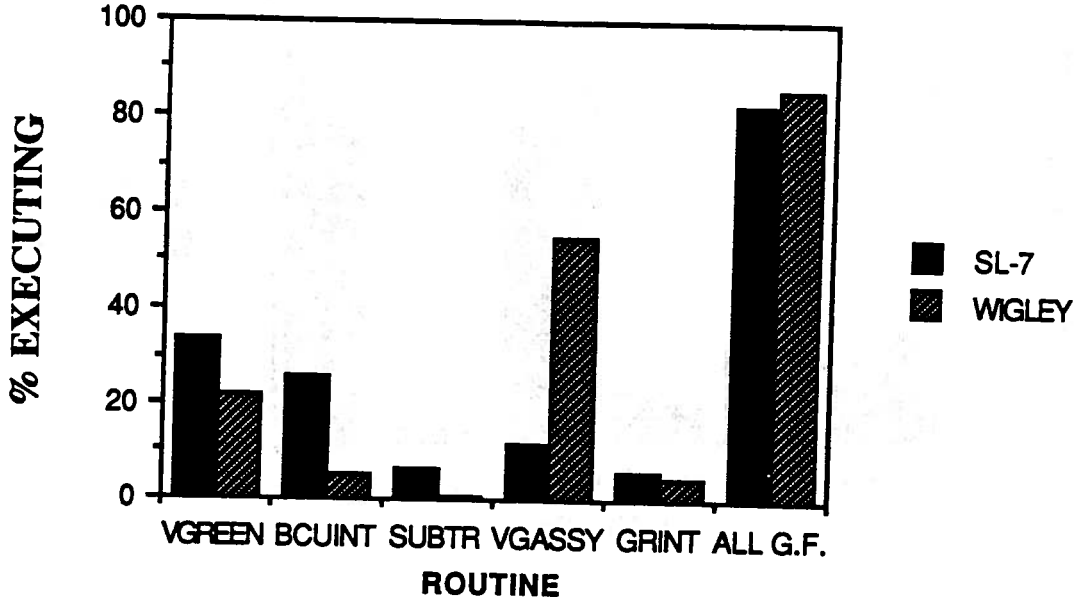

Figure 3.3: Percentage of overall CPU time spent in each of the Green function subroutines

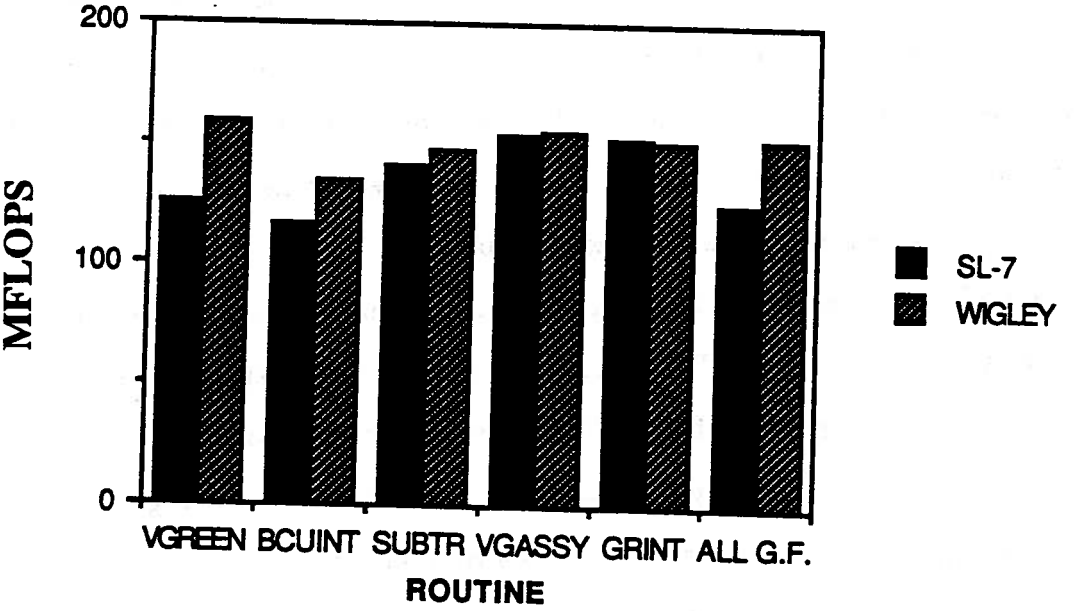

Figure 3.4: MFLOP ratings for the various Green function routines

be very fast, it does not include several other important parts of the calculations. For instance, the CPU time for the large-β stationary phase routines was not given. The time to perform the transformations to and from nondimensional space was also not included in this number. The length of the vectors was not given, nor was the type of calculation on which the routines were timed. Furthermore, it was not even specified on which CRAY the calculations were performed— a CRAY-2 or a Y-MP. However, space limitations and the varying interests of the audience for which the paper was written probably justify the omission of these important details. Lin and Yue (1990) gave an estimate of one to three microseconds per evaluation of the Green function and its derivatives for body-exact calculations, but it is not clear how much overhead is included elsewhere. However, these numbers seem fairly reasonable.

The bi-cubic approximation gives a function which has a maximum error near the one-quarter points of a grid cell. The error in the derivatives is a maximum near the center. The values of the Green function and its derivatives were checked in each grid cell at these points, along the edges of each cell, and at smaller intervals within the cell, against the output King's algorithms which were used to derive the coefficients. The maximum absolute errors were found to be less than 1×10^{-8} for the Green function and 1×10^{-6} for the derivatives.

The accuracy of Ferrant's interpolation scheme was not given, except that the final results showed no significant difference when compared to results obtained using semi-analytic methods for the Green function evaluation. Since only a limited number of Green functions can be calculated in a given amount of CPU time, there is a tradeoff between the numerical error made in calculating the Green function and the discretization error made in using a finite number of panels and a given time step size. The question of global versus local accuracy has not been thoroughly investigated.

Newman has argued that if the validation of the overall numerical method de-

pends on convergence studies, then high accuracy is necessary. Certainly, the method he has developed has excellent accuracy. Ideally, one would like a method that was adaptive to the computer environment available. Greater accuracy could be obtained by say, decreasing grid size, if memory was available. On a slower machine, some accuracy could be sacrificed in favor of a larger number of Green function calls—each less accurate but with a lower CPU requirement. The Chebyshev polynomials appear to be the best choice for such an adaptive method.

The subtraction function used here requires only one call to the exponential function instead of the several required by the two-term stationary phase approximation. A savings in the number of operations is also realized by using cubic instead of a fifth-order polynomials. However, a small extra cost is incurred in calculating the grid cells due do the nonuniform spacing.

The final data requirement is about 2 MW. While this may seem to be a large number, it is well within the available memory of most present generation vector processing machines. The coefficients are stored in a file which is read in at the beginning of the time-domain computation. The initial set up requires less than 0.1 CPU second using $BUFFER\ I/O$ on the Y-MP.

3.11 Application of Vectorized Calculations to the Linear Code

A speed increase of 32 times for the entire linear program over the unvectorized version has been achieved for a typical calculation on the CRAY Y-MP. The case of an SL-7 containership at $Fn = 0.2$ was used for a 7 degree of freedom calculation using $M = 212$ panels (on one half of the body), 127 time steps and a 2 by 2 Gauss quadrature rule for each panel. Including line integral terms, this calculation required a total of 145×10^6 Green function evaluations. The total CPU time was $3.1 \times 10^{-6} \times N_T$ seconds, where N_T is the total number of Green functions required. This number includes all the calculations from start to finish for the entire program.

A CPU time of 14,000 seconds for the unvectorized code has thus been reduced to 450 seconds for the vectorized version, and what was once an upper limit on temporal and spacial discretization now has rather moderate computational requirements.

The restructuring of the linear program was quite interesting. In the original scalar code, the required CPU time was split approximately 85%/5%/10% respectively between Green function evaluations, left hand side manipulations (setting up and solving the system of equations), and other calculations such as geometry, I/O and convolutions. After implementing the fast Green function routines, this ratio changed to about 10/40/50, but the whole code was nearly five times faster.

A lot of loop switching and the use of buffered I/O then virtually eliminated the CPU time in the general category, and the majority of the CPU was required by the only remaining scalar code, that is, the calculation of the $1/r$ terms. With about a week's work and some trial and error, these routines were vectorized, and the whole code regained an almost identical distribution of relative CPU requirements, but at a greatly reduced overall requirement.

A very fast LUD solver, LUSP, is available on the CRAY, and with the small number of unknowns used in the present calculations (typically a few hundred), an iterative solver was not used. The time required to calculate the infinite fluid terms—the integrals of $1/r$ and $1/r'$ and their normal derivatives for both combinations of symmetry was 0.72 CPU seconds for the Wigley hull. Decomposing the two matrices required 0.14 CPU seconds. The 256 back substitutions (one for each time step) required a total of 0.2 CPU seconds for each degree of freedom. In all, a total of 2.5 CPU seconds was spent in these parts of the calculation.

Also interesting is that the relative portions spent in each category for the body-exact code remains more or less the same as for the linear solution. In the linear problem the body geometry is stationary in the steadily moving coordinate system, so the left hand side need be computed only once, with only back substitution required

at each time step. In the body-exact code for submerged bodies, the $1/r$ term need only be calculated once, but the $1/r'$ term has to be recalculated once at each time step. Since the wave term is evaluated over the past history (averaging half of the entire linear calculation at each time step) the overall effect is to keep the same proportions in calculations. CPU time for geometry calculations and convolutions also remain approximately proportional. Decomposing the matrix is required every time step, so this portion is increased.

3.12 Possibilities for Parallel Processing

Multitasking can be achieved by using multiple copies of the subroutines or by moving the row loop inside the Green function routines as well. This has not been accomplished as of this date, and it is felt that present efforts need to be devoted elsewhere. The autotasking compiler on the CRAY Y-MP fails to recognize nesting which occurs across subroutine boundaries. Thus, more restructuring of the linear code would be needed to efficiently parallel process on the CRAY. Parallelization of the Green function calculations may prove worthwhile for the nonlinear calculations. The Stellar GS-2000 computer uses multithreading (a form of parallel processing) which allows several tasks to execute simultaneously using some hardware separately, while sharing other parts. The machine has only one vector processor, but several sets of registers which can operate independently to overlap some operations. A speed increase of about 1.5 times for 4 threads (over the single thread speed) indicates a good potential for speed increase using true parallelism. With multithreading, the CPU time for a typical calculation is about 10 times more on the Stellar than on the CRAY Y-MP.

It is believed that the present method will perform well on another important class of machines, namely, vector parallel processors such as the Alliant. The Alliant has up to 28 moderately fast parallel CPUs and a large fast cache of high speed shared

memory, as well as a huge, although somewhat slower RAM. By assuring that the polynomial coefficient data base is small enough to remain within the cache, where it is quickly accessible to all the processors, calculation speed can be improved. The row of influence matrix calculations can be processed in parallel, with each processor operating on a vector or column of Green functions. All the Green functions are independent, and we would expect very good speed from a large number of processors. Of course, it is not reasonable to expect a linear speed increase, i.e., that two processors will run twice as fast as one, because interprocessor communication is necessary, and contention for some of the same data is inevitable, but speeds approaching this ratio are obtainable with a well-designed code.

3.13 Comparison to Frequency-Domain Green Function

It is instructive to examine the form of the potential due to an isolated time-domain source traveling below the free surface. The top part of figure 3.5 shows the time history of the potential for a unit step function source which is created at $t = 0$; thereafter, its strength remains constant. The source is traveling at a depth of $z = -2$ below the free surface with a Froude number, $Fn \equiv U_0/gR = 0.4$, where U_0 is the steady horizontal speed, R is horizontal distance between source and field points, and g is gravity. The field point is traveling on the free surface at the same speed, and is located a distance $R = 1$ behind the source.

The potential due to an impulsive source at the same initial source point is shown in the bottom figure. The field point is moving as in the upper figure. The top figure corresponds to the Green function used by Korsmeyer (1988). The bottom figure is the time-domain Green function used in this work, and is the time derivative of the function used by Korsmeyer. Both Green functions are described in Wehausen and Laitone (1960). The potentials have the form of typical impulse response functions:

there is an initial large response followed a decaying oscillation about the large-time limit.

The frequency-domain singularity at $\tau \equiv U_0\omega_e/g = 1/4$, where ω_e is the pulsation frequency, is also described in Wehausen and Laitone. The singularity occurs at this frequency because the group velocity of some of the waves produced by the translating, pulsating source matches the speed of the source. In the steady-state limit of sinusoidal oscillations, which are assumed to have persisted for all time, these waves do not radiate and hence a singularity occurs. In this case, the critical wave number where $\tau = 1/4$ is $kR = 0.3906$.

The solid lines in figure 3.6 are expanded views of the oscillatory tail of the potentials at large time. The oscillations are at a frequency equivalent to $\tau = 1/4$ and lead to the singular behavior in the frequency domain. Recall that the Fourier transform of a sine wave of frequency ω_0 in the time domain is a delta function at ω_0 in the frequency domain. Thus, the $\tau = 1/4$ singularity appears as a decaying sine wave at the appropriate frequency in the large-time tail of the time-domain results.

Figure 3.7 shows the real and imaginary parts of the Fourier transform of the potential for the impulsive source, which is the frequency-domain Green function used by some authors. This suggests that the time domain Green function could be used for frequency domain calculations, which could be especially useful for forward speed problems where the frequency domain Green function is very expensive to compute, Hoff (1990). One could calculate the Green function and its normal derivative in the time domain, and then Fourier transform the result to be used in solving the integral equation in the frequency domain. The procedure might not be particularly effective because the number of Green function evaluations required to resolve the oscillations caused by the $\tau = 1/4$ singularity is very large. However, the asymptotic form of the Green function, King (1987), or Newman (1991), might be integrable analytically for steady forward speed. In this case, the nondimensional parameters μ and β are

known functions of time. The practicality of such a method needs to be investigated further.

The small squares in figure 3.7 are the values of the frequency-domain Green function taken from Wu and Eatock Taylor (1987). The singular behavior of the frequency-domain Green function at $\tau = 1/4$ is clearly visible. As can be seen, the agreement between the frequency-domain computations and the Fourier transform of the time-domain response is excellent except very near the singularity.

To eliminate the anomalous behavior in time-domain simulations due to the $\tau = 1/4$ singularity, artificial damping can be introduced into the large-time tail of the time-domain Green function. In particular, the large time asymptotic expansion that is used in the Green function subroutines is multiplied by $e^{-\alpha(\beta-\beta_0)^2}$, where α is an arbitrary constant which determines the strength of the damping. Typical values of α are in the range of 0.0 to 0.1. The artificial damping has the effect of forcing the large-time tail of the time-domain Green function to decay more quickly to zero. The dashed curves in figures 3.5 through 3.7 are the results computed using the damping. In figure 3.5, the dashed curve cannot be seen because on the scale of the figure the damped and undamped curves are identical. The effects of damping are clearly seen, however, in the expanded scale of figure 3.6. In this figure, the oscillations are substantially lower, and decay much faster.

The effects of the damping in the frequency domain can be seen in figure 3.7. The damped and undamped curves are effectively identical except around $\tau = 1/4$. In this region, the damping smoothes out the singularity. As the damping coefficient α is reduced, the results become more and more singular. In Chapter 4, the effects of the damping on motion simulations will be shown.

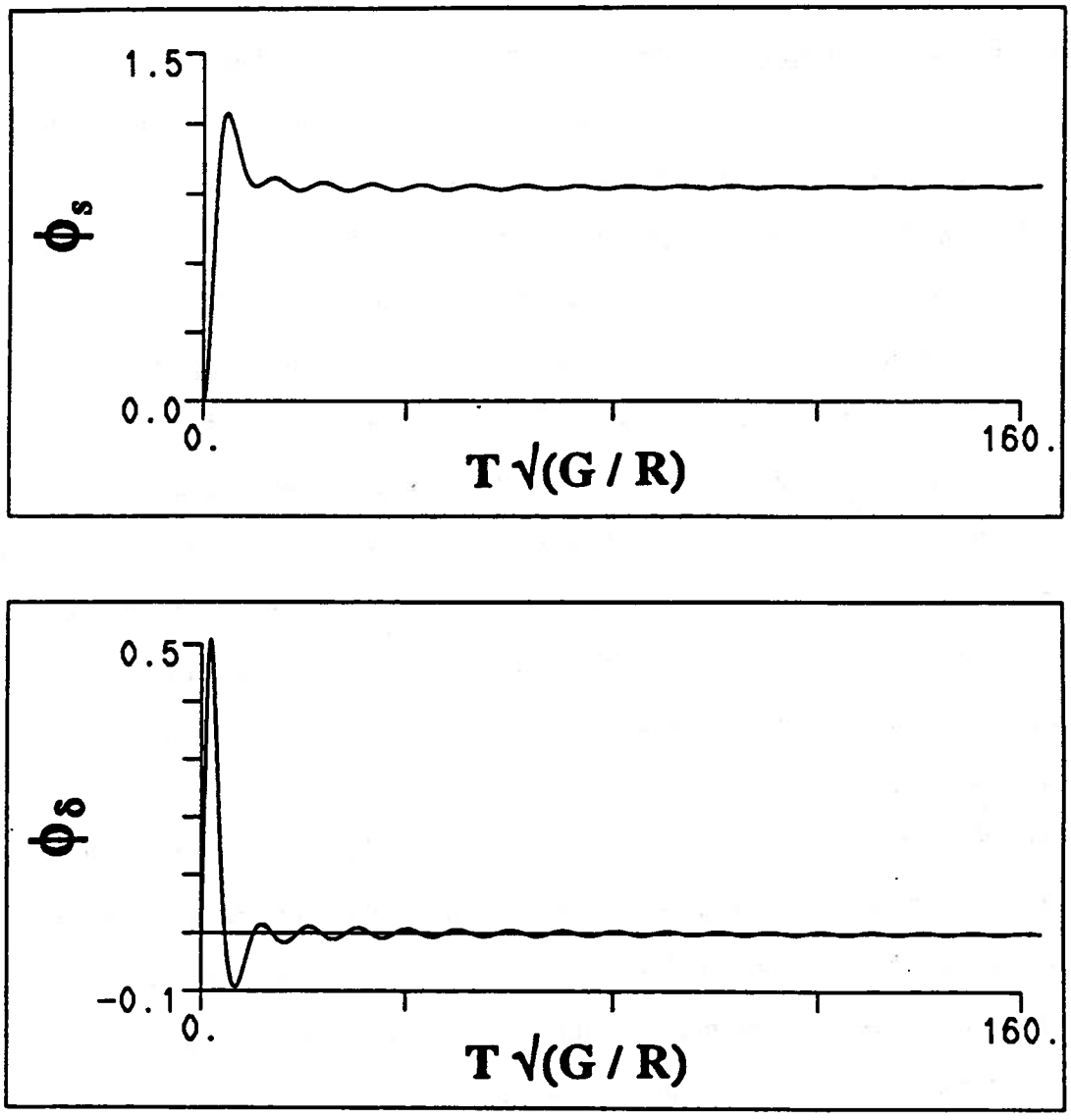

Figure 3.5: The potential for a step function source and an impulsive source

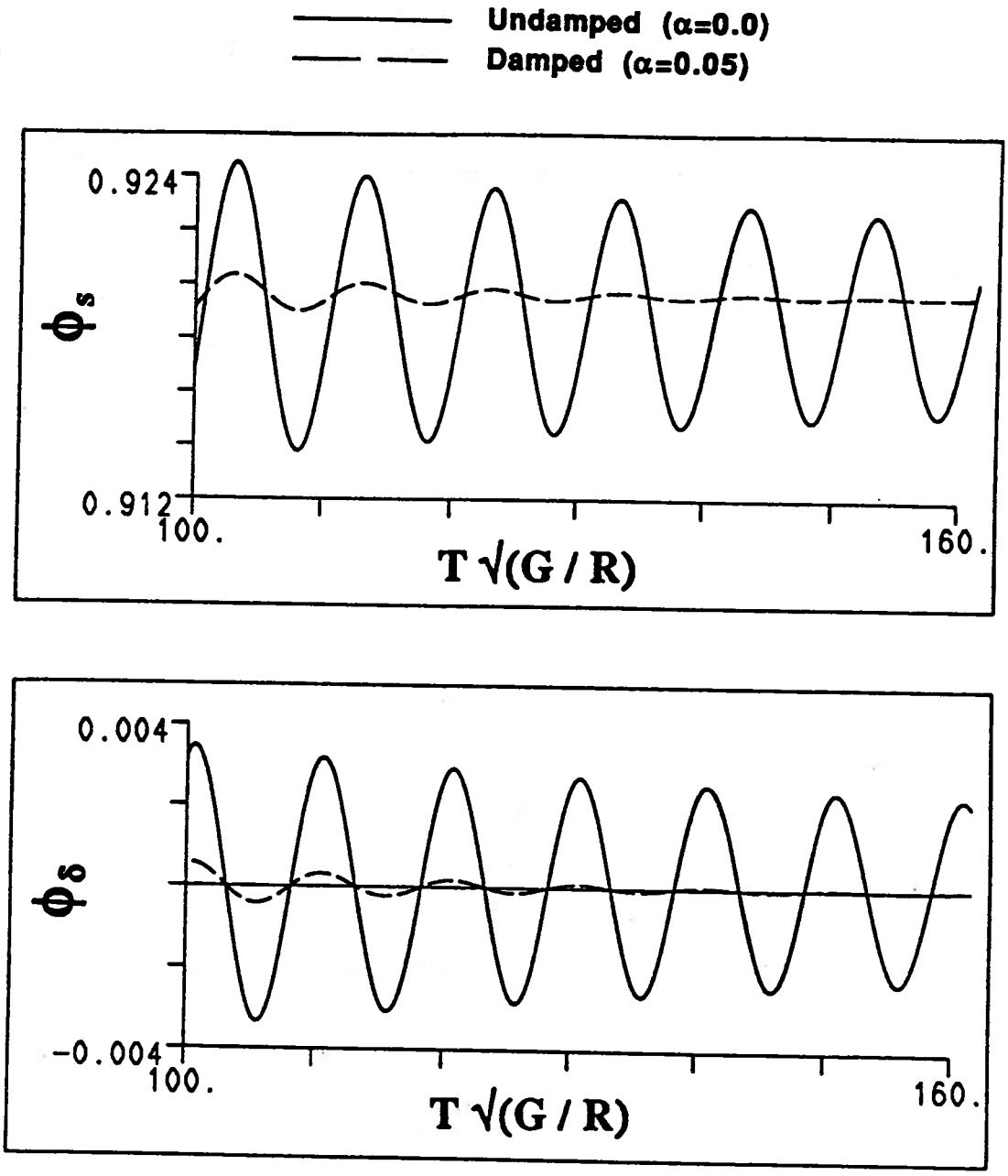

Figure 3.6: Greatly expanded view of the large-time tail of the potentials for the step and impulsive sources

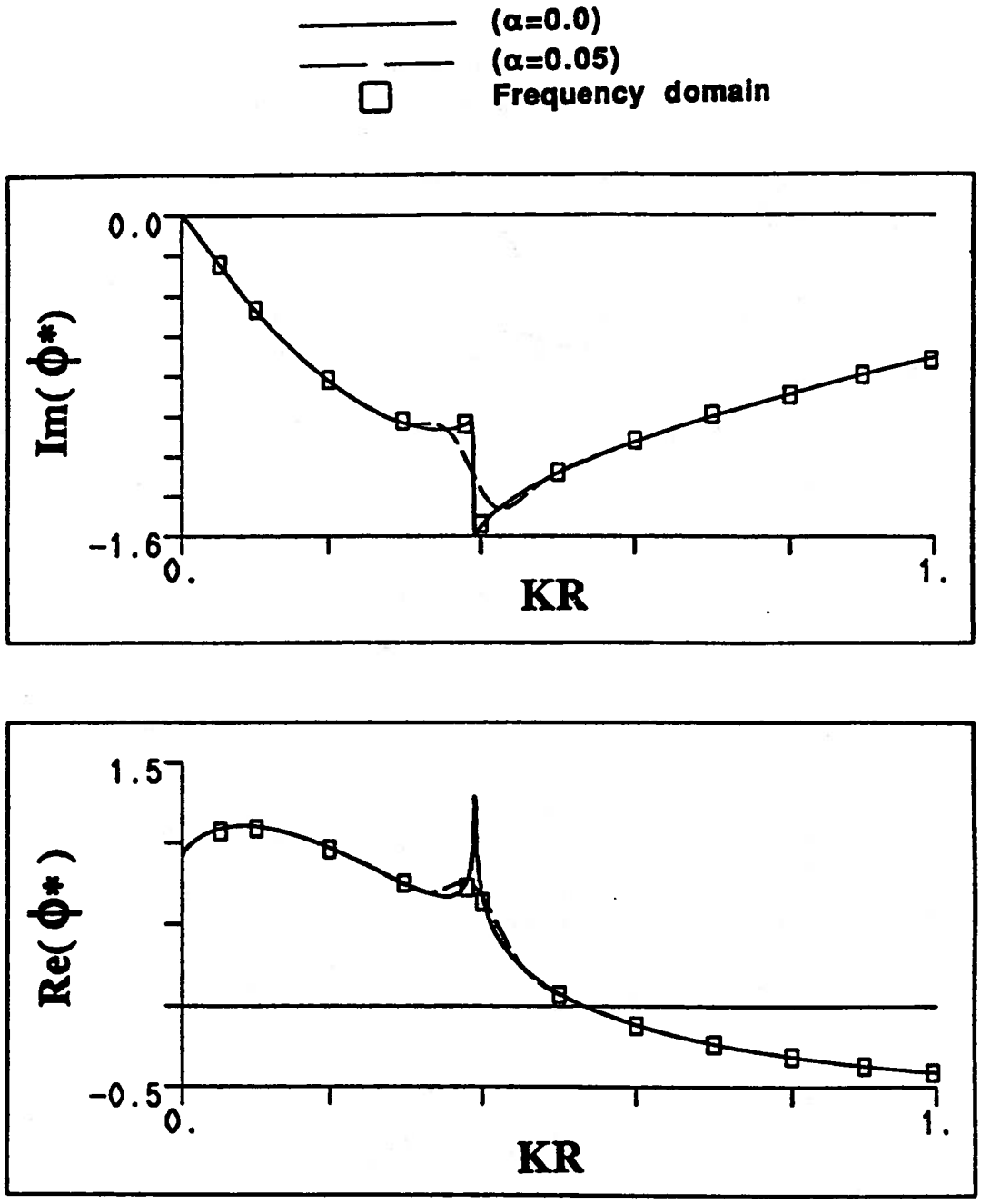

Figure 3.7: Fourier transform of the impulsive source potential

CHAPTER IV

NUMERICAL RESULTS FOR THE BODY-EXACT PROBLEM

4.1 Calculations for a Submerged Sphere

In order to verify the method and to determine its accuracy and convergence properties, initial calculations were performed for a submerged sphere. Analytical and other numerical results were readily available for comparison for certain specified motions.

In order to explore the effects of large-amplitude motions, and because an analytic solution was available, the first comparisons were for the zero frequency ($\partial\phi/\partial n = 0$) and infinite frequency ($\phi = 0$) limits of the free surface boundary condition (2.3). In these cases the Green function given by (2.9) reduces to $G = 1/r \pm 1/r'$, respectively. Since no memory effects are present, the force depends on the instantaneous displacement, velocity and acceleration only, and not on the past history of the motion. Figure 4.1 shows the nondimensional vertical and horizontal forces versus nondimensional time on a sphere which is heaving sinusoidally and also has a steady horizontal speed. The forces at the zero frequency limit is labeled 'R.W.' for rigid wall. The reduced frequency of the oscillations (See Ashley and Landahl (1965) p. 247.) is

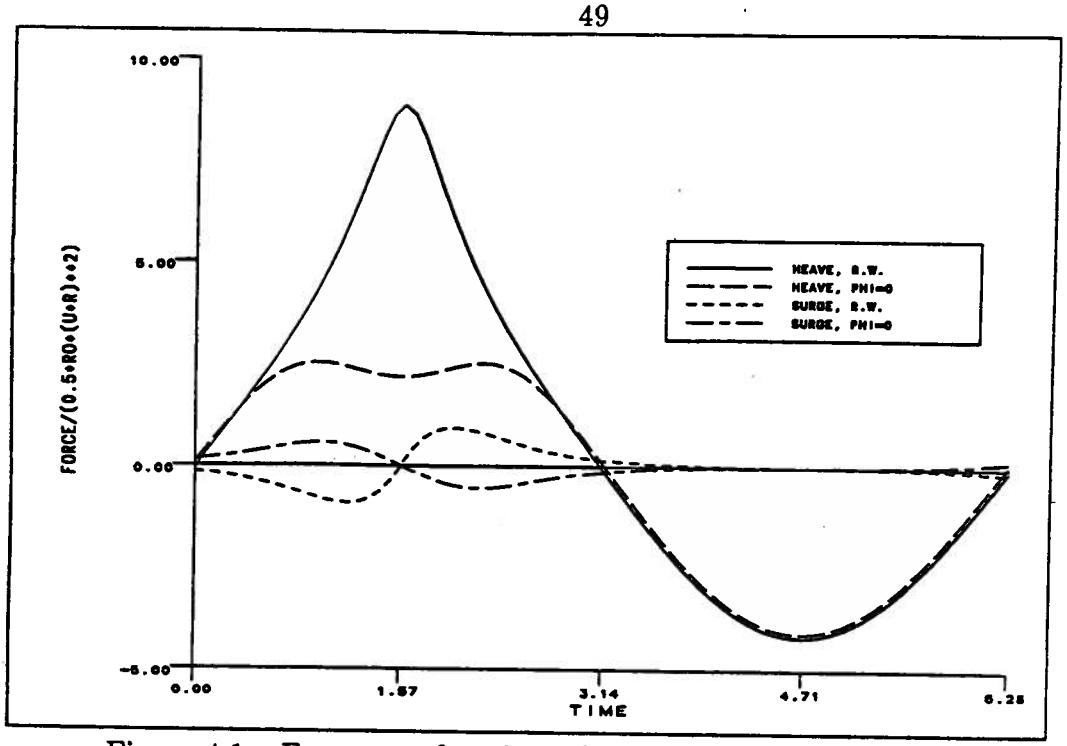

Figure 4.1: Forces on a heaving sphere beneath a $\phi = 0$ and $\partial\phi/\partial n = 0$ free surface

$\omega R/U = 1.0$. The center of the sphere is initially submerged a depth $H_0 = 2R$, where R is the radius, and the amplitude of motion is $A/R = 0.99$, so that the top of the body nearly touches the free surface at the end of the upstroke. The forces exhibit rather interesting trends as the body approaches the rigid wall or the pressure release surface, and tend toward sinusoidal behavior on the deeper half of the cycle. The analytic solution, by Miloh (1977) (not shown in the figure) was obtained by solving an infinite set of simultaneous equations for the coefficients of a series expansion in spheroidal coordinates. In practice, the infinite equation set is truncated at a rather small finite number, depending on the desired accuracy of the result. The numerical results were found by solving for the force using three sets of paneling, (400, 784, and 1296 panels on the half body). Richardson extrapolation was used to find the limit for an infinite number of panels. The potential formulation of (2.10) was used, and the tangential derivatives necessary to calculate velocities and hence pressure in (2.13) were obtained by second-order finite differences in the θ and α directions.

The extrapolated numerical and analytic forces agree to better than three significant figures, even when the sphere is nearly touching the surface. The convergence rate with number of panels is roughly linear for this smooth body. The convergence rate is studied further in Section 4.2.

This study verified the geometric portion of the large-amplitude program. The next step was to add the wave term of the Green function in (2.9), thus implementing the finite frequency free surface condition. Both the potential and source formulation were used to compute the vertical force on a heaving sphere using the free surface condition (2.3). The results are shown in figure 4.2. Also shown are the results by Ferrant (1989) who used a body-exact formulation similar to the present source method. Ferrant's result was taken from a table of coefficients which gave the limits of the in-phase and out of phase components for each harmonic of the fundamental. The time-history was reconstructed by multiplying the appropriate coefficients by their respective sinusoidal variations. Thus, the time-domain solutions are expected to approach this steady limit cycle after some time has passed.

The number of panels on the half body was 100, and the number of time steps per period of the oscillation was 24. The sphere is heaving at an amplitude $A/R = 0.5$ from the same initial depth as the above case, the forward speed is zero, and the non-dimensional frequency is $\omega\sqrt{R/g} = 1$. The solution obtained with the linearized body boundary condition is also included for comparison. The body-exact solution differs from the linear one mainly in the peaks. Its phase is slightly ahead with respect to the linear solution when the body is near the free surface, and the reverse is true on the deeper portion of the cycle. This is a result of the second and higher order harmonics of the force time history which are introduced by the changing body position. While not strictly a nonlinear phenomenon, in this case, the nonstationary geometry captures some very important features which would be present in a fully nonlinear solution.

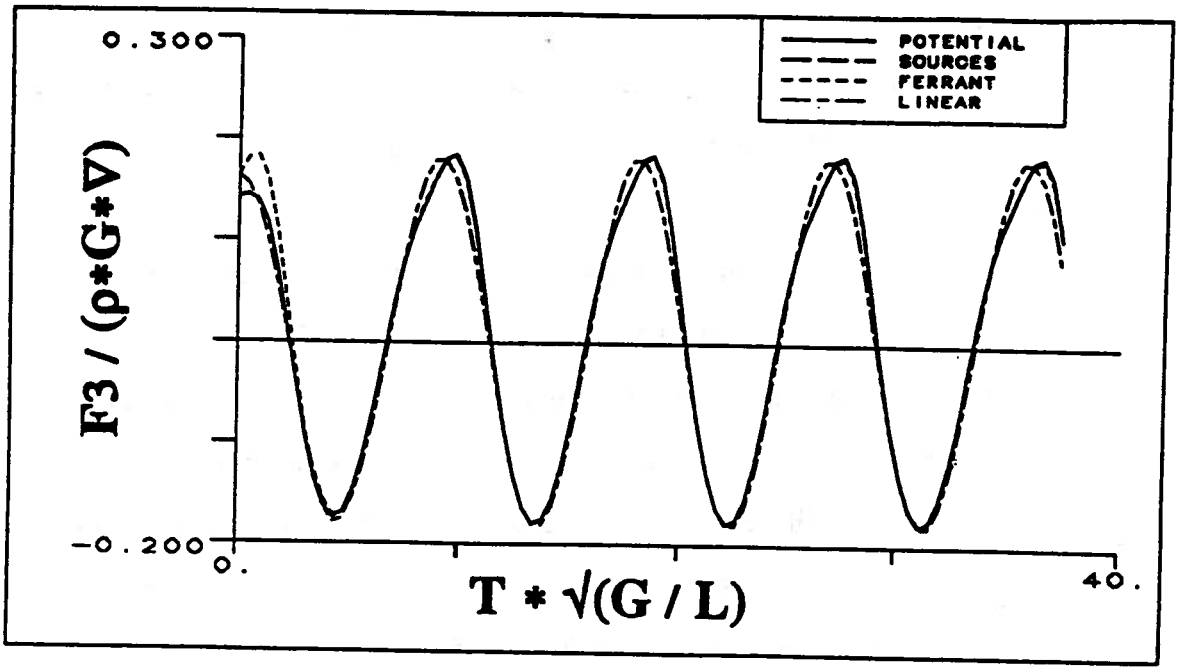

Figure 4.2: Vertical force on a heaving sphere, $A/R = 0.7, K_1R = 0.5, Z_0/R = 2.0$

This case verified that both source and potential formulations were working properly and giving similar answers. The numerical differentiation of the potential to obtain surface velocities works quite well for this smooth geometric body shape, especially since the required transformations between tangential and global coordinates are known analytically. Similar calculations for an ellipsoid provided slightly worse answers, especially near the ends of the body where geometric and flow quantities vary rapidly— this despite the existence of a locally orthogonal surface coordinate system for the ellipsoid given by Miloh and Patel (1973). For arbitrary geometries, it was felt that this method was not very promising, and given the ease with which the velocities could be obtained from a source distribution method, the potential method for body-exact calculations was at least temporarily dropped.

Nevertheless, the superior properties of the direct application of Green's theorem, most notably reduced effects in the vicinity of irregular frequencies for surface-piercing bodies, are well known, Adachi and Omatsu (1979). It would be desirable

to keep this quality of the solution method, while at the same time developing a robust method for computing tangential surface velocities. One alternative is to differentiate the Green function. However, the derivatives may be highly oscillatory, compounding the already difficult problem of panel and line integrations. A linear or quadratic variation of the potential over a panel or between node points might allow a better approximation to be made for velocities, while still maintaining the superior qualities of the direct method. A spline method similar to the one used by Nakos (1990) and Sclavounos and Nakos (1990) which allows quantities of interest to vary smoothly over the body surface could be implemented. In addition, the nature of the time-domain problem allows one to think of time as the third variable, and a three-dimensional spline surface (two dimensions over the body surface, and the third in the time direction) might be useful for evaluating convolutions. While this method has not been implemented it holds promise for future work.

Figure 4.3 shows the wave elevation versus nondimensional time predicted by the source distribution method for a heaving sphere at zero forward speed. This is a case that was studied by Ferrant (1989). The nondimensional wave number is $K_1 R = \omega^2 R/g = 0.279$— a case for which the higher order harmonics produced by the changing body position are important in determining the wave elevation. The amplitude of motion was $A/R = 0.5$. The number of panels used in the calculation was $M = 100$ on the half body, and 24 time steps per cycle were used. Both linear and body-exact solutions are shown. The wave elevation versus time is shown at a horizontal distance of $D = 16.5\ R$. Experimental values were obtained by Dassonville (1987). According to Ferrant, "A small difference in the starting transient is observed, due to the smooth start of the experimental apparatus. ...At large time, the comparison is not significant, the experiments being affected by tank wall reflections."

Near the middle of the time record, the agreement between body-exact calcu-

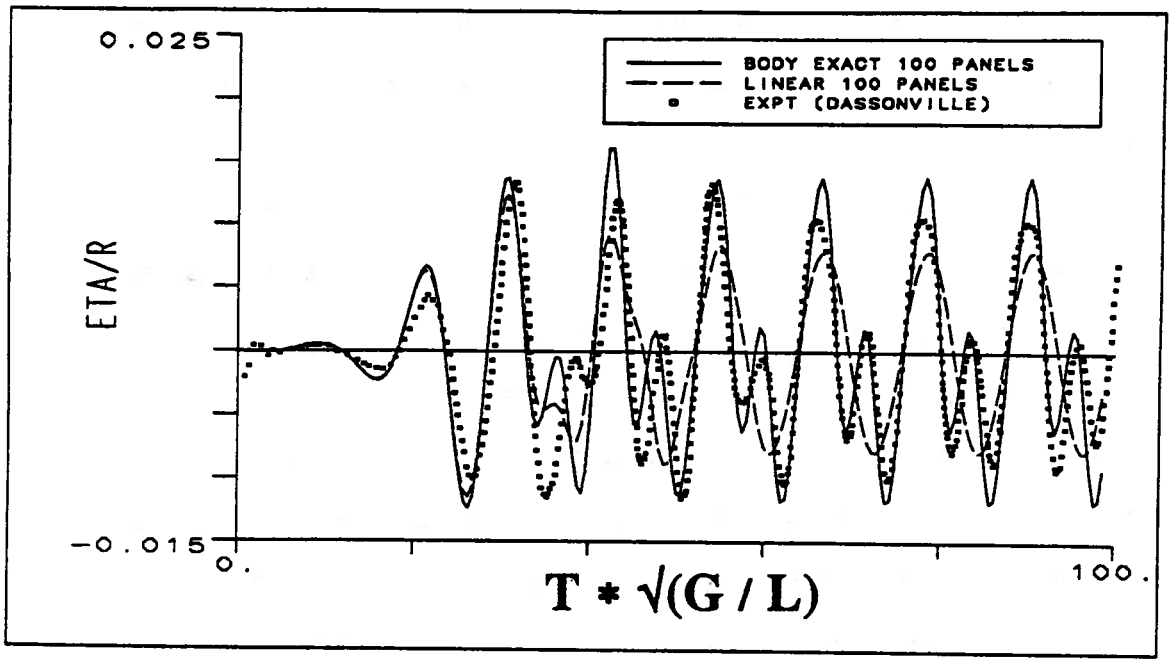

Figure 4.3: Wave elevation versus nondimensional time for a heaving sphere at a horizontal distance D=16.5 R

lations and the experimental values is good for the phasing, although the peak values are over-predicted by the calculations. The linear solution misses the very strong higher harmonics which are well captured by the body-exact solution. Ferrant pointed out that these harmonics in the radiated wave field are more important at moderate frequencies than at very high or very low frequencies.

4.2 The Unsteady Forward Speed Problem

Having more or less mastered the solution for submerged bodies at zero forward speed, the next step was to try to add forward speed. In direct contrast to the frequency domain method, in which the required Green function is much more difficult to compute, the time-domain method allows the same, relatively simple form of the Green function to be retained for arbitrary motions, including (but not limited to) steady forward speed. Thus, in principle, the only extra difficulty encountered with

forward speed is the addition of the line integral terms in (2.11). For the submerged body, however, these are zero, and little else needs to be done than to modify the input for the specified motion.

Before combining the large-amplitude unsteady motions with steady forward speed, a validation of the solution with only forward speed was made. The time-domain Green function satisfies the linearized free surface boundary condition in the moving coordinate system as does the steadily translating Havelock source. A radiation condition which excludes upstream waves is usually invoked in the derivation of the translating source Green function by means of Rayleigh virtual viscosity or arguments concerning integration contours in the complex plane (cf. Newman (1977)). In the time-domain method, however, this is not necessary. If the body is started from rest, its motion automatically causes the waves to move downstream. Since the boundary-value problems are the same at large times, one would expect to recover the steady state, or classic Neumann-Kelvin solution from the unsteady time-dependent solution as time goes to infinity. However, it is difficult reach an infinite time limit with a finite computer budget.

In practice one finds that the unsteady time-domain solution oscillates about the steady-state limit at a particular frequency, which depends on the forward speed, and that the oscillations decay slowly in time. For any finite time, some small oscillations remain, although they may be made arbitrarily small by using a very smooth start.

Figures 4.4 and 4.5 show an example of calculations for a submerged ellipsoid. The nondimensional drag, lift and moment are shown as functions of nondimensional time. The ellipsoid has an aspect ratio of $L/D = 5$, and is submerged a depth $H = 0.16L$ at its center. The body is started from rest and reaches an ultimate Froude number $F_n \equiv U_0/\sqrt{gL} = 0.35$. A smooth start is used so that the velocity is

$$U(t) = U_0\left(1 - e^{-at^2}\right) \tag{4.1}$$

Note that this motion has zero initial velocity and acceleration, but contains a jerk

at $t = 0$. In this case the value of the constant 'a' was 0.02.

The unsteady time-domain results oscillate about a mean value, and the amplitude of oscillations decay approximately as $1/t$, with a frequency such that the the value of $\tau \equiv U_0\omega_e/g$ is 1/4. These results are in complete agreement with Wehausen (1964) who investigated the effects of the starting transient on the wave resistance of a thin ship started abruptly from rest. These figures show that even a smooth starting transient leads to some oscillations. The more abrupt the start, the bigger the oscillations. Such effects are often seen in towing tanks, although the oscillations appear to die out after some time.

The results shown are extrapolated from four values of the nondimensional time step: $\Delta t' = \Delta t\sqrt{g/L} = 0.25, 0.2, 0.125$, and 0.0625. The results are shown for three discretizations: 36 panels (12 lengthwise by 3 girthwise), 64 panels (16 by 4) and 100 panels (20 by 5) on half of the body. These are the same geometric discretizations used by Doctors and Beck (1987). For each paneling, Richardson extrapolation, Doctors and Beck (1987), is used to obtain a limit for zero time step size. Extrapolation is then further employed to estimate the limit as the number of panels goes to infinity. This method of extrapolation ignores any interaction between the effects of time step and panel size.

Figure 4.6 is a plot of the error in the steady-state surge force (wave resistance) on the same body with the same submergence depth versus time step size for each of the discretizations, and figure 4.7 shows the error versus the number of panels. The errors in figure 4.6 are taken relative to the extrapolated values in time step, and those in figure 4.7 are relative to the extrapolated values in panel number. A log-log scale is used in the figures. The steady-state values were obtained by averaging the last part of the record. The convergence rate with time step is seen to be approximately $O(\Delta t^2)$. The slope of the lines is 2.0 for the extrapolated values, and slightly higher for the 36, 64 and 100 panel discretizations. Figure 4.7 indicates that the convergence

rate with panel number is approximately linear for this smooth, submerged body. The slopes of the lines are approximately 0.99 for all the time step sizes. This study would need to be extended to other Froude numbers and to surface-piercing bodies before complete convergence information was available.

The final extrapolated value of the nondimensional wave resistance, defined as $C_W = R/(\rho g \nabla)$, (where R is the resistance, ρ is the fluid density, g is the gravitational acceleration, and ∇ is the volume of the body) is $C_W = 0.49$ for Froude number $F_n = 0.35$. Farell (1973) performed wave resistance calculations for this body, and obtained a value of $C_W = 0.52$— about 6% higher. Since finer discretizations lead to higher values of the wave resistance in this case, one would expect the time-domain results to improve slightly with respect to Farell's if smaller panels and time steps were used.

The results presented in Doctors and Beck (1987) for this Froude number show much better agreement with Farell's results. This is because the comparisons were made for the calculations using analytic integration of the Green function over panels, (what Doctors called the 'wave panel'). Since the body is at a relatively shallow depth of submergence, the panel integrations are important for this case. Use of a larger number of quadrature points per panel in the time-domain calculations would probably improve the agreement.

Figure 4.8 shows a similar result. In order to save computer time, the coarse discretization of 36 panels is used. As the above figures show, using more panels will alter the absolute value of the forces, but the character of the curves remains the same. For numerical investigations of a submerged body, the 36 panel ellipsoid seems sufficient. As in figure 4.4, several values of time step are used, and the limit is taken for a zero time step using Richardson extrapolation. The ultimate Froude number is 0.35, and the two depth to length ratios are H/L=0.16 (the same as in figures 4.4– 4.7) and 0.245.

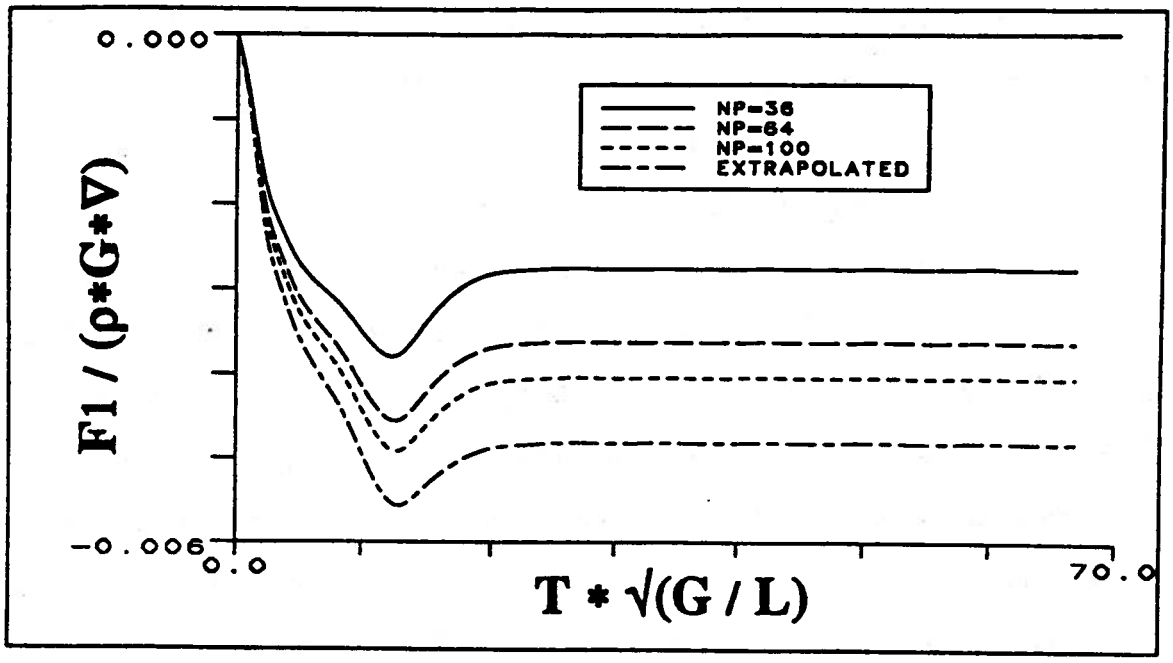

Figure 4.4: Surge force on a submerged ellipsoid started from rest using three discretizations, ultimate Froude number Fn=0.35, depth $H_0/L = 0.16$

As can be seen, the time-domain results quickly approach the steady-state values. The large-time values for both heave and surge agree with the steady Neumann-Kelvin results to within 0.5% even for the smaller depth of submergence. This is a good verification for two entirely different computer codes. Both the Neumann-Kelvin and time-domain results were obtained using the monopole approximation as described in Doctors and Beck (1987). Hence, the agreement is quite good.

Figure 4.9 shows a greatly enlarged view of the approach to steady state for the surge and heave forces at the deeper depth of submergence. The surge force is expanded 125 times and the heave force 400 times. On this scale, the decaying oscillations are clearly visible. The steady-state results are also shown for comparison.

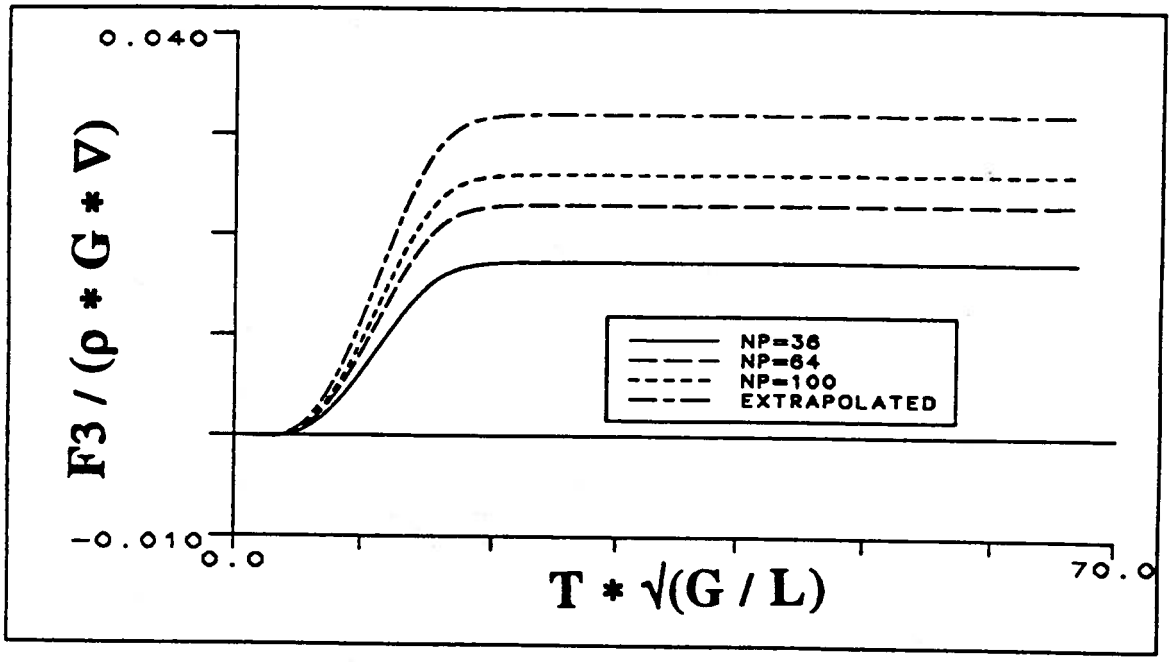

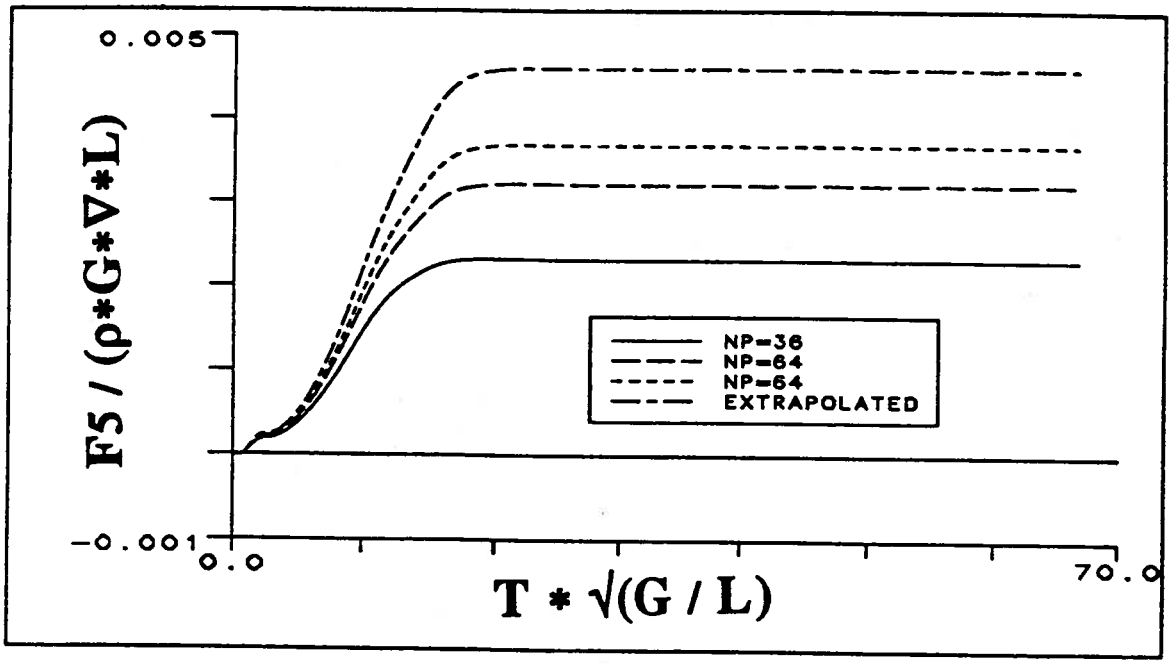

Figure 4.5: Heave force and pitch moment on a submerged ellipsoid started from rest using three discretizations

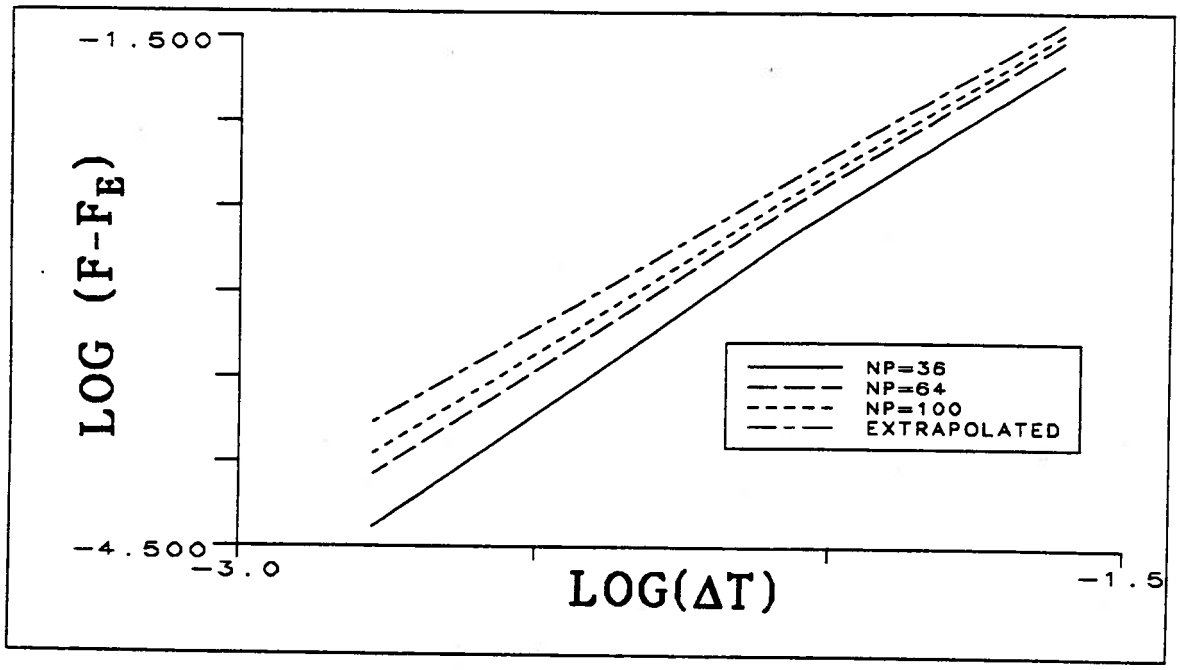

Figure 4.6: Convergence of the steady state surge force (wave resistance) on a submerged ellipsoid versus time step size

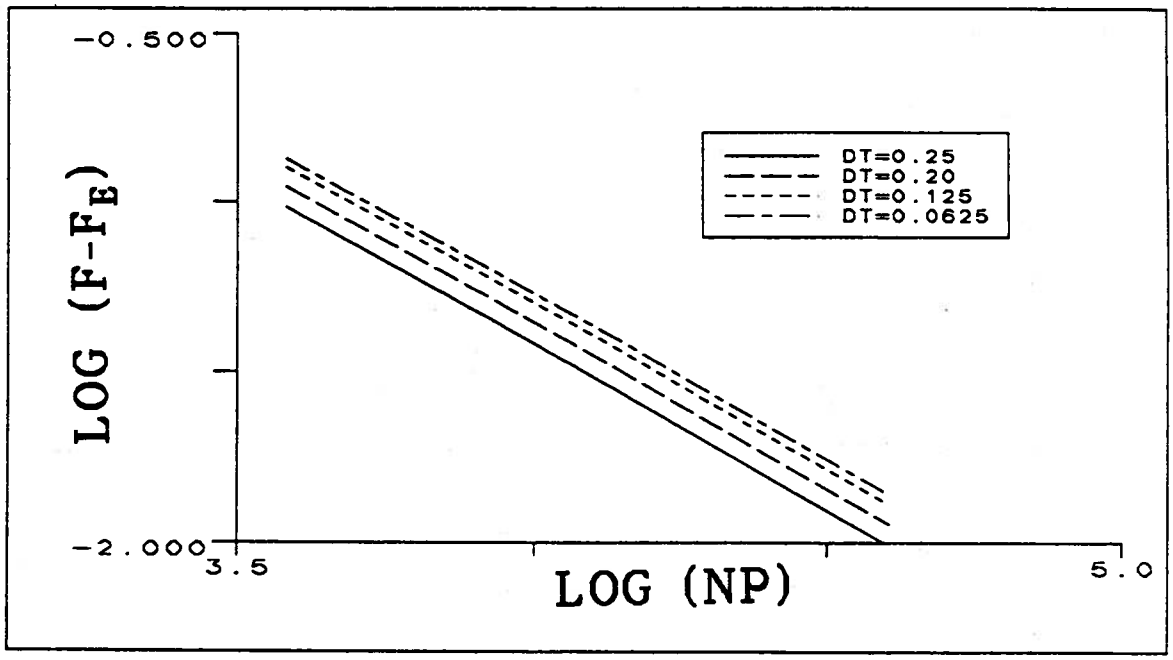

Figure 4.7: Convergence of the steady state surge force (wave resistance) on a submerged ellipsoid versus number of panels

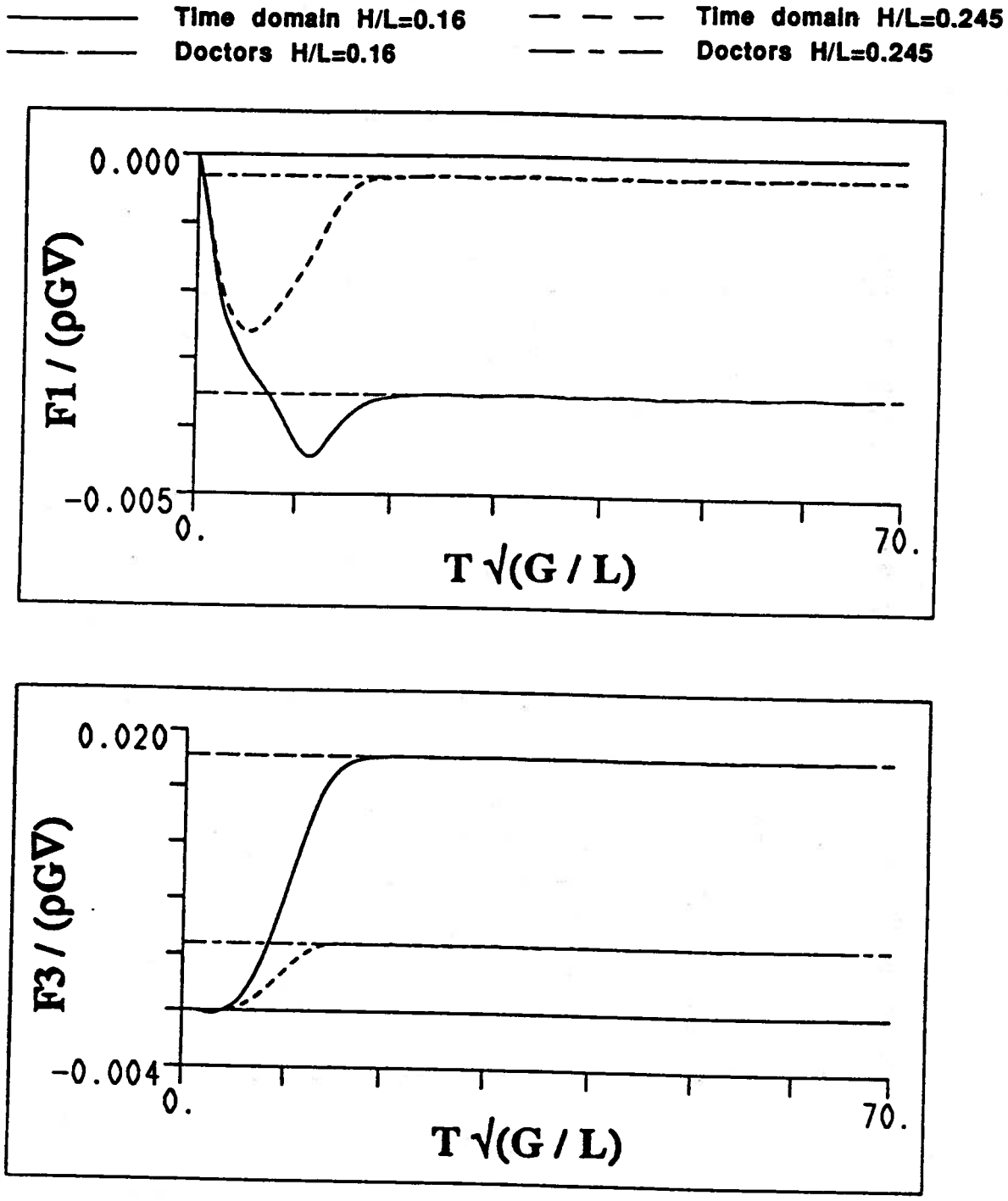

Figure 4.8: Surge and heave force on a submerged ellipsoid started from rest at two different depths (36 panels), ultimate Froude number Fn=0.35

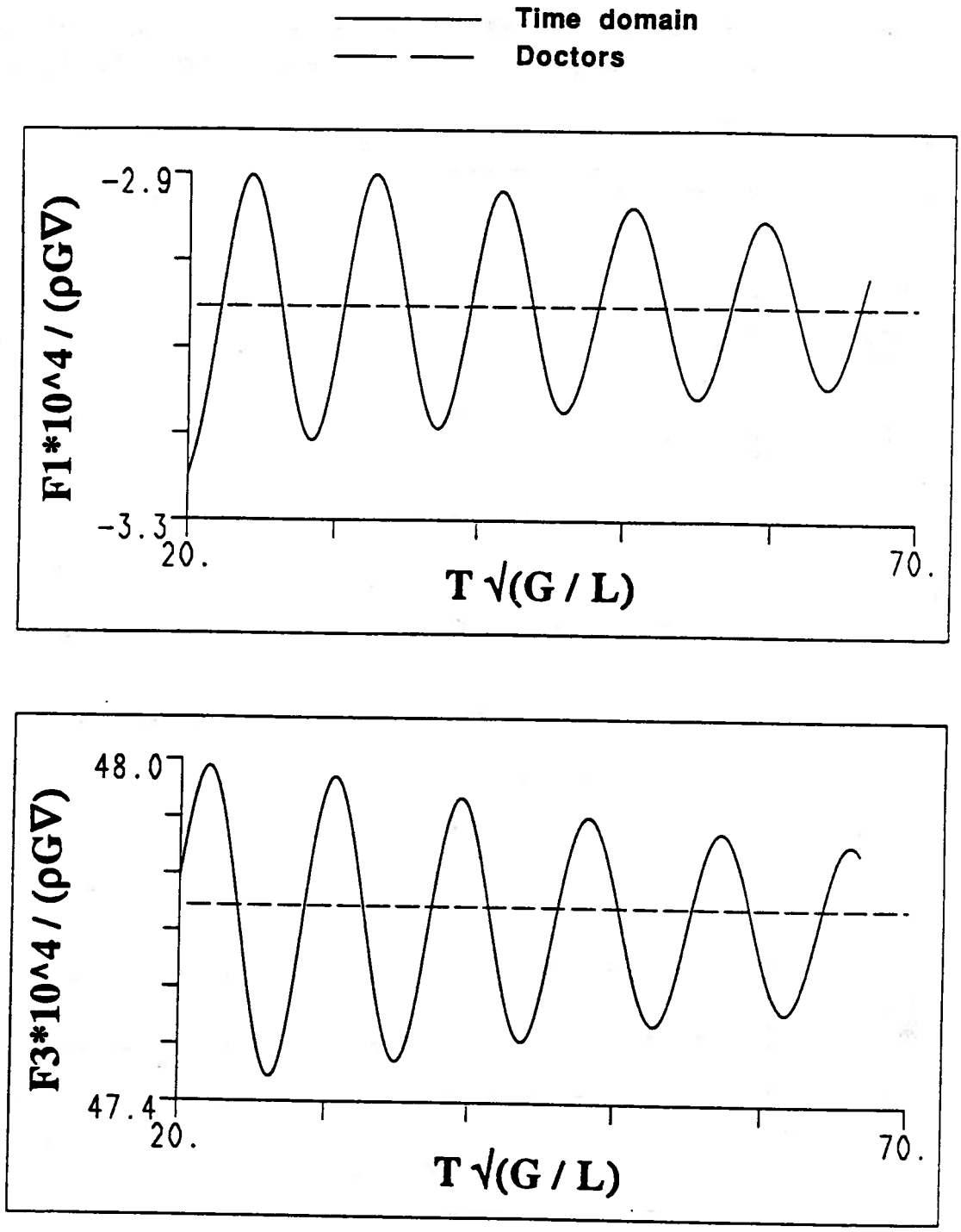

Figure 4.9: Greatly expanded view of the approach to steady state for H/L=0.245 (36 panels)

4.3 A Heaving Ellipsoid with Forward Speed

Examples of body-exact calculations are shown in figures 4.10– 4.15. The results are all for a submerged ellipsoid of length-to-diameter ratio of 5. The body has a forward speed as in the calculations above, and in addition has a sinusoidal heave motion imposed. The time history of the forced heave motion is given by:

$$\dot{\zeta}_3 = \left(1 - e^{-at^2}\right) \sum_{j=1}^{N} A_j sin\left(\omega_j t\right) \tag{4.2}$$

To investigate the effects of $\tau = 1/4$ on simulations of sinusoidal motions, figure 4.10 shows the heave force on the ellipsoid as a function of time. The body has forward speed (ultimate Fn=0.35) and is also heaving sinusoidally at a single frequency corresponding to $\tau = 1/4$. The amplitude of motion is $A/L = 0.085$ and the mean depth of submergence is $H_0/L = 0.245$. In figure 4.10, the total heave force with and without artificial damping and the contribution to the force from just the $(1/r - 1/r')$ terms is shown. The inclusion of artificial damping in the large-time tail of the Green function for a simple source are discussed in Chapter 3. The curves for the total force with and without artificial damping are almost coincident. The $(1/r - 1/r')$ terms do not vary from cycle to cycle and are responsible for a large part of the force, particularly on the bottom of the stroke. As expected, the wave terms make the biggest contribution near the free surface.

The difference between the total force and the $(1/r - 1/r')$ component is shown in figure 4.11. As can be seen, the peaks in the force curves are growing slowly for no artificial damping and reach constant amplitude for the case with damping. A line is drawn through the peaks of the curves to emphasize the growth without artificial damping. Since there is a singularity in the frequency domain response at $\tau = 1/4$, it is expected that the results without artificial damping will continue to grow and there will be no steady state solution. The artificial damping apparently eliminates this growth. The growth rate for the case without artificial damping is extremely

slow. Dagan and Miloh (1980) show that in three-dimensions the singularity in the frequency domain behaves in the vicinity of $\tau = 1/4$ as $\log|\omega - \omega_c|$, where ω_c is the $\tau = 1/4$ critical frequency. While the asymptotic form of the growth in the time-domain is not yet known analytically, it is probably on the order of $\log(t)$ as $t \to \infty$.

Figure 4.12 presents the surge force for the $\tau = 0.20$ case with the same parameters as used for figure 4.10, except that in one case (top figure) the frequency was lowered, and in the other (bottom figure), the forward speed was increased such that both solutions correspond to the same τ value. No artificial damping was used in the computation. Several interesting features of this figure should be noted. First, as opposed to the $\tau = 1/4$ case, the peaks in the unsteady force do not grow. There is an initial starting transient and then the peaks exhibit a small oscillatory behavior as they approach steady state. For other combinations of frequency and forward speed the oscillatory behavior can be much more pronounced. It is easily calculated that this oscillation occurs at the beat frequency between $\tau = 1/4$ and $\tau = 0.20$. The starting transient must induce some $\tau = 1/4$ response and this forms a beat with the $\tau = 0.20$ force. Also shown in the figure is the approach to steady forward speed if there is no forced heave (a replot of the curve in figure 4.8 as long dashes at small times) and the mean of the total surge force near the end of the record (small dashes at large times). The vertical difference between these two lines is the mean added drag due to heave. This demonstrates an advantage of the body-exact time-domain method: the mean shift and slowly varying forces are automatically computed, no special calculations are necessary.

The effects of $\tau = 1/4$ on more general simulations are shown in figures 4.13 and 4.14. The 'random' motions simulations were made using a sum of five sine waves in heave as in (4.2) with forward speed. Figure 4.13 has one component placed at $\tau = 1/4$ and in 4.14 this component has been eliminated. Each of the simulations were run with and without the artificial damping. The dashed line near the axis

is the difference between the two runs. Without the $\tau = 1/4$ component (figure 4.13) the difference is so small it cannot be seen in the figure. For the $\tau = 1/4$ case, the difference continues to grow. Initially, the difference is exactly zero because the artificial damping affects only the large time asymptotic form of the time-domain Green function. A greatly expanded view of the differences is shown in figure 4.15. As can be seen, there are some differences between the artificially damped and undamped calculations even for the case without the $\tau = 1/4$ component; however, they remain very small. With the $\tau = 1/4$ component present, the differences are much larger and more importantly, they continue to grow. It appears that any long-time simulation which uses the linear free surface boundary condition and includes $\tau = 1/4$ forcing will fail because this component will eventually dominate the solution. The proposed artificial damping fix-up is simple but effective. Undoubtedly, improved methods can be developed.

However, the effects on a simulation created by solving the equations of motion have not been investigated. If the input to the system were waves at the $\tau = 1/4$ frequency, and the ship were free to surge, one might not expect an increasing response as time increases. More likely, the forward speed would change, altering some of the parameters such as frequency and the τ value and diminishing the effects of the singularity.

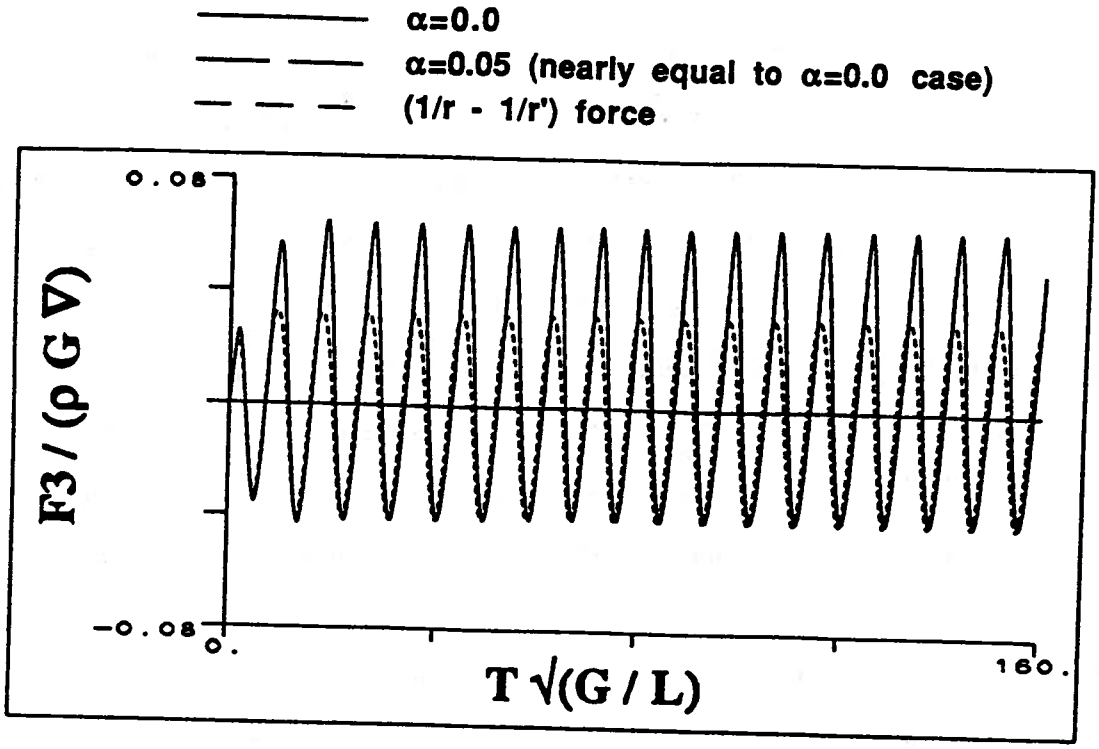

Figure 4.10: Vertical force on a heaving ellipsoid at Fn=0.35, $\tau = 1/4$, amplitude $A/L = 0.085$, mean depth $H_0/L = 0.245$

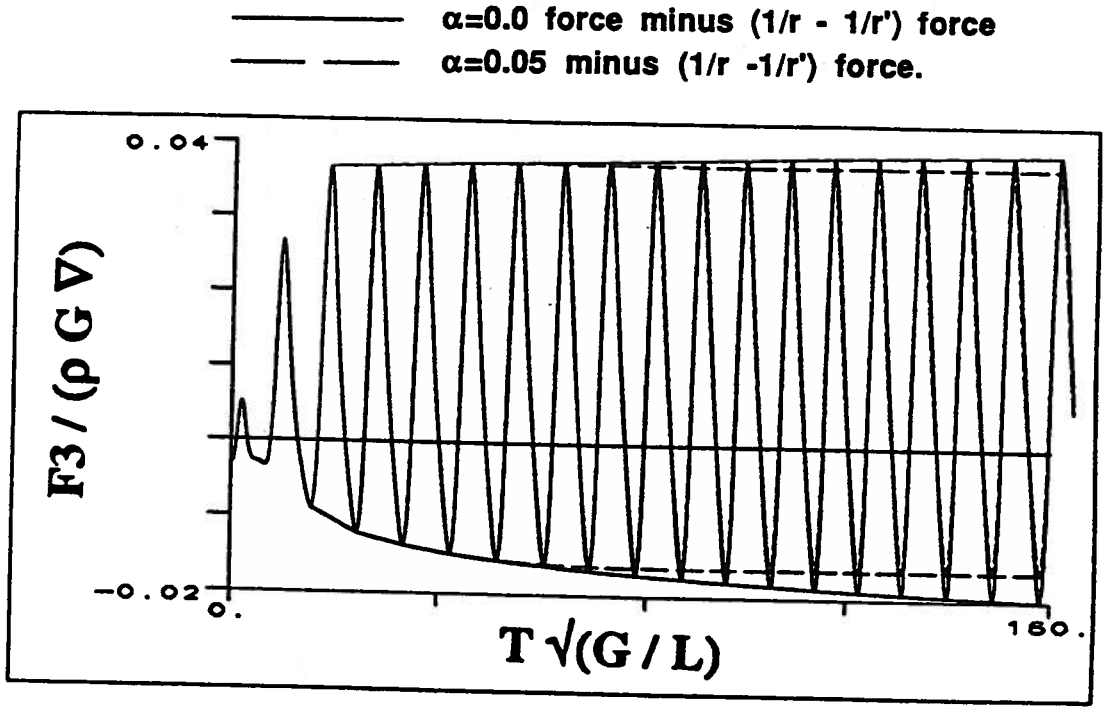

Figure 4.11: Expanded view of the total force minus the $\phi = 0$ force

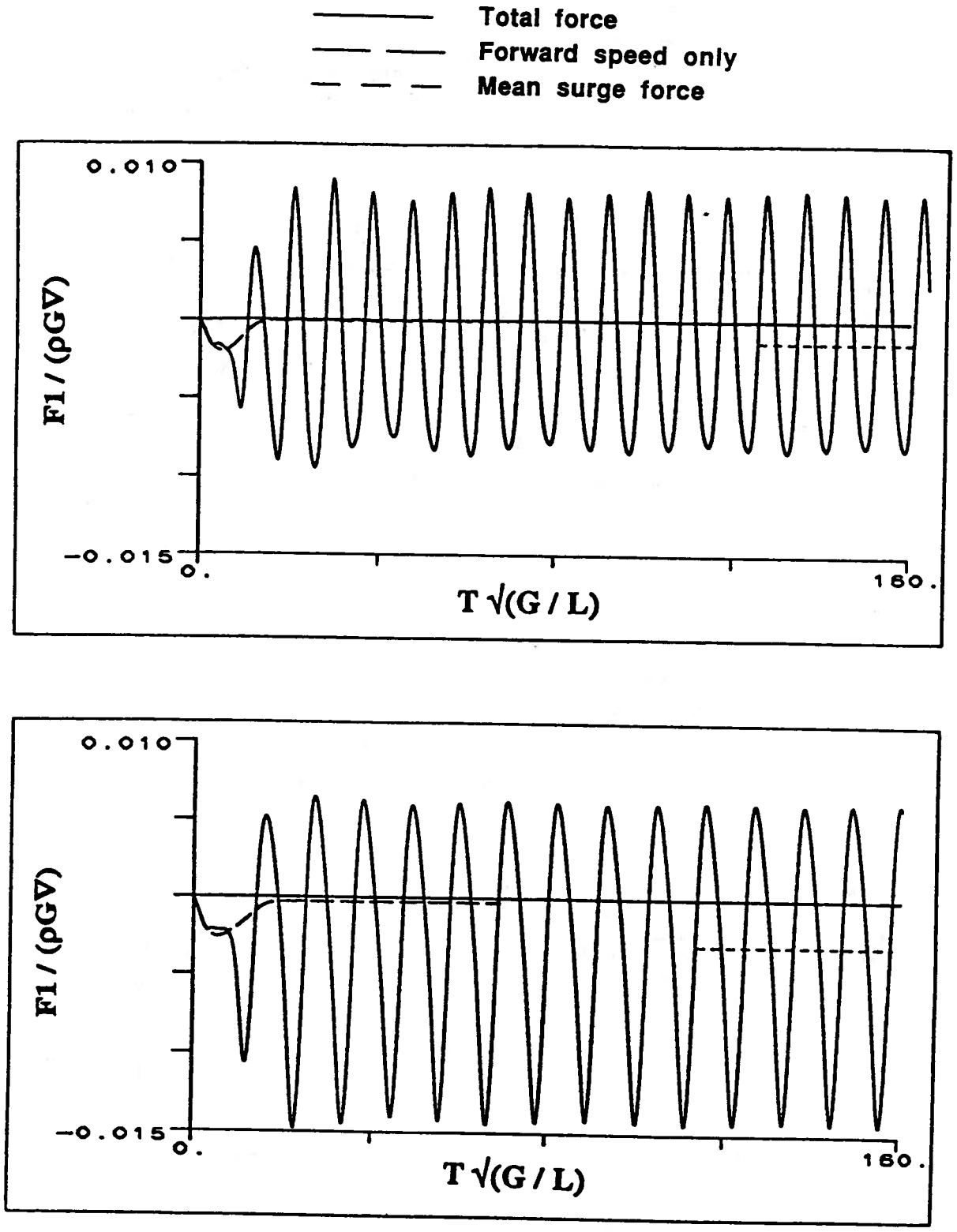

Figure 4.12: Surge force on a heaving ellipsoid at $\tau = .2$, $A/L = .085$, $H_0/L = .245$

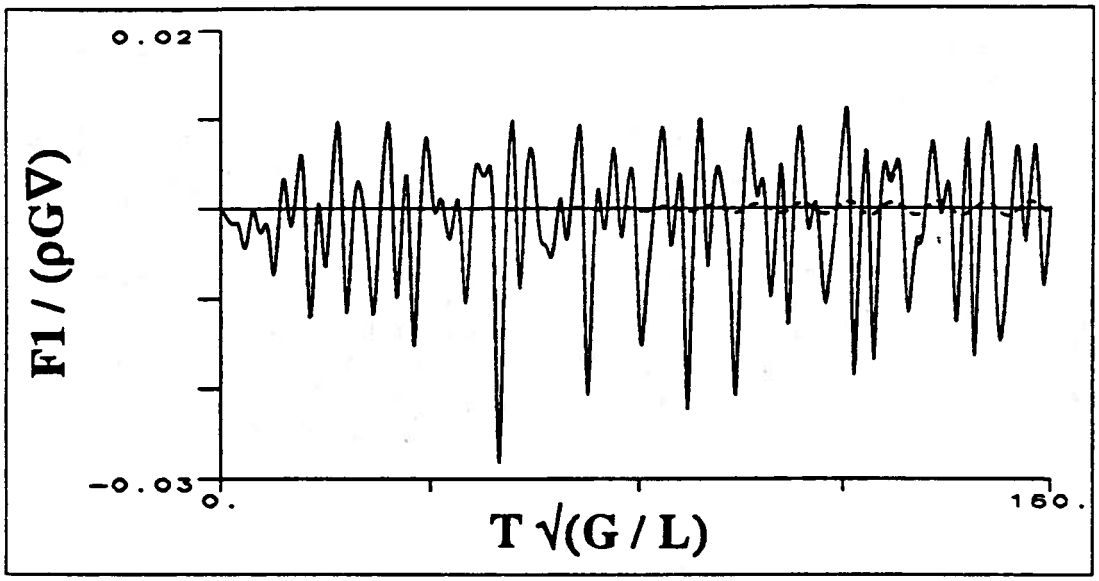

Figure 4.13: Surge force on a heaving ellipsoid at Fn=0.35, with a sum of five sine waves in heave

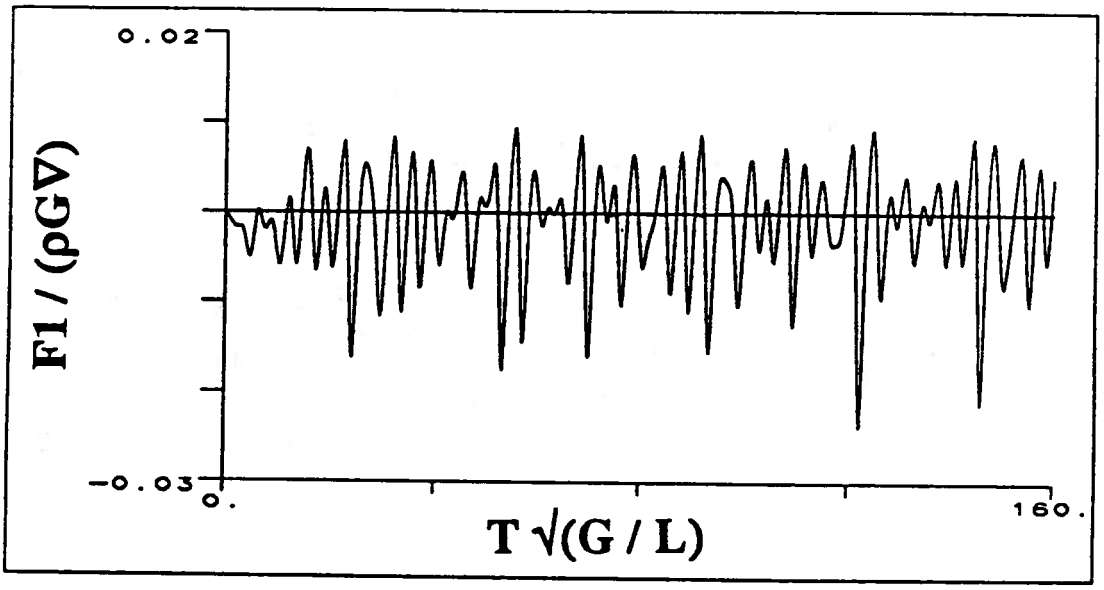

Figure 4.14: Surge force on a heaving ellipsoid at Fn=0.35, with a sum of four sine waves in heave

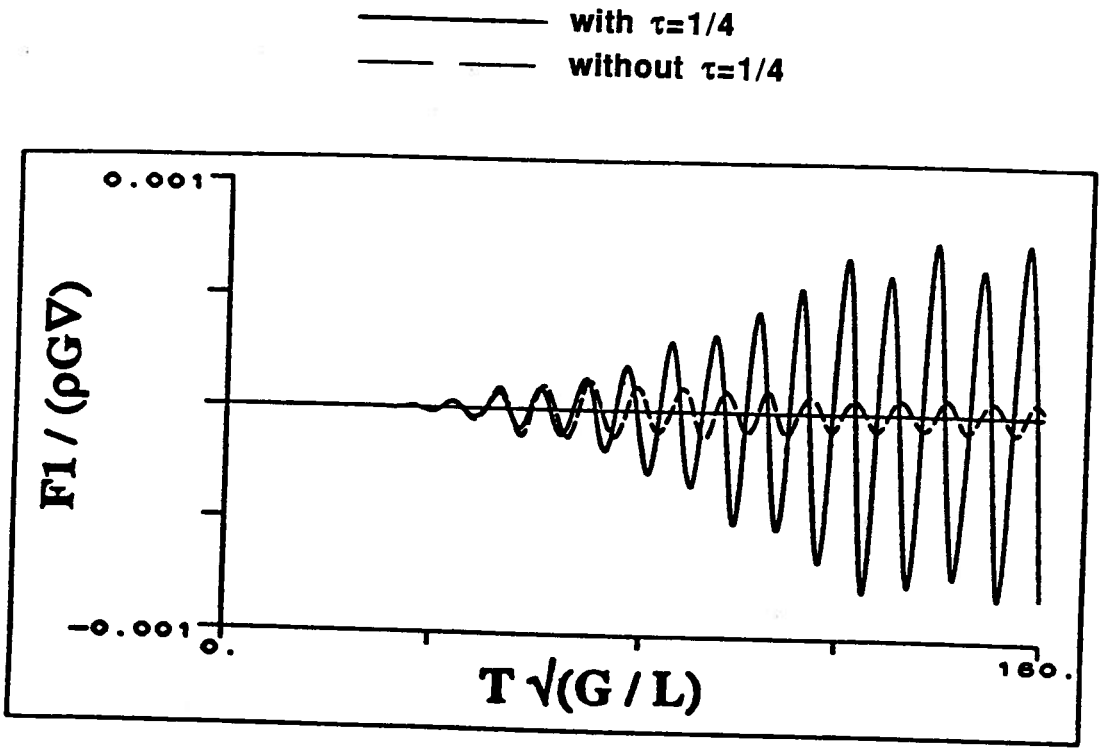

Figure 4.15: Greatly expanded view of the difference forces from the above figures

CHAPTER V

NUMERICAL RESULTS FOR THE LINEAR PROBLEM

5.1 Calculations For Wall-Sided Bodies

Examples of computed results using linear time-domain analysis are shown in figures 5.1 through 5.6. These figures show the nondimensional heave and pitch added mass and damping as a function of nondimensional frequency for a modified Wigley mathematical hull form. The Wigley form has a length-to-beam ratio of 10 and a beam-to-draft ratio 1.6. It is vertically tangent at the waterline. The half beam is given by the equation:

$$\begin{aligned} \frac{y}{b} &= \left(1-\left(\frac{z}{T}\right)^2\right)\left(1-\left(\frac{2x}{L}\right)^2\right)\left(1+0.2\left(\frac{2x}{L}\right)^2\right) \\ &+ \left(\frac{z}{T}\right)^2\left(1-\left(\frac{z}{T}\right)^8\right)\left(1-\left(\frac{2x}{L}\right)^2\right)^4 \end{aligned} \tag{5.1}$$

where,

b = the half beam

L = the length

T = the draft

For the calculations, 240 panels (30 lengthwise by 8 girthwise) were used on the half-body. The non-dimensional time step, defined as $\Delta t' = \Delta t\sqrt{g/L}$, was 0.088 and

the total number of time steps was 256. Figure 5.1 and 5.2 present results for zero forward speed and figure 5.3 through 5.6 are for a Froude number of 0.3. Also shown in the figure are strip theory results computed using a Salvesen, Tuck, Faltinsen (1970) based strip theory (cf. Beck (1989)). The experimental results are due to Gerritsma (1988). No experimental results are available for $Fn = 0$.

The Wigley hull is fore-and-aft symmetric. Consequently, for $Fn = 0.0$ the cross coupling coefficients are zero. As can be seen in figures 5.1 and 5.2, the strip theory and time-domain results agree very well for high frequencies. For low frequencies, however, there are significant differences. This is presumably due to three-dimensional effects that are neglected in strip theory. The oscillations in the damping coefficients in the frequency range $\omega' = 6. - 8.$ are a result of irregular frequencies. Inglis and Price (1981a) used a box barge with the same dimensions as the ship to estimate the irregular frequencies. By this method, the first irregular frequency occurs at 5.7 and the second at 7.9. The singular nature of the coefficients around the irregular frequencies is not properly captured because the record length and time step size are insufficient to give adequate resolution to the Fourier transform. This is both a weakness and strength of the time-domain method. As with the $\tau = 1/4$ singularity, in the time domain the irregular frequencies appear as oscillations in the large-time tail and do not cause any particular problems until the Fourier transform is taken. Because of the finite record length and time-step size, the irregular frequencies are effectively filtered out. On the other hand, in the frequency domain the results are singular and calculations in the region of the irregular frequency are meaningless.

Figures 5.3 through 5.6 present the heave and pitch radiation force coefficients at forward speed. It should be noted that the added mass coefficients include the c_{jk}/ω^2 term as discussed in Section 2.4. This is consistent with strip theory (cf. Beck (1989)) and Gerritsma's (1988) experimental results since only the hydrostatic

coefficients were used in reducing the measured data to obtain the added mass and damping coefficients. In figure 5.6, the short-dashed curve shows the pitch added mass neglecting the contribution of c_{55}. In this case, the added mass is actually negative, indicating that the c_{55} term's contribution is quite important. The solid line was computed using the double body m-terms and the long dash curve results from using the simplified version of the m-terms (2.25). For this smooth slender body the different m-terms do not change the results very much.

The most prominent feature of these figures is the singularity at $\tau = 1/4$. The strip theory results are not affected by $\tau = 1/4$ and the experiments were not conducted at such low frequencies. As previously discussed, the $\tau = 1/4$ singularity will affect all linear three-dimensional theories. It has also been shown to affect the body-exact problem in random forced-motion simulations.

For forward speed the agreement between theory and experiment is mixed. For pure heave, the strip theory appears better while for the cross-couplings and for pure pitch the three-dimensional time-domain predictions give better agreement. For this ship, using the double body m-terms is probably not worth the extra effort. Perhaps the complete m-terms might improve the agreement for all modes of motion. It should be noted that in the body-exact computations the full m-terms are automatically accounted for. The agreement between strip theory, linear time-domain analysis, and experiments shown in these figures is typical of the results that have been calculated for many different ship types, Magee and Beck (1988a).

As discussed previously, the character of the curves shown in the figures around the irregular frequencies and at $\tau = 1/4$ is the result of the large-time tail in the time domain. This is demonstrated by figure 5.7 which shows an expanded view of the large-time tail of the pitch moment time-domain record for the Wigley hull calculations. At a Froude number of 0.3 the tail is dominated by the $\tau = 1/4$ frequency and at zero forward speed the irregular frequencies appear. Note that the

zero speed tail has been multiplied by 100 in order to plot it on the same curve as the forward speed result. The apparent beat frequency in the zero speed tail is probably the result of interference between the two lowest irregular frequencies. We have seen no evidence of irregular frequencies in calculations at forward speed. This might be numerical because of the dominance of the $\tau = 1/4$ frequency or it might be the result of forward speed effects.

The nondimensional exciting force coefficients in head seas for the Wigley hull at Fn=0.3 are plotted in figures 5.8 and 5.9 against nondimensional wave number. As for the radiation forces, there is not a significant difference between the solutions with the double-body and approximate m-terms. However, these curves indicate the good resolution now attainable with the fast Green function calculations. The spike at $\tau = 1/4$ is visible, although it is not very pronounced.

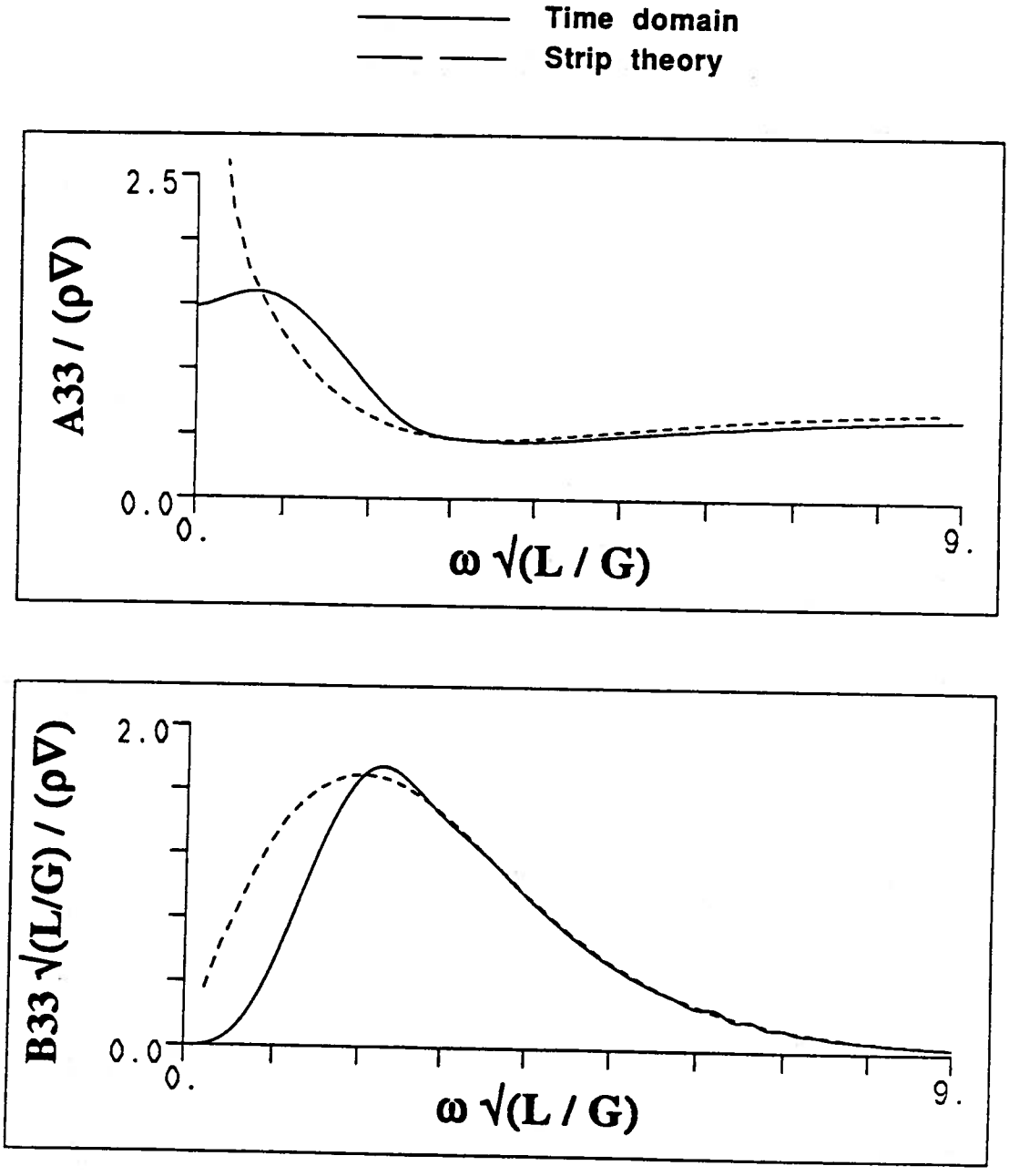

Figure 5.1: Heave added mass and damping for a Wigley hull, Fn=0.0

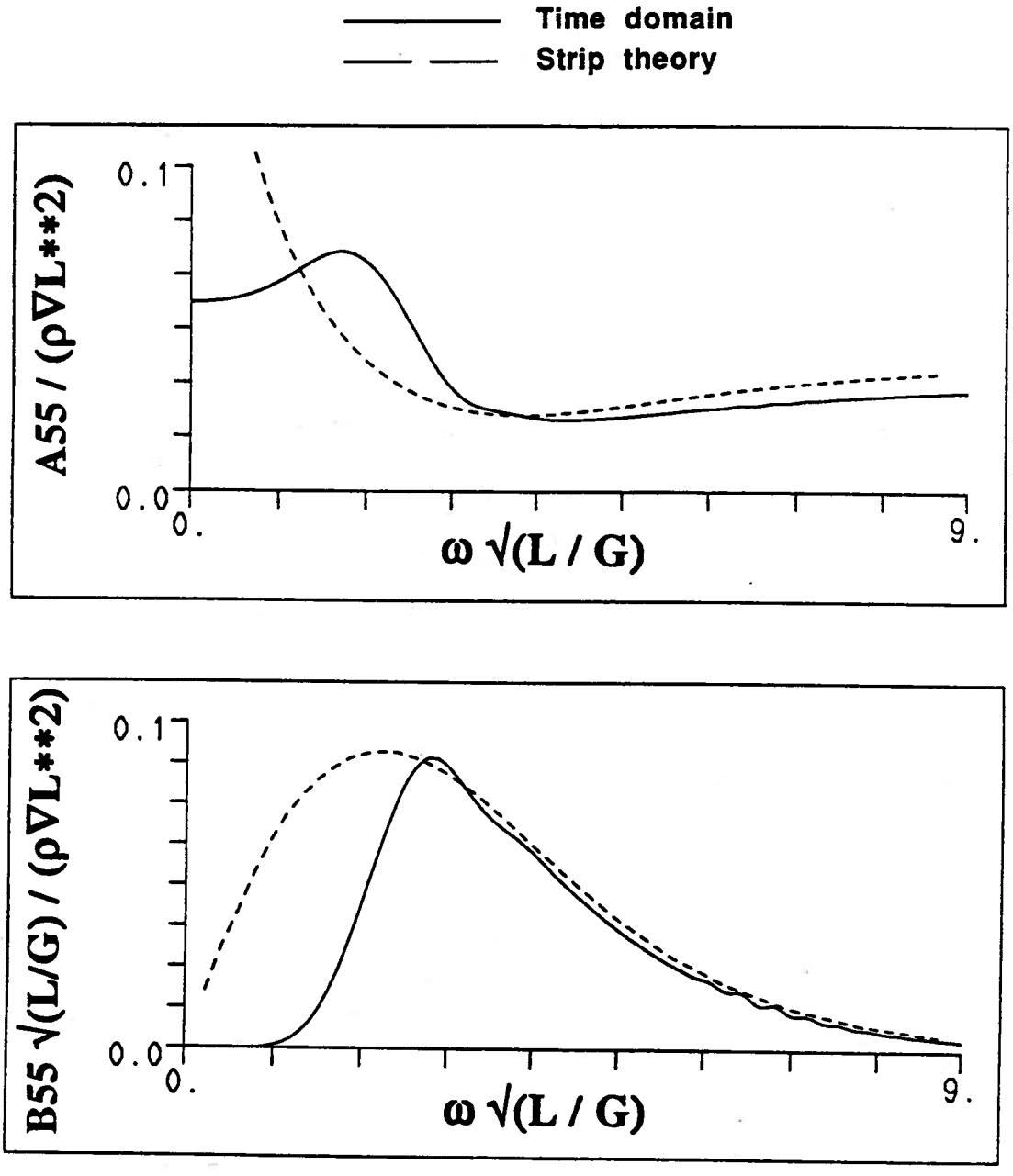

Figure 5.2: Pitch added mass and damping for a Wigley hull, Fn=0.0

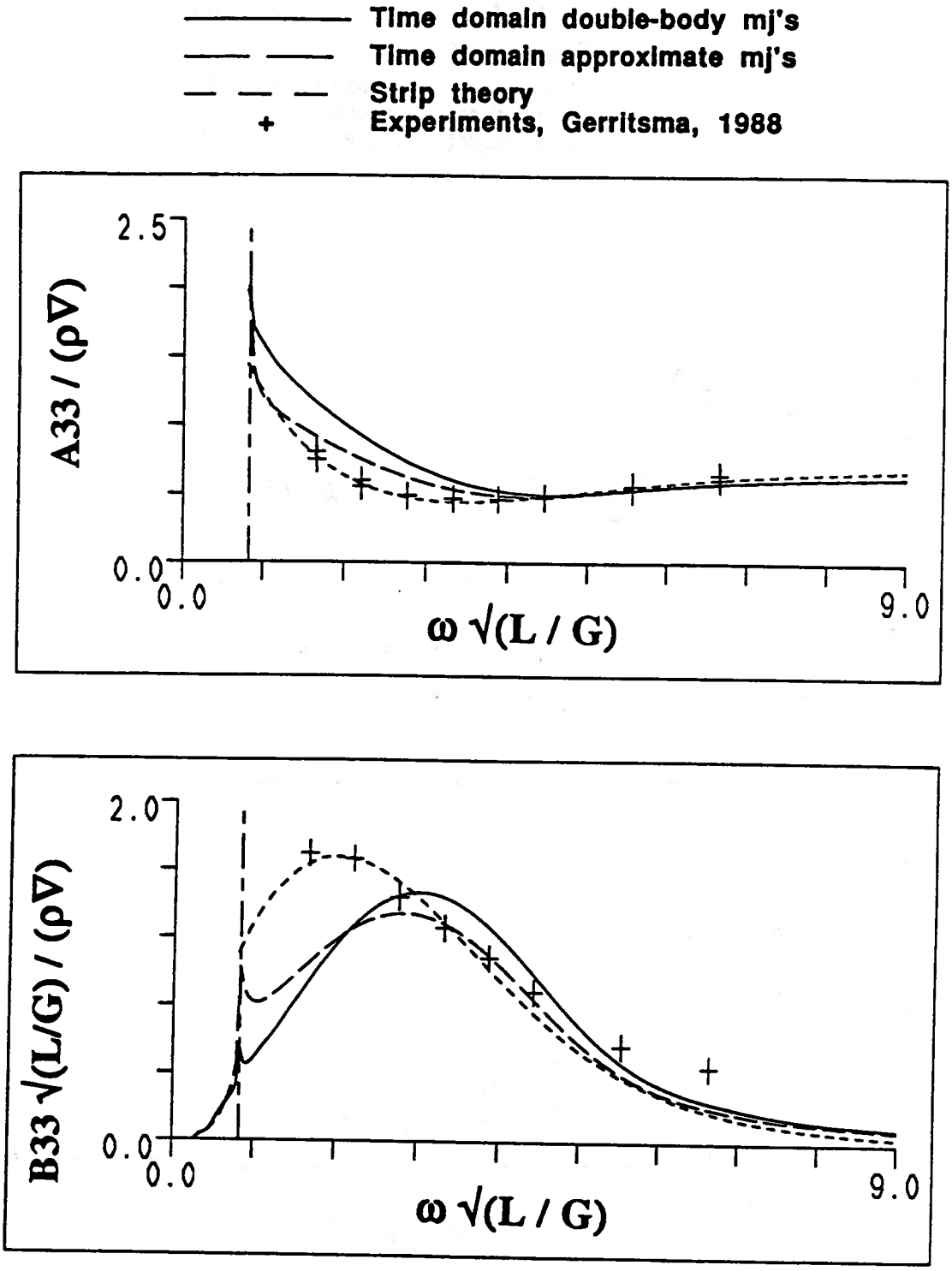

Figure 5.3: Heave added mass and damping for a Wigley hull, Fn=0.3

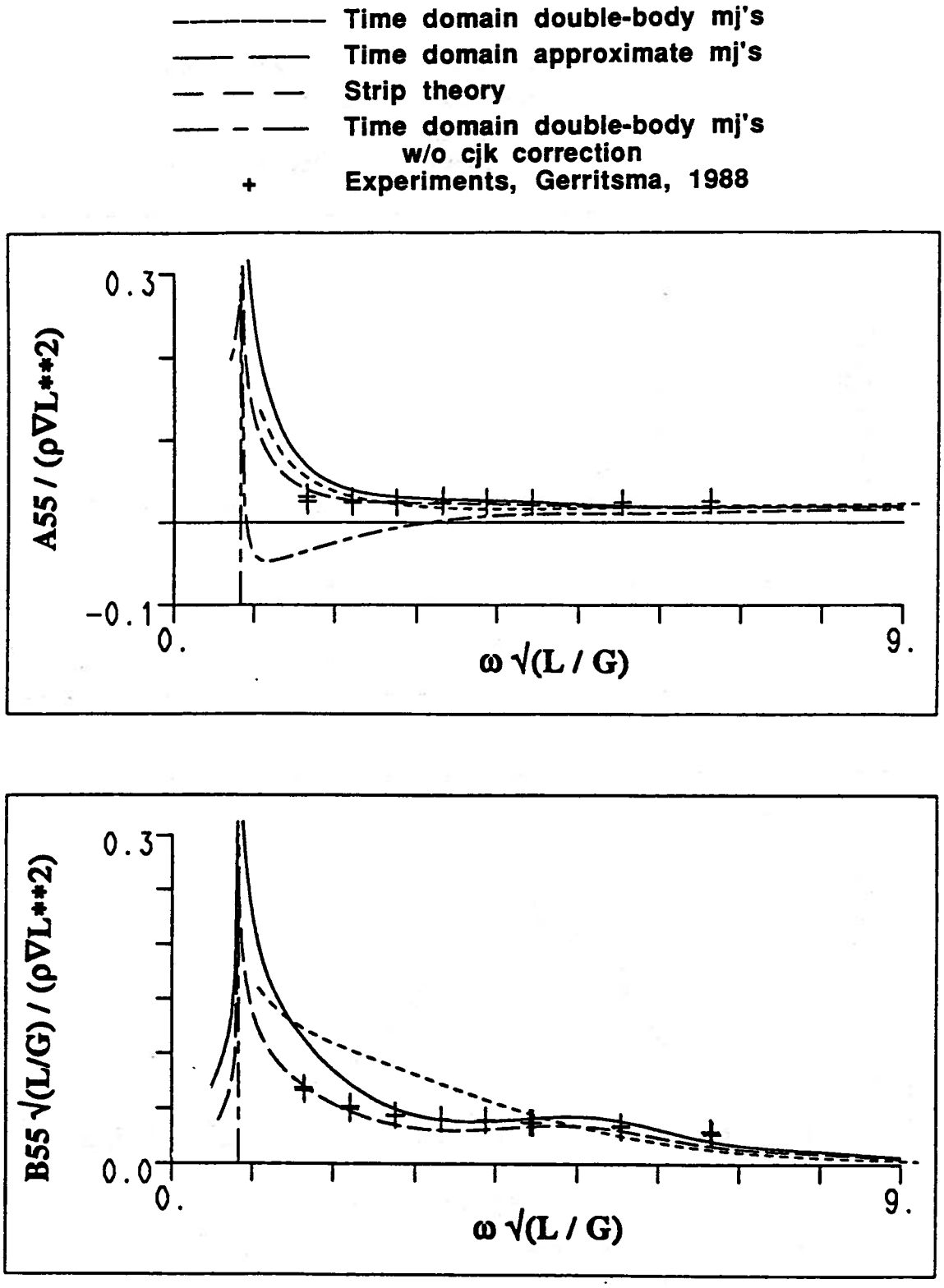

Figure 5.4: Pitch added mass and damping for a Wigley hull, Fn=0.3

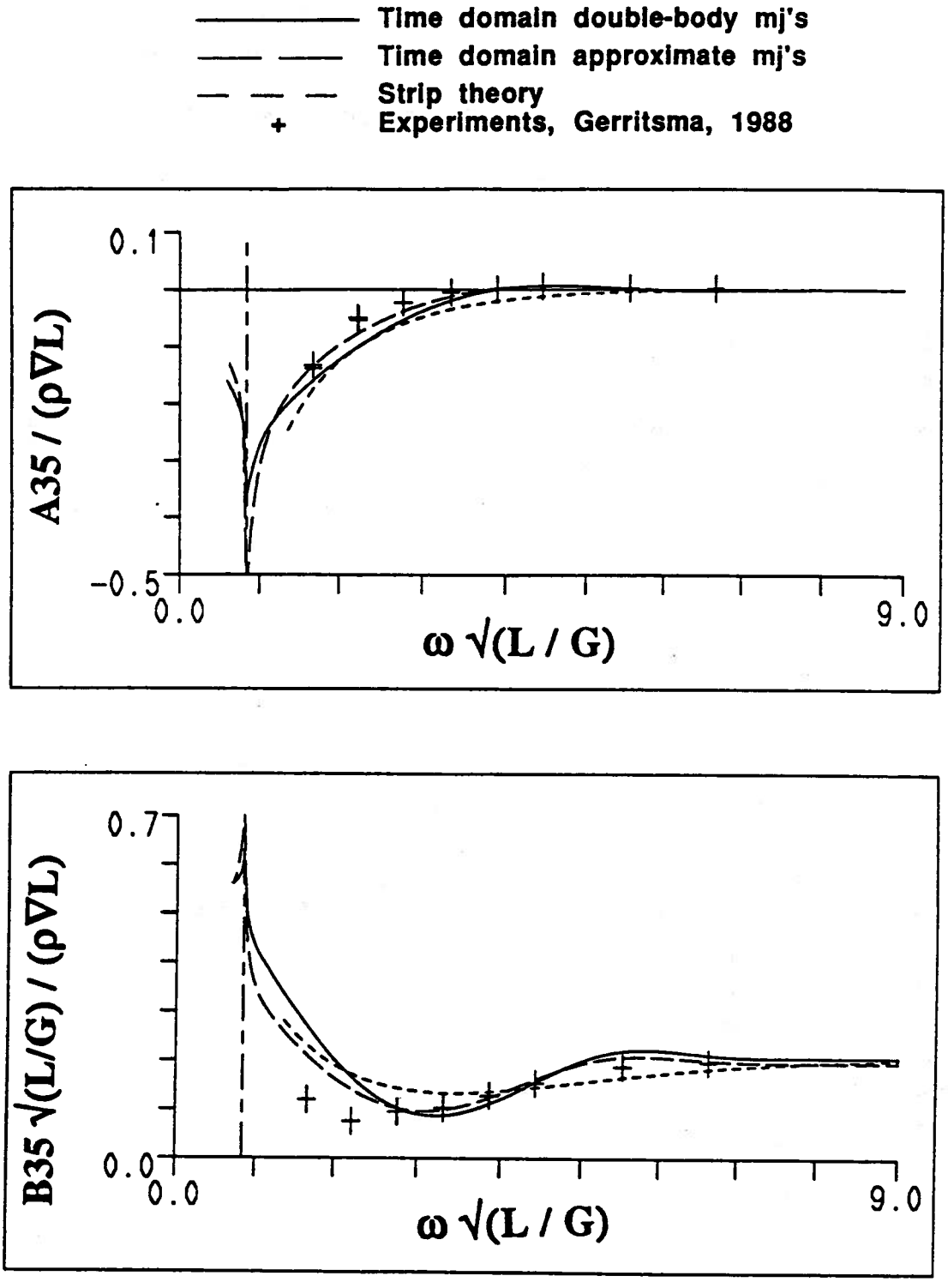

Figure 5.5: Heave-pitch added mass and damping for a Wigley hull, Fn=0.3

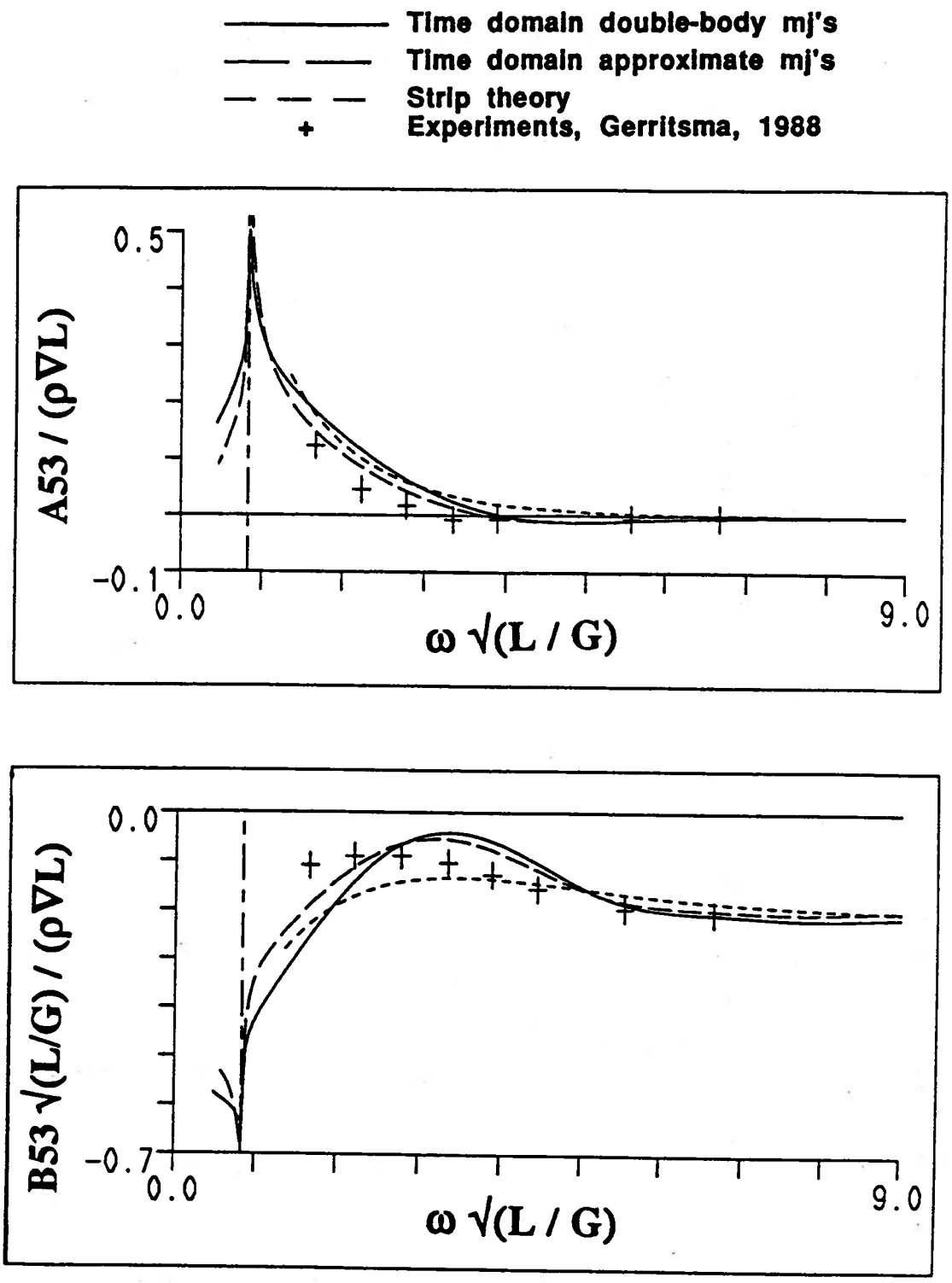

Figure 5.6: Pitch-heave added mass and damping for a Wigley hull, Fn=0.3

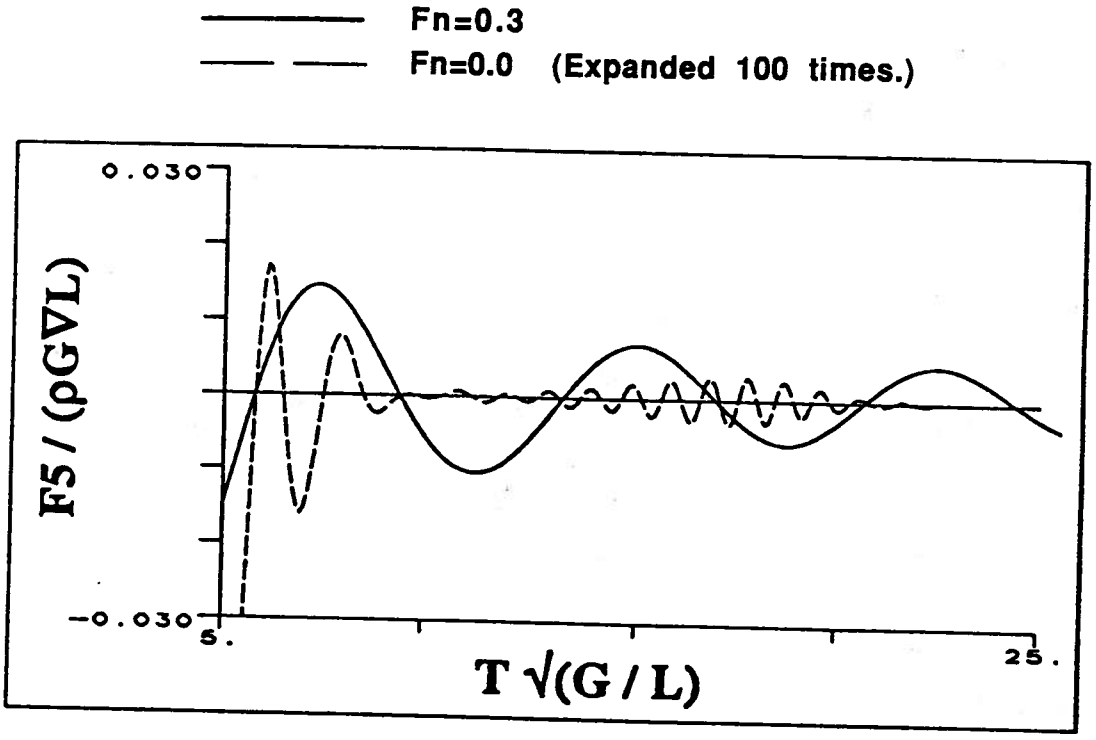

Figure 5.7: Large-time tail of the time-domain record of the pitch moment for the Wigley hull. Fn=0.0 solution has been expanded 100X

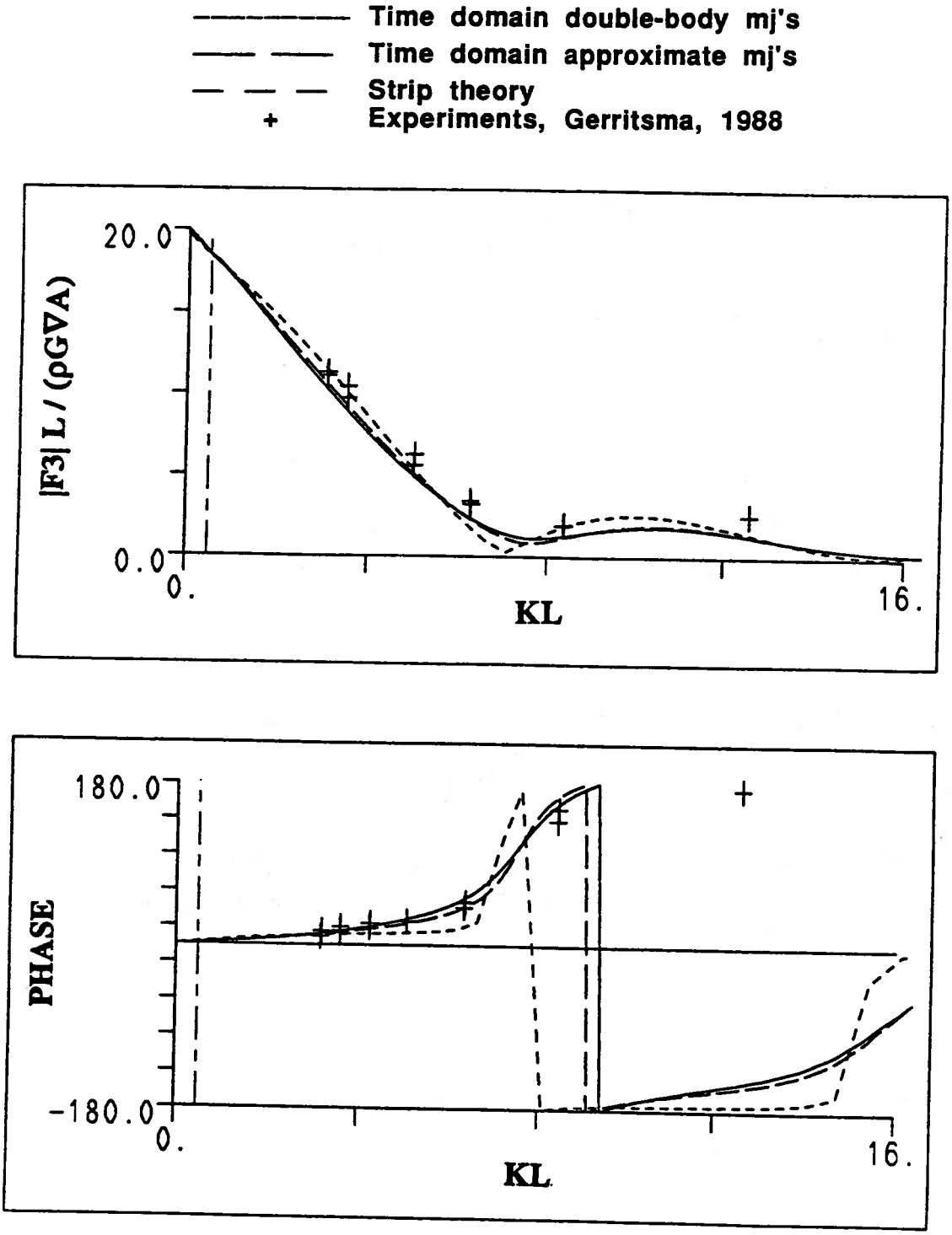

Figure 5.8: Heave exciting force for a Wigley hull in head seas, Fn=0.3

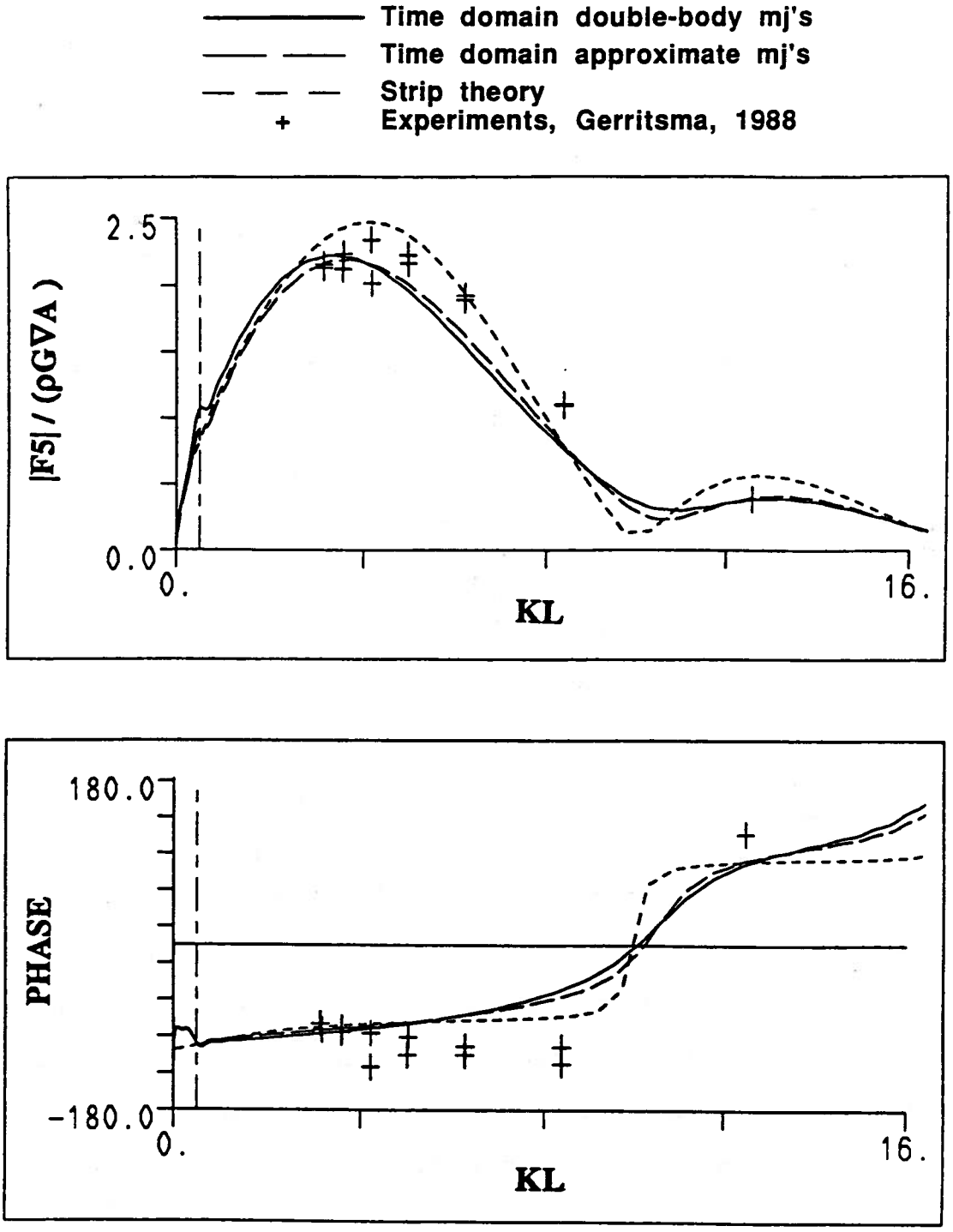

Figure 5.9: Pitch exciting force for a Wigley hull in head seas, Fn=0.3

5.2 Calculations for Nonwall-Sided Bodies

Before proceeding with the solution of the large-amplitude motion of surface-piercing bodies, the linear problem was investigated further. Some difficulties were encountered in the solution for shallow bodies at zero forward speed. In particular, an instability appears in the time-domain solution for bodies with large flare at the waterline. The instability takes the form of an oscillation growing without bound as time increases.

The instability appears first on panels adjacent to the free surface, and because the equation is elliptic, eventually spreads throughout the domain. It does not appear for wall-sided or moderately flared bodies, but increases in severity the shallower and more flared the body. The frequency of the oscillations in the solution appears to be related to the horizontal extent of the panels near the free surface.

An example is shown in figure 5.10 which gives the time record of the function g_{55}, the integral over the body of the pitch potential due to pitch motion (see (2.32)) for the SL-7 container ship at Fn=0. The force on the body at zero forward speed is the time derivative of this function. The half body is discretized by 212 panels, and the nondimensional time step size is $\Delta t' = .04$. A 2 by 2 Gauss quadrature rule was used for integration of the wave terms over panels, and the line integrals are zero at zero forward speed.

The solid line shows the solution obtained with this discretization. The instability is clearly visible as a bell-shaped oscillatory growth at large time. Also shown by the small squares is the solution using 208 panels obtained by removing the four panels in the stern portion of the ship. These panels have a z-normal of nearly 0.9. No instability is visible in the 208 panel solution, and the solution does not appear to have been otherwise affected. Figure 5.11 shows the paneling for the SL-7 using 212 and 208 panels.

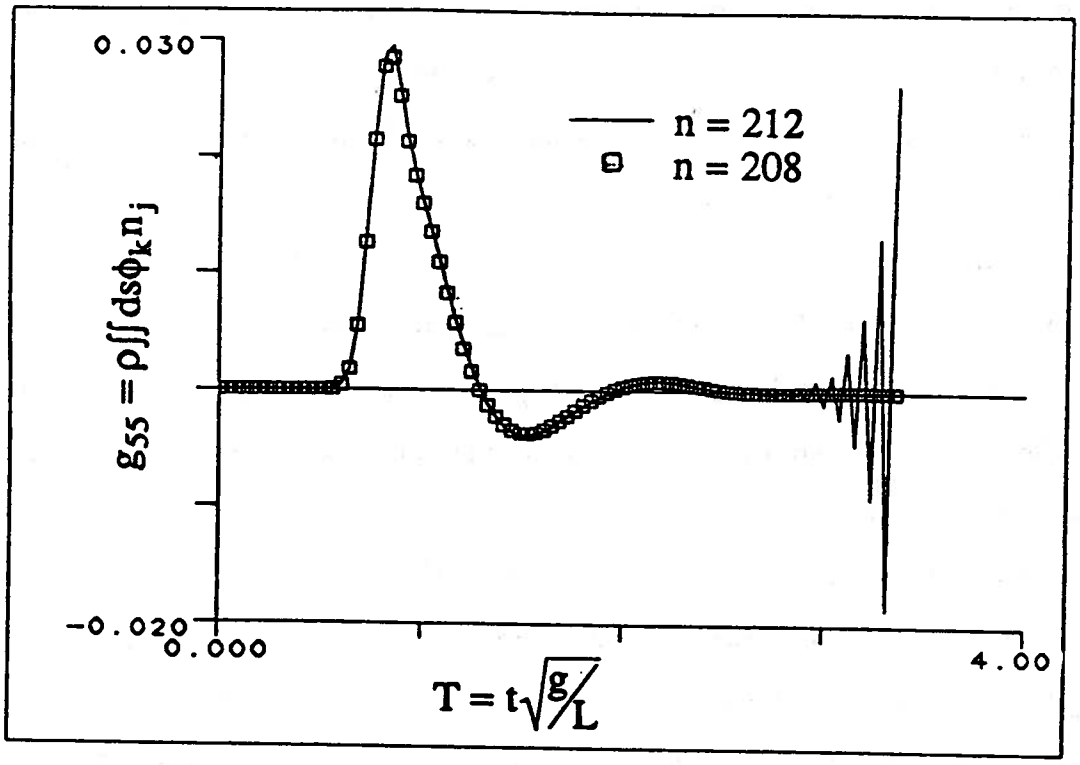

Figure 5.10: Time-domain record (g_{55}) for the SL-7 container ship using 212 and 208 panels

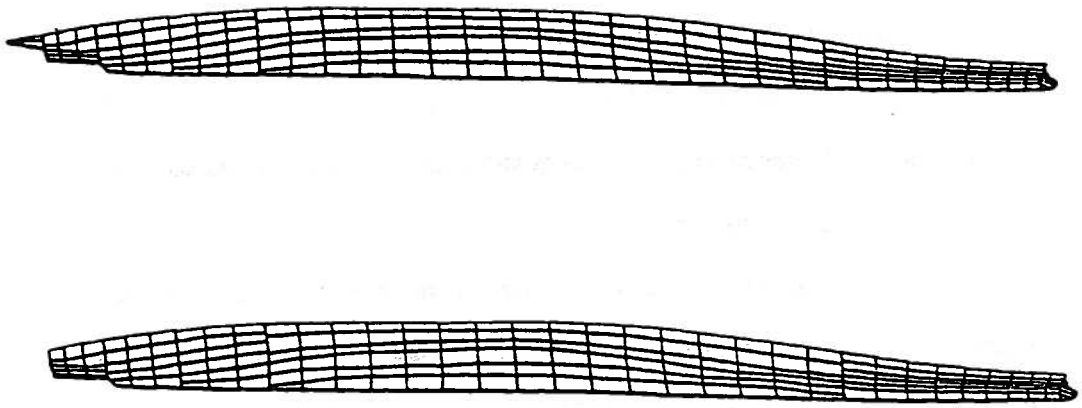

Figure 5.11: Paneling for the SL-7 containership: 212 and 208 panels

In order to study the problem further, without undue complications, a simpler model was proposed whose solution exhibited similar characteristics. A single horizontal flat square panel was run at various depths of submergence to study the parameters affecting the solution.

Figure 5.12 shows the time domain Green function, and figure 5.13 its normal derivative, $\partial\tilde{G}/\partial n(=\partial\tilde{G}/\partial z)$ integrated over the panel. The panel is square with $\Delta x = \Delta y = 0.1$, and is submerged at a depth $z = -0.023$ (slightly less than one fourth the length of its sides). The field point is at the panel center, and the panel has zero forward speed.

The Gauss quadrature rule for integration over the panel varies from 1 by 1 up to 8 by 8 as denoted in the figure. The results were computed using up to a 12 by 12 integration rule, but these are not graphically different from the 8 by 8 rule shown. For the highest order rule, the integration has converged to four significant figures.

The solution to (2.17) for the potential function (g_{33}) due to nonimpulsive heave motion using the converged Green function is shown in figure 5.14 for two depths of submergence, $z = -0.023$ and $z = -0.025$. Little difference can be seen until one looks closely at the tail of the response (figure 5.15). Here we see growing oscillations for the smaller depth, but a smooth decay for the deeper depth. Shallower depths of submergence are more unstable. In figure 5.15, three solutions are shown for $z = -0.023$, and one for $z = -0.025$. Different time step sizes and Gauss integration rules are shown for the shallower depth, but the results have all converged to graphical accuracy, and hence appear as one line.

Some insight into the possible cause of the instability can be gained by looking at the frequency-domain representation of the Green function. As shown in Chapter 3, the Fourier transform of the time-domain Green function is the frequency-domain Green function used by, for example, Wu and Eatock-Taylor (1987).

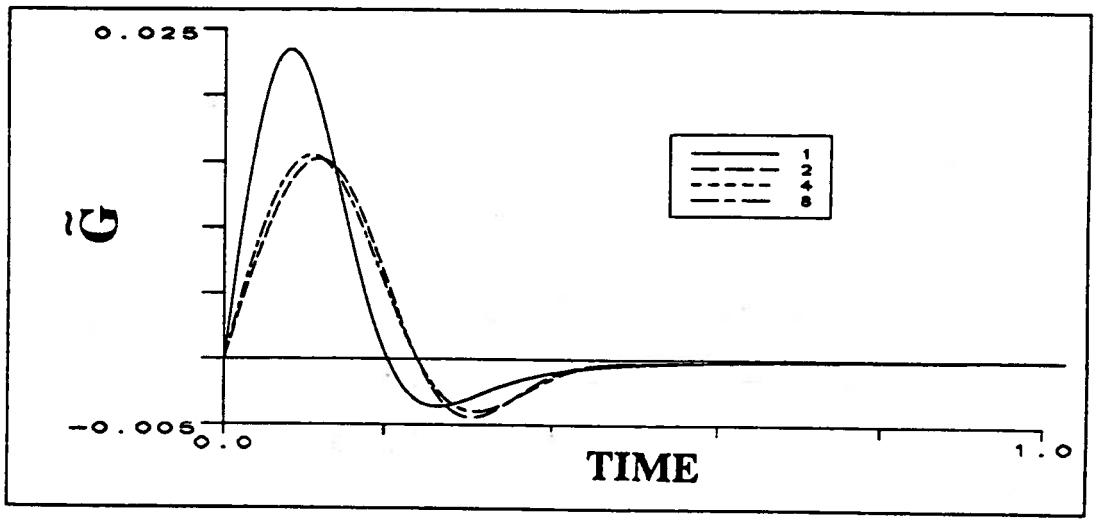

Figure 5.12: Time-domain Green function for one horizontal square panel. $\Delta x = \Delta y = 0.1$, $z = -0.023$

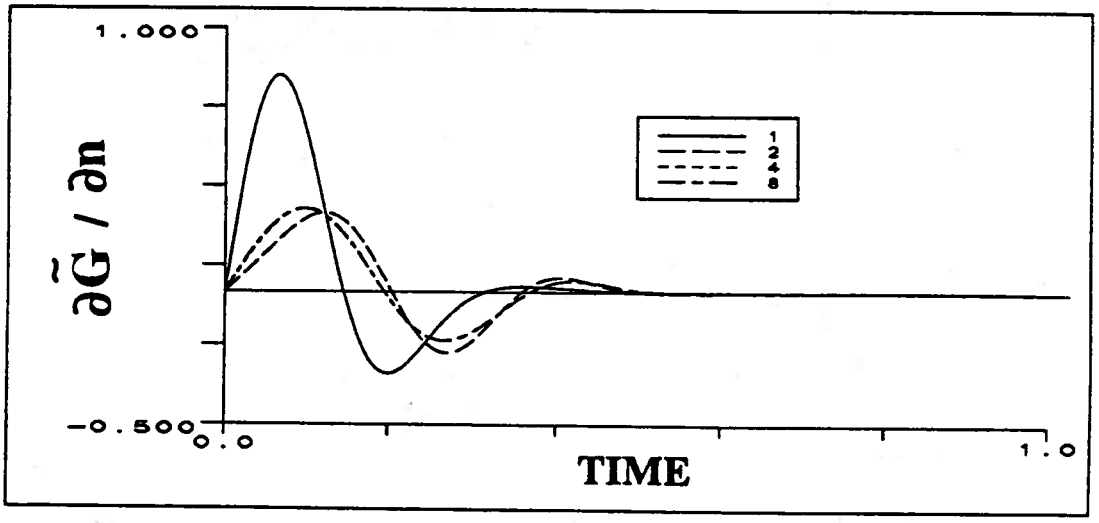

Figure 5.13: Normal derivative of the time-domain Green function for one horizontal square panel

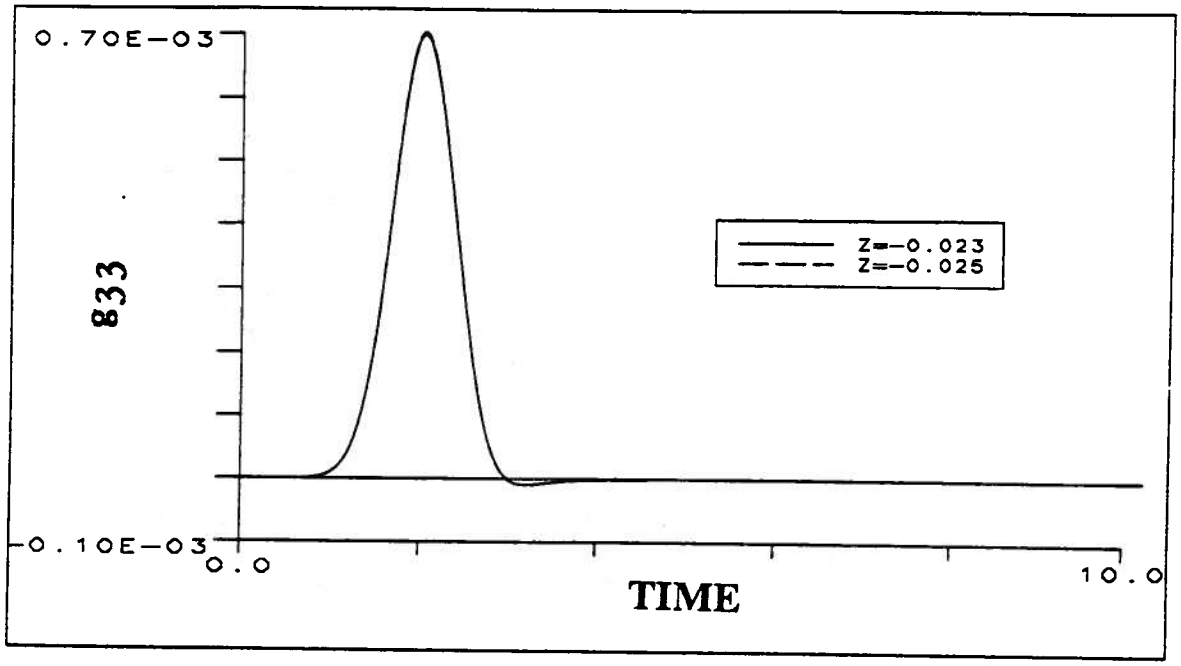

Figure 5.14: Potential on the panel for two depths of submergence $\Delta x = \Delta y = 0.1$, 12 by 12 Gauss integration

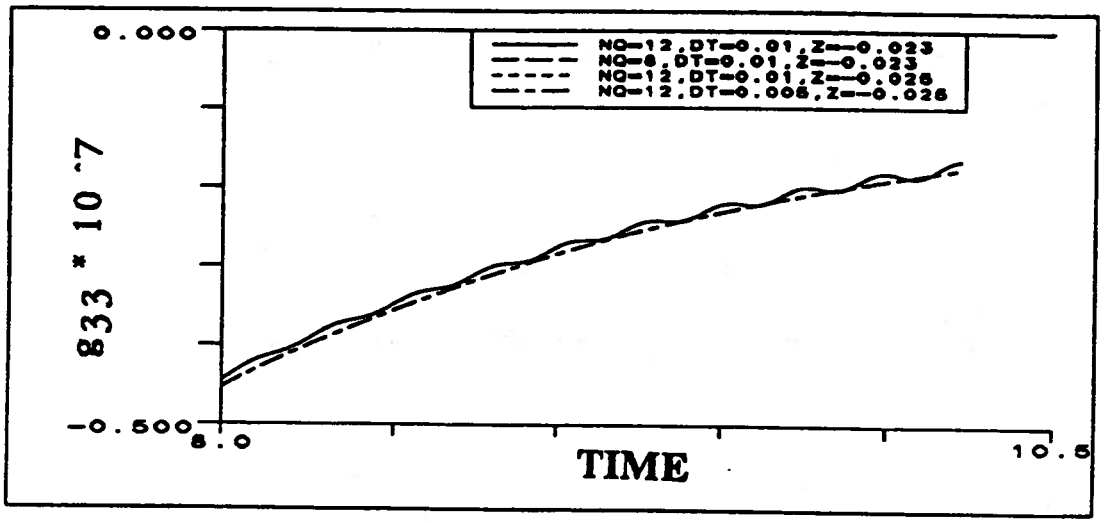

Figure 5.15: Greatly expanded view of the potential at large time. The three curves for $z = -0.023$ are coincident to graphical accuracy

Figure 5.16 shows the Fourier transform of the normal derivative ($\partial\tilde{G}/\partial z$) shown in figure 5.13 for various numbers of quadrature points on the single panel. Note that the imaginary part crosses zero at a frequency of about 25. One can easily calculate that this frequency corresponds very closely to a wave which is the length of the panel. This 'negative damping' is nonphysical, and may indicate that the waves of this frequency are not being properly resolved by the constant strength panel. Also note that the monopole or 1 by 1 Gauss rule is a very poor approximation to the converged solution, but does not have a negative damping in the frequency range shown.

Figure 5.17 shows the frequency-domain Green function integrated over a smaller panel ($\Delta x = \Delta y = 0.033$), one third the size of the previous panel. The integrated Green function is shown for several Gauss integration rules. The function obtained using the 2 by 2 and 4 by 4 rules are almost coincident. Also, as one might expect, the monopole approximation is much better for this panel. The solution for the potential on this panel does not show any sign of the instability for a very long simulation.

From this study we can draw two conclusions. First, the monopole approximation is a poor one for panels with large horizontal extent very near the free surface. However, the solution obtained using monopoles does not exhibit the unstable character that has been seen using several quadrature points per panel. Second, the solution for panels which are deeper relative to their horizontal extent are more stable, for any quadrature rule except the 1 by 1 or monopole.

In view of the added expense of using a large number of quadrature points per panel, which requires more Green function calls, it appears that for surface-piercing bodies with large flare at the waterline, the use of monopoles may be the only method which produces stable results. However, in order to obtain accurate results, a very large number of panels with small horizontal extent will be required to accurately resolve the variation of the solution over the panels near the free surface.

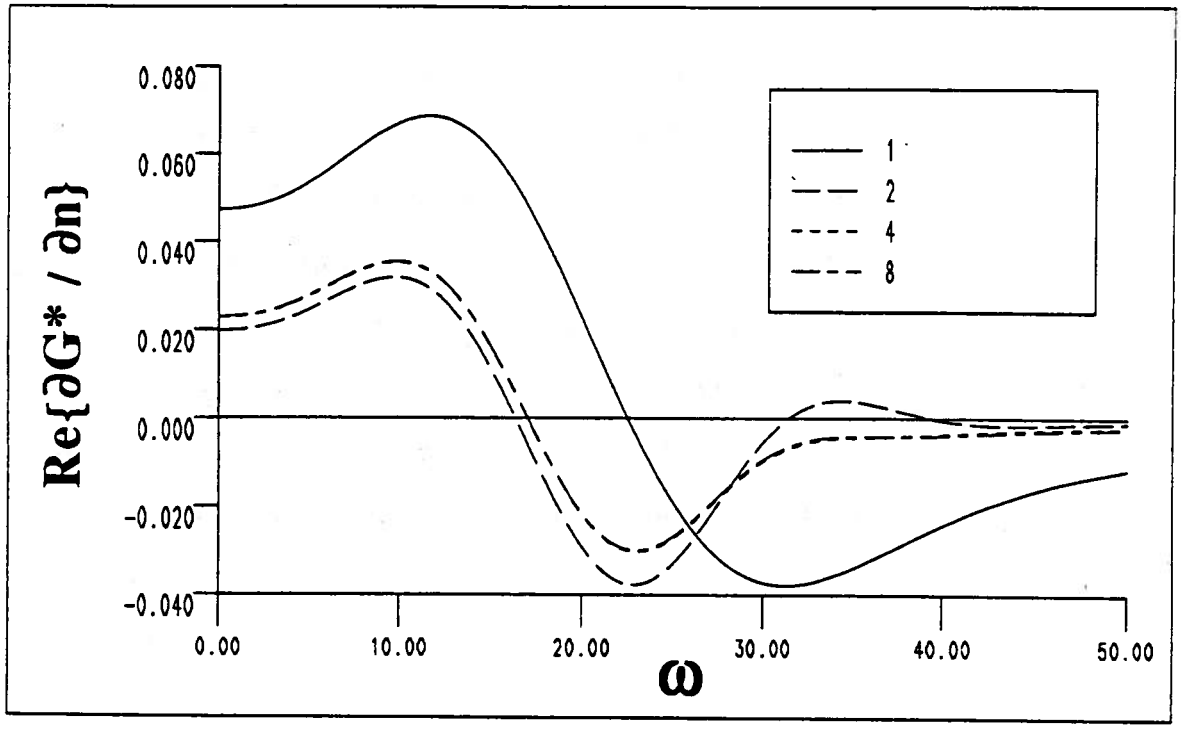

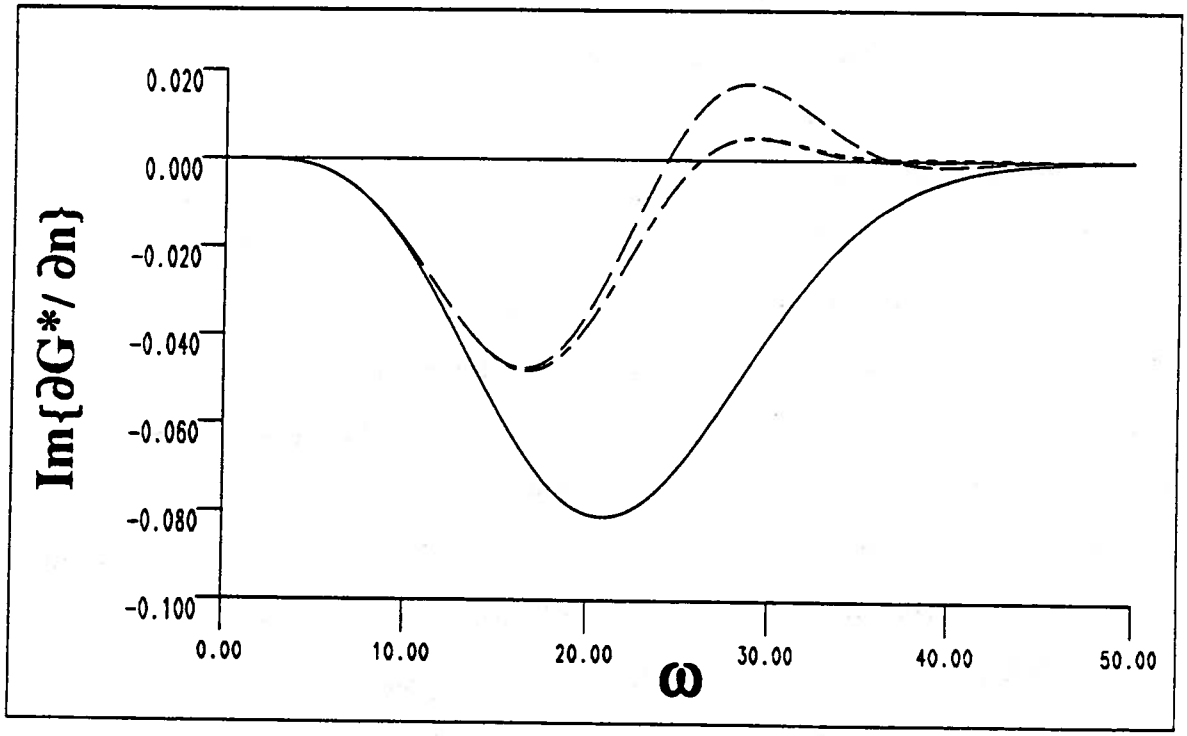

Figure 5.16: Fourier transform of the normal derivative of the Green function integrated over the panel, $\Delta x = \Delta y = 0.1$, $z = -0.023$

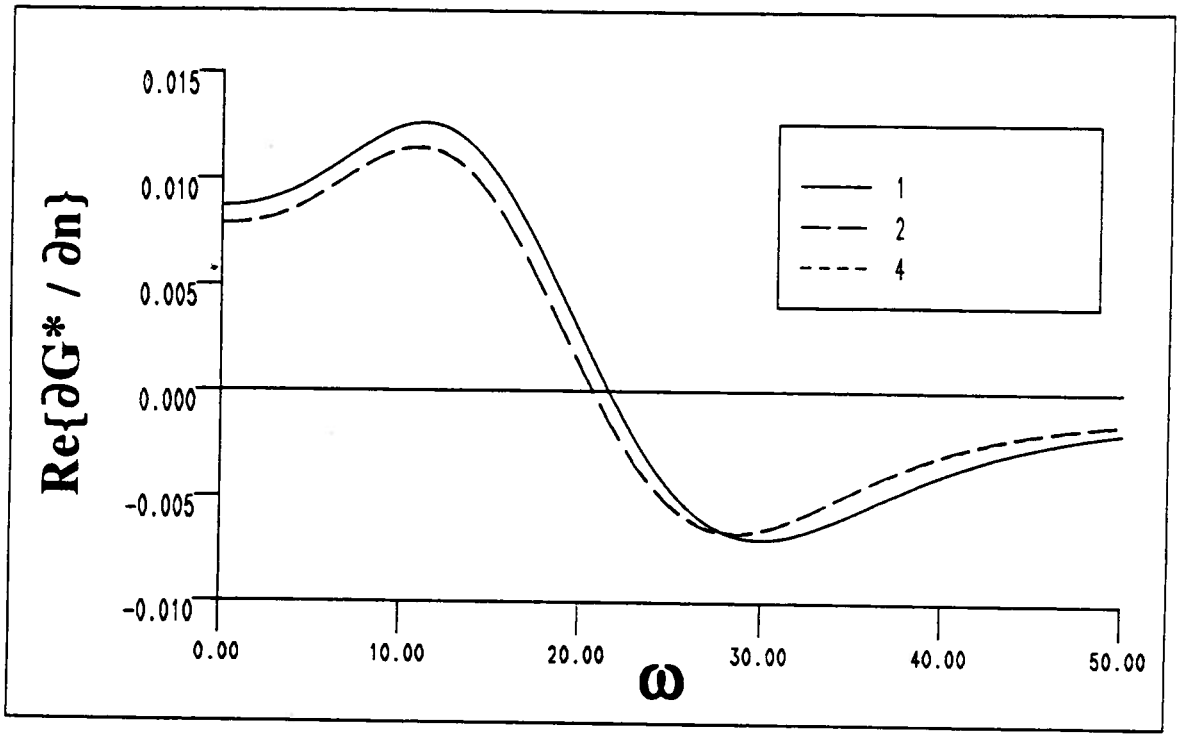

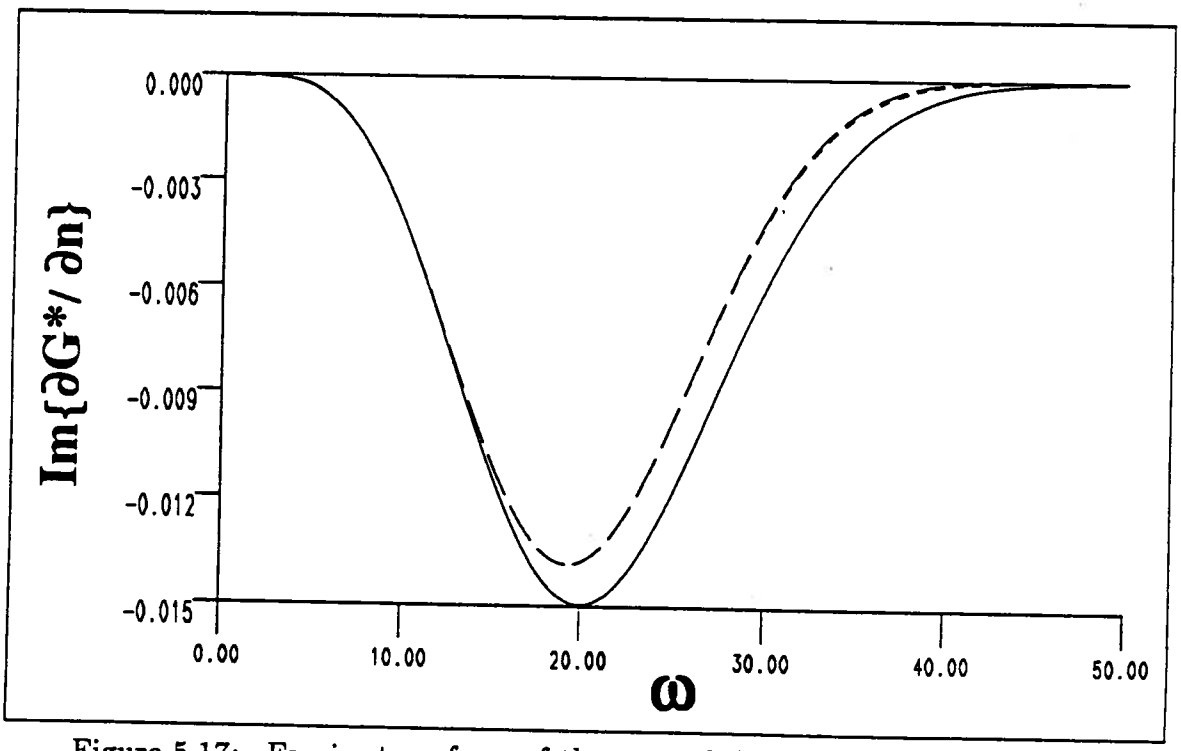

Figure 5.17: Fourier transform of the normal derivative of the Green function integrated over a smaller panel, $\Delta x = \Delta y = 0.033$, $z = -0.023$

CHAPTER VI

CONCLUSIONS AND SUGGESTIONS FOR FURTHER RESEARCH

6.1 Conclusions

The primary conclusion from the work to date on time-domain analysis is that it is a viable alternative to the traditional frequency-domain analysis. For linearized problems with forward speed, computations in the time domain appear to be much easier than the equivalent frequency-domain calculations. The Wigley model six degrees of freedom calculations for linear radiation and exciting force coefficients using 240 panels on a half-body and 256 time steps required 25 CPU minutes for $Fn = 0.3$ on a CRAY Y-MP. For radiation forces only, at zero forward speed the required time was 9 CPU minutes. In comparison with experiments and strip theory, linearized time-domain analysis gives mixed results. At times the time-domain calculations compare better with experiments and at other times the predictions are worse. For the mathematical Wigley hull form, the use of double body or simplified m-terms does not seem to make much of a difference in the added mass and damping predictions.

Difficulties have been encountered in the linearized solutions for nonwall-sided bodies when using higher order Gauss integration for the wave terms over panels.

An instability occurs at large times which appears to be the result of inadequate resolution of high frequency waves. The instability is the most severe for very shallow bodies with large flare, but does not appear to affect wall-sided, or moderately flared bodies.

Time-domain analysis can be extended to the body-exact problem in which the body boundary condition is always satisfied on the exact instantaneous wetted surface of the body. Research into the body-exact problem is continuing. To date computations have been performed only on submerged bodies.

Calculations on a submerged ellipsoid have shown excellent agreement with a steady Neumann-Kelvin code. In addition, the calculations have indicated the importance of the frequency domain singularity at $\tau = 1/4$. Because of the linear free surface boundary condition, singularities appear in the frequency domain results at $\tau = 1/4$ and the results grow slowly without bound in time-domain simulations. A simple fix-up using artificial damping on the large-time tail of the time-domain Green function is proposed. In time-domain simulations, the fix-up prevented the unbounded growth and otherwise did not alter the solution significantly. Much more research needs to be done on the large-time asymptotics and rates of decay in order to obtain the exact solutions in both the time and frequency domains.

6.2 Suggestions for Further Work

The present method of the exact Neumann-Kelvin problem should be extended for the case of floating bodies. The simulation approach in which the equations of motion are solved directly in the time domain appears promising, Lin and Yue (1990). Motion predictions could be compared directly with experimental seakeeping results without the restrictions of small-amplitude or sinusoidal motions. Local slamming pressures and added resistance in waves are quantities which should be well predicted by the method. Extreme motions are often the most important in design, and

the body-exact solutions may provide important insights without the difficulties of paneling the free surface inherent in fully nonlinear solution techniques.

Before the large-amplitude simulation can be undertaken for real floating bodies, the discretization of an arbitrary geometry must be automatic, and hence free from user input. This is because the underwater portion of the geometry changes at each time step. In order to avoid difficulties such as the instability described in Chapter 5, and to maintain the accuracy of the solution with a reasonable number of unknowns, this process must be automated. When a program is running, one cannot simply stop, repanelize the body interactively and then continue. The same problems exist in unsteady nonlinear free surface problems for surface-piercing bodies.

The problems inherent in frequency-domain Neumann-Kelvin calculations are also present in the time domain, although they often appear to be less extreme. The singularity at $\tau = 1/4$ has been shown to affect time-domain solutions. The effects of irregular frequencies are also present in the time-domain solution at zero forward speed. Existing methods such as the one proposed by Lee and Sclavounos (1989) who used a mixed source and dipole distribution to eliminate irregular frequency effects could be employed in the time-domain as well, if zero speed results are desired.

Methods of dealing with solutions for highly non wall-sided bodies which are both stable and accurate need to be pursued further. The assumption of constant strength unknowns may be partly responsible since it is inadequate to resolve the rapidly varying solution near the intersection of the body and free surface. Results of the study of the instability must be applied to obtain more useful results for the difficult case of nonwall-sided bodies. Perhaps a better technique would be the use higher-order panels or a method similar to the desingularized technique of Cao, et al. (1990) in which the potential is allowed to vary smoothly over the body. Such a method allows the tangential surface velocities to be calculated while maintaining the good mathematical foundation of a direct solution of Green's Theorem without

also provide the benefit of getting the most use out of each (still expensive) Green function evaluation.

Finally the application of parallel processing to Green function calculations may allow the body-exact solution to become a practical tool for predicting flow quantities of interest. It is felt that the limit of speed of the vectorized calculations is being approached. Further order of magnitude increases are not foreseeable with this method. Parallel computations, however, show potential for the same order of magnitude speed up as was obtained by vector processing over scalar calculations.

APPENDICES

APPENDIX A

DERIVATION OF THE INTEGRAL EQUATION FOR THE POTENTIAL FORMULATION

Green's theorem applied to the fluid domain yields

$$\int\int\int_V dV \left(\phi \nabla^2 G - G \nabla^2 \phi\right) = \int\int_S dS \left(\phi \frac{\partial G}{\partial n} - G \frac{\partial \phi}{\partial n}\right) \tag{A.1}$$

with the volume V bounded by S, where $S = S_B \cup S_F \cup S_\infty$, and S_B is the body surface, S_F is the free surface, and S_∞ is the bounding surface at infinity, and G is the time-domain Green function given by (2.9).

For a point on S_B, the principal value of the surface integral is 2π for a flat panel. Integrating both sides with respect to time and separating the instantaneous from the memory parts of the Green function, one arrives at the following equation:

$$\phi(P,t) = -\frac{1}{2\pi}\int\int_{S(t)} dS_Q \left(\phi(Q,t)\frac{\partial}{\partial n_Q}\left(\frac{1}{r}-\frac{1}{r'}\right) - \left(\frac{1}{r}-\frac{1}{r'}\right)\frac{\partial}{\partial n_Q}\phi(Q,t)\right)$$
$$-\frac{1}{2\pi}\int_{-\infty}^{t} d\tau \int\int_{S(\tau)} dS_Q \left(\phi(Q,\tau)\frac{\partial}{\partial n_Q}\tilde{G}(P,Q,t,\tau) - \tilde{G}(P,Q,t,\tau)\frac{\partial}{\partial n_Q}\phi(Q,\tau)\right) \tag{A.2}$$

Far from the body, the potential dies off in such a manner that the contribution from the bounding surface is zero. The remaining surfaces are the body and free surface. Thus,

$$S(t) = S_B(t) + S_F(t)$$

The body contribution is:

$$I_B(P,t) = -\frac{1}{2\pi}\int\int_{S_B(t)} dS_Q \left(\phi(Q,t)\frac{\partial}{\partial n_Q}\left(\frac{1}{r}-\frac{1}{r'}\right) - \left(\frac{1}{r}-\frac{1}{r'}\right)\frac{\partial}{\partial n_Q}\phi(Q,t)\right)$$
$$-\frac{1}{2\pi}\int_{-\infty}^{t} d\tau \int\int_{S_B(\tau)} dS_Q \left(\phi(Q,\tau)\frac{\partial}{\partial n_Q}\tilde{G}(P,Q,t,\tau) - \tilde{G}(P,Q,t,\tau)\frac{\partial}{\partial n_Q}\phi(Q,\tau)\right) \tag{A.3}$$

The integrals over the free surface can be reduced to line integrals around the intersection line of the body surface and free surface by an application of the transport theorem. This eliminates the need to distribute unknowns on the free surface, and greatly eases the computational burden of the problem. To proceed, one first notes that since the $1/r$ and $1/r'$ terms cancel on the free surface, the contribution of the free surface can be written as

$$I_F(P,t) = -\frac{1}{2\pi}\int_{-\infty}^{t} d\tau \int\int_{S_F(\tau)} dS_Q \left(\phi(Q,\tau)\frac{\partial}{\partial n}\tilde{G}(P,Q,t,\tau) - \tilde{G}(P,Q,t,\tau)\frac{\partial}{\partial n}\phi(Q,\tau)\right) \tag{A.4}$$

On the free surface, using the free surface boundary condition (2.3), we have

$$\frac{\partial}{\partial n} = \frac{\partial}{\partial \zeta} = -\frac{1}{g}\frac{\partial}{\partial \tau^2} \tag{A.5}$$

so that this can be written as

$$I_F(P,t) = \frac{1}{2\pi g}\int_{-\infty}^{t} d\tau \int\int_{S_F(\tau)} dS_Q \left(\phi(Q,\tau)\frac{\partial}{\partial \tau^2}\tilde{G}(P,Q,t,\tau) - \tilde{G}(P,Q,t,\tau)\frac{\partial}{\partial \tau^2}\phi(Q,\tau)\right)$$
$$= \frac{1}{2\pi g}\int_{-\infty}^{t} d\tau \int\int_{S_F(\tau)} dS_Q \frac{\partial}{\partial \tau}\left(\phi(Q,\tau)\tilde{G}_\tau(P,Q,t,\tau) - \tilde{G}(P,Q,t,\tau)\,\phi_\tau(Q,\tau)\right) \tag{A.6}$$

A two-dimensional form of the transport theorem can be applied in the form

$$\frac{d}{dt}\int\int_{S(\tau)} dS_Q\, f(Q,\tau) = \int\int_{S(t)} dS_Q \frac{\partial}{\partial \tau} f(Q,t) + \oint_{\Gamma(\tau)} dl_Q\, V_N\, f(Q,\tau) \tag{A.7}$$

where, V_N is the two-dimensional normal velocity in the $z = 0$ plane of a point on Γ. The direction of the line integral is counter-clockwise along the outer contour, and hence clockwise around the intersection line, as shown in figure A.1. The result is

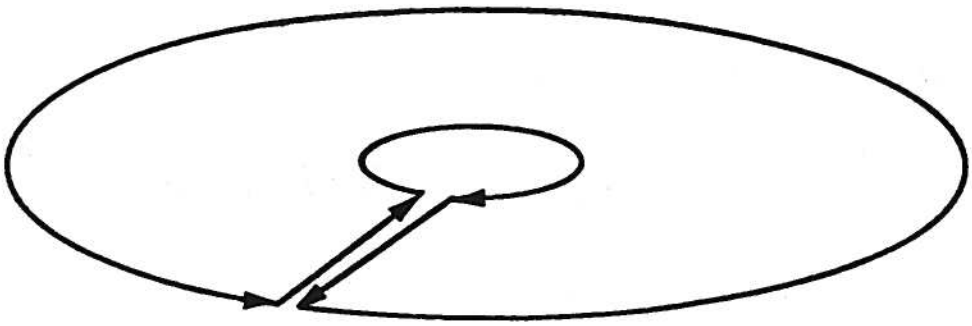

Figure A.1: Line integral contours on the free surface

$$
\begin{aligned}
I_F(P,t) &= \frac{1}{2\pi g}\int_{-T_0}^{t} d\tau \frac{d}{dt}\int\int_{S_F(\tau)} dS_Q \left(\phi(Q,\tau)\,\tilde{G}_\tau(P,Q,t,\tau) - \phi_\tau(Q,\tau)\,\tilde{G}(P,Q,t,\tau)\right) \\
&- \frac{1}{2\pi g}\int_{-T_0}^{t} d\tau \oint_{\Gamma(\tau)} dl_Q\, V_N \left(\phi(Q,\tau)\,\tilde{G}_\tau(P,Q,t,\tau) - \tilde{G}(P,Q,t,\tau)\,\phi_\tau(Q,\tau)\right) \\
&= \frac{1}{2\pi g}\int\int_{S_F(t^+)} dS_Q \left(\phi\left(Q,t^+\right)\tilde{G}_\tau\left(P,Q,T_0^-\right) - \phi_\tau\left(Q,t^+\right)\tilde{G}\left(P,Q,T_0^-\right)\right) \\
&- \frac{1}{2\pi g}\int\int_{S_F(T_0^-)} dS_Q \left(\phi\left(Q,T_0^-\right)\tilde{G}_\tau\left(P,Q,t^+\right) - \phi_\tau\left(Q,T_0^-\right)\tilde{G}\left(P,Q,t^+\right)\right) \\
&- \frac{1}{2\pi g}\int_{-T_0}^{t} d\tau \oint_{\Gamma(\tau)} dl_Q\, V_N \left(\phi(Q,\tau)\,\tilde{G}_\tau(P,Q,t,\tau) - \tilde{G}(P,Q,t,\tau)\,\phi_\tau(Q,\tau)\right)
\end{aligned}
\tag{A.8}
$$

The outer contour at infinity does not contribute, and the integrals along the two sides of the cut are in opposite directions. Hence, they cancel. The limits of the temporal integration extend from $T_0 - \epsilon$ to $t + \epsilon$, as denoted in (A.8), where T_0 represents the time at which the motion begins. Subsequently, the limit as $T_0 \to -\infty$ can be taken in a proper manner. Using the initial conditions (2.7) and the Green function properties (2.9), it can be shown that the first two terms in (A.8) are zero.

The remaining term is the line integral contribution to the potential integral equation:

$$I_F(P,t) = -\frac{1}{2\pi g}\int_{-\infty}^{t} d\tau \oint_{\Gamma(\tau)} dl_Q \; V_N \left(\phi(Q,\tau)\,\tilde{G}_\tau(P,Q,t,\tau) - \tilde{G}(P,Q,t,\tau)\,\phi_\tau(Q,\tau)\right) \tag{A.9}$$

Combining (A.4) and (A.10) yields the desired form of equation (2.10):

$$\begin{aligned}\phi(P,t) + \frac{1}{2\pi}\int\int_{S_B(t)} dS_Q\,\phi(Q,t)\frac{\partial}{\partial n_Q}\left(\frac{1}{r}-\frac{1}{r'}\right) &= \frac{1}{2\pi}\int\int_{S_B(t)} dS_Q \left(\frac{1}{r}-\frac{1}{r'}\right)\frac{\partial}{\partial n_Q}\phi(Q,t) \\ -\frac{1}{2\pi}\int_{-\infty}^{t} d\tau \int\int_{S_B(\tau)} dS_Q &\left\{\phi(Q,\tau)\frac{\partial}{\partial n_Q}\tilde{G}(P,Q,t,\tau) - \tilde{G}(P,Q,t,\tau)\frac{\partial}{\partial n_Q}\phi(Q,\tau)\right\} \\ -\frac{1}{2\pi g}\int_{-\infty}^{t} d\tau \oint_{\Gamma(\tau)} dl_Q &\left\{\phi(Q,\tau)\frac{\partial}{\partial \tau}\tilde{G}(P,Q,t,\tau) - \tilde{G}(P,Q,t,\tau)\frac{\partial}{\partial \tau}\phi(Q,\tau)\right\} V_N(Q,\tau)\end{aligned} \tag{A.10}$$

By using the mean body position and transferring to a steadily moving coordinate system, the line integral terms given by King (1987) can be recovered.

APPENDIX B

DERIVATION OF THE INTEGRAL EQUATION FOR THE SOURCE FORMULATION

The derivation of the integral equation for the source formulation (2.11) follows similar steps as the derivation of the integral equation for the potential in Appendix A. A fictitious inner flow inside the body is used to specify that no jump in the potential occurs across the boundary, and to define the source strength. Prime ($'$) variables will be used to denote quantities associated with the inner flow. The normal for the inner flow is in the opposite sense to that used for the outer flow, i.e.,

$$\mathbf{n}' = -\mathbf{n} \tag{B.1}$$

By applying the same steps as in Appendix A to the inner flow potential, ϕ' one arrives at a similar formula to equation (2.10). Since the field point is outside the domain of integration, the left hand side of Green's identity is zero. Thus,

$$\begin{aligned}
0 = &-\frac{1}{4\pi}\int\int_{S_B(t)} dS_Q \left\{\phi'(Q,t)\frac{\partial}{\partial n'_Q}\left(\frac{1}{r}-\frac{1}{r'}\right) - \left(\frac{1}{r}-\frac{1}{r'}\right)\frac{\partial}{\partial n'_Q}\phi'(Q,t)\right\} \\
&-\frac{1}{4\pi}\int_{-\infty}^{t} d\tau \int\int_{S_B(\tau)} dS_Q \left\{\phi'(Q,\tau)\frac{\partial}{\partial n'_Q}\tilde{G}(P,Q,t,\tau) - \tilde{G}(P,Q,t,\tau)\frac{\partial}{\partial n'_Q}\phi'(Q,\tau)\right\} \\
&-\frac{1}{4\pi g}\int_{-\infty}^{t} d\tau \oint_{\Gamma(\tau)} dl_Q \left\{\phi'(Q,\tau)\frac{\partial}{\partial \tau}\tilde{G}(P,Q,t,\tau) - \tilde{G}(P,Q,t,\tau)\frac{\partial}{\partial \tau}\phi'(Q,\tau)\right\} V_N(Q,\tau)
\end{aligned} \tag{B.2}$$

where the singular contribution has not yet been evaluated. The sense of the line integral for the inner flow is counter-clockwise around the intersection line. Combining

(B.2) with a similar formula for the outer flow potential ϕ, results in:

$$\begin{aligned}
\phi(P,t) = &-\frac{1}{4\pi}\int\int_{S_B(t)} dS_Q \left\{ (\phi(Q,t) - \phi'(Q,t)) \frac{\partial}{\partial n_Q}\left(\frac{1}{r} - \frac{1}{r'}\right) \right. \\
&\left. - \left(\frac{1}{r} - \frac{1}{r'}\right) \frac{\partial}{\partial n_Q} (\phi(Q,t) - \phi'(Q,t)) \right\} \\
&- \frac{1}{4\pi}\int_{-\infty}^{t} d\tau \int\int_{S_B(\tau)} dS_Q \left\{ (\phi(Q,\tau) - \phi'(Q,\tau)) \frac{\partial}{\partial n_Q} \tilde{G}(P,Q,t,\tau) \right. \\
&\left. - \tilde{G}(P,Q,t,\tau) \frac{\partial}{\partial n_Q} (\phi(Q,\tau) - \phi'(Q,\tau)) \right\} \\
&- \frac{1}{4\pi g}\int_{-\infty}^{t} d\tau \oint_{\Gamma(\tau)} dl_Q \left\{ (\phi(Q,\tau) - \phi'(Q,\tau)) \frac{\partial}{\partial \tau} \tilde{G}(P,Q,t,\tau) \right. \\
&\left. - \tilde{G}(P,Q,t,\tau) \frac{\partial}{\partial \tau} (\phi(Q,\tau) - \phi'(Q,\tau)) \right\} V_N(Q,\tau)
\end{aligned} \tag{B.3}$$

For a distribution of sources, there is no jump in the potential across the surface:

$$\phi(Q,t) - \phi'(Q,t) = 0$$

Thus, we obtain

$$\begin{aligned}
\phi(P,t) = &\frac{1}{4\pi}\int\int_{S_B(t)} dS_Q \left(\frac{1}{r} - \frac{1}{r'}\right) \frac{\partial}{\partial n_Q} (\phi(Q,t) - \phi'(Q,t)) \\
&- \frac{1}{4\pi}\int_{-\infty}^{t} d\tau \int\int_{S_B(\tau)} dS_Q \tilde{G}(P,Q,t,\tau) \frac{\partial}{\partial n_Q} (\phi(Q,\tau) - \phi'(Q,\tau)) \\
&+ \frac{1}{4\pi g}\int_{-\infty}^{t} d\tau \oint_{\Gamma(\tau)} dl_Q \frac{\partial}{\partial \tau} (\phi(Q,\tau) - \phi'(Q,\tau)) \tilde{G}(P,Q,t,\tau) V_N(Q,\tau)
\end{aligned} \tag{B.4}$$

The contribution from the line integral is

$$I_F(P,t) = \frac{1}{4\pi g}\int_{-\infty}^{t} d\tau \oint_{\Gamma(\tau)} dl_Q \frac{\partial}{\partial \tau} (\phi(Q,\tau) - \phi'(Q,\tau)) \tilde{G}(P,Q,t,\tau)\ V_N(Q,\tau) \tag{B.5}$$

We note that this formulation has been carried out in the earth-fixed coordinate system. In a system fixed to the body, the time derivative includes a convective term, that is:

$$\frac{\partial}{\partial t} = \frac{\partial}{\partial t_M} - \mathbf{V} \cdot \nabla \tag{B.6}$$

where, M represents the derivative in the moving coordinate system. Thus, we have

$$I_F(P,t) = -\frac{1}{4\pi g}\int_{-\infty}^{t} d\tau \oint_{\Gamma(\tau)} dl_Q \left(\frac{\partial}{\partial \tau_M} - \mathbf{V}\cdot\nabla\right) \left(\phi(Q,\tau) - \phi'(Q,\tau)\right) \tilde{G}(P,Q,t,\tau)\ V_N(Q,\tau) \quad \text{(B.7)}$$

In the moving system the time derivative of the potential jump is zero. The gradient operator can be applied in a locally orthogonal $\mathbf{n}-\mathbf{l}-\mathbf{s}$ coordinate system, with $\mathbf{n}$ representing the normal, that is,

$$\mathbf{V}\cdot\nabla = V_n\frac{\partial}{\partial n} + V_l\frac{\partial}{\partial l} + V_s\frac{\partial}{\partial s}$$

For sources there is no jump in tangential velocity, and the only nonzero component is in the normal direction, representing the source strength. Setting the source strength in the *moving* coordinate system to be

$$\sigma = -\frac{\partial}{\partial n}(\phi - \phi') \quad \text{(B.8)}$$

results in,

$$I_F(P,t) = \frac{1}{4\pi g}\int_{-\infty}^{t} d\tau \oint_{\Gamma(\tau)} dl_Q\ \sigma(Q,\tau)\ \tilde{G}(P,Q,t,\tau)\ V_n(Q,\tau)\, V_N(Q,\tau) \quad \text{(B.9)}$$

where, V_n is the local normal velocity of the body surface on the intersection line in the earth-fixed frame. Adding the contributions from the body surface and line integrals together gives the expression for the potential in the source formulation, equation (2.12):

$$\phi(P,t) = -\frac{1}{4\pi}\iint_{S_B(t)} dS_Q\,\sigma(Q,t)\left(\frac{1}{r}-\frac{1}{r'}\right) - \frac{1}{4\pi}\int_{-\infty}^{t} d\tau \iint_{S_B(\tau)} dS_Q\,\sigma(Q,\tau)\,\tilde{G}(P,Q,t,\tau) + \frac{1}{4\pi g}\int_{-\infty}^{t} d\tau \oint_{\Gamma(\tau)} dl_Q \left\{\sigma(Q,\tau)\,\tilde{G}(P,Q,t,\tau)\right\} V_n(Q,\tau)\, V_N(Q,\tau) \quad \text{(B.10)}$$

Taking the gradient with respect to the field point variables of the above expression gives the fluid velocity. Dotting this with the normal gives the expressions necessary for the source integral equation (2.11). For an unsteady maneuver in the horizontal plane, the terms reduce to those give by Liapis (1985) in his Appendix A for this case.

BIBLIOGRAPHY

BIBLIOGRAPHY

[1] Adachi, H. and S. Ohmatsu. 1979. On the influence of irregular frequencies in the integral equation solutions of the time-dependent free surface problems. *Journal of Engineering Mathematics*, 16(2): 97-119.

[2] Ashley, H. and M. Landahl. 1965. *Aerodynamics of Wings and Bodies.* Reading, MA: Addison-Wesley.

[3] Beck, R.F. 1989. Motions in waves. Chapter 8, section 3 of *Principles of Naval Architecture*, edited by Edward Lewis, Jersey City: Society of Naval Architects and Marine Engineers.

[4] Beck, R.F, and S.J. Liapis. 1986. Transient motions of floating bodies at zero forward speed. *Journal of Ship Research*, 31(3): 164-76.

[5] Beck, R.F., and A.R. Magee. 1990. Time-domain analysis for predicting ship motions. *Proceedings of the IUTAM symposium on dynamics of marine vehicles and structures in waves.* Uxbridge, U.K.: Brunel University.

[6] Bertram, V. 1990. A Rankine source approach to forward speed diffraction problems. *Proceedings of the fifth international workshop on water waves and floating bodies*, Manchester, U.K.

[7] Brard, R. 1948. Introduction à l'étude théorique du tangage en marche. Bulletin de l'A.T.M.A. No. 48. Paris: A.T.M.A.

[8] Burtness, M., and R. Steele. 1989. I3G conversion to HP workstations. Annapolis: SAIC Report 89/1743.

[9] Cao, Y.S., W.W. Schultz, and R.F. Beck. 1990. Three-dimensional, unsteady computations of nonlinear waves caused by underwater disturbances. *Proceedings of the eighteenth symposium on naval hydrodynamics.* Washington, D.C: Office of Naval Research.

[10] Chang, M.-S. 1977. Computation of three-dimensional ship motions with forward speed. *Proceedings of the second international conference on numerical ship hydrodynamics*, 124-35. Berkeley, CA: University of California.

[11] Cummins, W.E. 1962. The impulse response function and ship motions. *Schiffstechnik*, 9: 101-09.

[12] Dagan, G., and T. Miloh 1980. Flow past oscillating bodies at resonant frequency. *Proceedings of the thirteenth symposium on naval hydrodynamics*, 355-73. Tokyo, Japan.

[13] Dassonville, B. 1987. Etude expérimentale des effects non-linéaires du mouvement de grande amplitude d'un corps faiblement immergé. Ph.D. Diss., Université de Nantes.

[14] Doctors, L.J., and R.F. Beck. 1987. Convergence properties of the Neumann-Kelvin problem for a submerged body. *Journal of Ship Research*, 31(4): 227-34.

[15] Dommermuth, D.G., and D.K.P. Yue. 1987. Numerical simulations of nonlinear axisymmetric flows with a free surface. *Journal of Fluid Mechanics.* 178: 195-219.

[16] Faltinsen, O.M. and R. Zhao. 1990. Numerical predictions of a ship motion at high forward speed. *Proceedings of the Meeting on the Dynamics of Ships.* London: The Royal Society of London.

[17] Falzarano, J.M. 1990. Predicting complicated dynamics leading to vessel capsizing. Ph.D. Diss., The University of Michigan.

[18] Farell, C. 1973. On the wave resistance of a submerged spheroid. *Journal of Ship Research*, 17(1): 1-11.

[19] Ferrant, P. 1988. An accelerated computational method for time-domain analysis of 3D wave-body interactions. *Proceedings of the third international workshop on water waves and floating bodies.* MIT Press: Cambridge, MA.

[20] Ferrant, P. 1989. Radiation d'ondes de gravité par les mouvements de grande amplitude d'un corps immergé: Comparaison des approches fréquentielle et instationaire. Ph.D. Diss., Université de Nantes.

[21] Ferrant, P. 1990. A coupled time and frequency approach for nonlinear wave radiation. *Proceedings of the eighteenth symposium on naval hydrodynamics.* Washington, D.C: Office of Naval Research.

[22] Finklestein, A. 1957. The initial value problem for transient water waves. *Communications on Pure and Applied Mathematics*, 10: 511-22.

[23] Gerritsma, J. 1988. Motions, wave loads and added resistance in waves of two Wigley hull forms. Delft, Netherlands: Technical University of Delft, Report No. 804.

[24] Ginsberg, M. 1985. An overview of the computational environments offered by current and future supercomputers. *Supercomputers in the Automotive Industry*, Special Publications SP-624, Warrendale, PA: Society of Automotive Engineers, 1-25.

[25] Guevel, P., and J. Bougis. 1982. Ship motions with forward speed in infinite depth. *International Shipbuilding Progress*, 29: 103-17.

[26] Guo, C.-L.S. 1981. Nonlinear theory of ship manuevering. *Journal of Ship Research*, 25(1): 21-43.

[27] Harries, S. 1990. PANNURBS: An interactive program for the panelization of NURBS surfaces. User's manual. The University of Michigan, Department of Naval Architecture and Marine Engineering.

[28] Hess, J.L., and A.M.O. Smith. 1964. Calculation of nonlifting potential flow about arbitrary three-dimensional bodies. *Journal of Ship Research*, 8(2): 22-44.

[29] Hoff, J.R. 1990. Three-dimensional Green function of a vessel with forward speed in waves. Ph.D. Diss., The Norwegian Institute of Technology, Trondheim.

[30] Inglis, R.B., and W.G. Price. 1981a. Irregular frequencies in three-dimensional source distribution techniques. *International Shipbuilding Progress*, 28(319): 57-62.

[31] Inglis, R.B., and W.G. Price. 1981b. A three-dimensional ship motion theory— comparison between theoretical prediction and experimental data of the hydrodynamic coefficients with forward speed. *Transactions of the Royal Institute of Naval Architects*, 124: 141-57.

[32] Jami, A., and G. Pot. 1985. Finite element solution for the transient flow past a freely floating body. *Proceedings of the fourth international conference on numerical ship hydrodynamics*, 185-199. Washington, DC: National Academy of Sciences.

[33] Jensen, G., Z.X. Mi, and H. Söding 1988. Rankine source methods for numerical solutions of the steady wave resistance problem. *Proceedings of the sixteenth symposium on naval hydrodynamics*, 575-582. Washington, DC: Office of Naval Research.

[34] Kang, C.-G. and I.-Y. Gong. 1990. A numerical method for three-dimensional nonlinear free surface problems. *Proceedings of the eighteenth symposium on naval hydrodynamics.* Washington, D.C: Office of Naval Research.

[35] King, B.K., R.F. Beck, and A.R. Magee 1988. Seakeeping calculations with forward speed using time-domain analysis. *Proceedings of the seventeenth symposium on naval hydrodynamics*, 577-596. Washington, DC: Office of Naval Research.

[36] King, B.K. 1987. Time-domain analysis of wave exciting forces on ships and bodies. Ph.D. Diss., The University of Michigan.

[37] Korsmeyer, F.T. 1988. The first and second order transient free-surface wave radiation problems. Ph.D. Diss., Massachusetts Institute of Technology.

[38] Korsmeyer, F.T., C.-H. Lee, J.N. Newman, and P.D. Sclavounos. 1988. The analysis of wave effects on tension leg platforms. *Proceedings of the international conference on offshore mechanics and arctic engineering.* Houston.

[39] Lamb, H. 1929. Hydrodynamics. Cambridge, U.K.: Cambridge University Press.

[40] Lee, C.-H., and P.D. Sclavounos. 1987. Removing the irregular frequencies from integral equations in wave-body interactions. Submitted for publication.

[41] Levesque, J.M., and J.W. Williamson. 1989. *A Guidebook to Fortran on Supercomputers.* San Diego: Academic Press.

[42] Liapis, S.J. 1986. Time-domain analysis of ship motions. Ph.D. Diss., The University of Michigan.

[43] Liapis, S.J. 1988. Optimization of the panel discretization of an arbitrary body to solve potential flow problems. Unpublished.

[44] Liapis, S.J., and R.F. Beck. 1985. Seakeeping computations using time-domain analysis. *Proceedings of the fourth international conference on numerical hydrodynamics,* 34-54. Washington, D.C.: National Academy of Sciences.

[45] Lin, W.-M., and D.K.P. Yue. 1990. Numerical solutions for large-amplitude ship motions in the time domain. *Proceedings of the eighteenth symposium on naval hydrodynamics.* Washington, D.C: Office of Naval Research.

[46] Magee, A.R. and R.F. Beck. 1988a. Compendium of ship motion calculations using linear time-domain analysis. The University of Michigan, Department of Naval Architecture and Marine Engineering Report No. 310.

[47] Magee, A.R. and R.F. Beck. 1988b. Nonlinear motions in the time-domain. *Proceedings of the third international workshop on water waves and floating bodies.* Cambridge, MA: MIT Press

[48] Magee, A.R., and R.F. Beck. 1989. Vectorized computation of the time-domain Green function. *Proceedings of the fourth international workshop on water waves and floating bodies.* Øystese, Norway.

[49] Miloh, T. 1977. Hydrodynamics of deformable contiguous spherical shapes in an incompressible fluid. *Journal of Engineering Mathematics*, 11(4): 349-372.

[50] Miloh, T., and V.C. Patel. 1973. Orthogonal coordinate systems for three-dimensional boundary layers, with particular reference to ship forms. *Journal of Ship Research*, 17(1): 50-58.

[51] Nakos, D.E. 1990. Ship wave patterns and motions by a three-dimensional Rankine panel method. Ph.D. Diss., Massachusetts Institute of Technology.

[52] Newman, J.N. 1977. *Marine hydrodynamics.* Cambridge, MA: MIT Press.

[53] Newman, J.N. 1978. The theory of ship motions. *Advances in Applied Mechanics*, 18: 221-285.

[54] Newman, J.N. 1985. Transient axisymmetric motion of a floating cylinder. *Journal of Fluid Mechanics*, 157: 17-33.

[55] Newman, J.N. 1991. Approximation of free surface Green functions. *Wave Asymptotics: Proceedings of the Fritz Ursell retirement meeting.* Cambridge, U.K.: Cambridge University Press.

[56] Ogilvie, T.F. 1964. Recent progress toward the understanding and prediction of ship motions. *Proceedings of the fifth symposium on naval hydrodynamics*, 3-128. Washington, DC: Office of Naval Research.

[57] Ogilvie, T.F. 1977. Singular-perturbation problems in ship hydrodynamics. *Advances in Applied Mechanics*, 17: 91-188.

[58] Ogilvie, T.F., and E.O. Tuck. 1969. A rational strip theory for ship motions, Part 1. The University of Michigan, Department of Naval Architecture and Marine Engineering, Report No. 013.

[59] Ohkusu, M., and O.M. Faltinsen. 1990. Prediction of radiation forces on a catamaran at high Froude number. *Proceedings of the eighteenth symposium on naval hydrodynamics.* Washington, D.C: Office of Naval Research.

[60] Ohkusu, M., and H. Iwashita. 1989. Evaluation of the Green function for ship motions at forward speed and applications to radiation and diffraction problems. *Proceedings of the fourth international workshop on water waves and floating bodies*, Øystese, Norway.

[61] Salvesen, N., E.O. Tuck, and O. Faltinsen. 1970. Ship motions and sea loads, *Transactions of the Society of Naval Architects and Marine Engineers*, 78: 250-87.

[62] Sclavounos, P. 1985. The unified slender-body theory: Ship motions in waves. *Proceedings of the fifteenth symposium on naval hydrodynamics*, 177-193. Washington, D.C: Office of Naval Research.

[63] Sclavounos, P. and D. Nakos. 1990. Ship motions by a three-dimensional Rankine source panel method. *Proceedings of the eighteenth symposium on naval hydrodynamics.* Washington, D.C: Office of Naval Research.

[64] Scragg, C. 1990. Numerical Solutions of the 'Dawson' free-surface problem using Havelock singularities. *Proceedings of the eighteenth symposium on naval hydrodynamics.* Washington, D.C: Office of Naval Research.

[65] Stoker, J.J. 1957. *Water Waves.* New York: Interscience Publishers.

[66] Timman, R., and J.N. Newman. 1962. The coupled damping coefficients of symmetric ships. *Journal of Ship Research*, 5(4): 34-55.

[67] Wehausen, J.V. 1967. Initial value problem for the motion in an undulating sea of a body with fixed equilibrium position. *Journal of Engineering Mathematics* 1:1-19.

[68] Wehausen, J.V. 1964. Effect of the initial acceleration upon the wave resistance of ship models. *Journal of Ship Research*, 1964(1): 38-50.

[69] Wehausen, J.V. and E.V. Laitone. 1960. Surface Waves. In *Handbuch der Physik*, 9: 446-778, edited by S. Flugge. New York: Springer-Verlag.

[70] Wu, G.X. and R. Eatock Taylor 1987. A Green's function form for ship motions at forward speed. *International Shipbuilding Progress*, 34(394): 189-96.

[71] Yeung, R.W. 1982. The transient heaving motion of floating cylinders. *Journal of Engineering Mathematics*, 16: 97-119.

[72] Yeung, R.W., and S.H. Kim. 1985. A new development in the theory of oscillating and translating slender ships. *Proceedings of the fifteenth symposium on naval hydrodynamics*, 195-218. Washington, DC: Office of Naval Research.